# **Springer Theses**Recognizing Outstanding Ph.D. Research

Steven Bloemen

# High-Precision Studies of Compact Variable Stars



# **Springer Theses**

Recognizing Outstanding Ph.D. Research

### Aims and Scope

The series "Springer Theses" brings together a selection of the very best Ph.D. theses from around the world and across the physical sciences. Nominated and endorsed by two recognized specialists, each published volume has been selected for its scientific excellence and the high impact of its contents for the pertinent field of research. For greater accessibility to non-specialists, the published versions include an extended introduction, as well as a foreword by the student's supervisor explaining the special relevance of the work for the field. As a whole, the series will provide a valuable resource both for newcomers to the research fields described, and for other scientists seeking detailed background information on special questions. Finally, it provides an accredited documentation of the valuable contributions made by today's younger generation of scientists.

### Theses are accepted into the series by invited nomination only and must fulfill all of the following criteria

- They must be written in good English.
- The topic should fall within the confines of Chemistry, Physics, Earth Sciences, Engineering and related interdisciplinary fields such as Materials, Nanoscience, Chemical Engineering, Complex Systems and Biophysics.
- The work reported in the thesis must represent a significant scientific advance.
- If the thesis includes previously published material, permission to reproduce this must be gained from the respective copyright holder.
- They must have been examined and passed during the 12 months prior to nomination.
- Each thesis should include a foreword by the supervisor outlining the significance of its content.
- The theses should have a clearly defined structure including an introduction accessible to scientists not expert in that particular field.

More information about this series at http://www.springer.com/series/8790

### Steven Bloemen

# High-Precision Studies of Compact Variable Stars

Doctoral Thesis accepted by the KU Leuven, Belgium



Author
Dr. Steven Bloemen
Afdeling Sterrenkunde
Radboud Universiteit Nijmegen
Nijmegen
The Netherlands

Supervisor
Prof. Dr. Conny Aerts
Institute of Astronomy
KU Leuven
Leuven
Belgium

ISSN 2190-5053 ISBN 978-3-319-10282-5 DOI 10.1007/978-3-319-10283-2 ISSN 2190-5061 (electronic) ISBN 978-3-319-10283-2 (eBook)

Library of Congress Control Number: 2014947705

Springer Cham Heidelberg New York Dordrecht London

### © Springer International Publishing Switzerland 2015

This work is subject to copyright. All rights are reserved by the Publisher, whether the whole or part of the material is concerned, specifically the rights of translation, reprinting, reuse of illustrations, recitation, broadcasting, reproduction on microfilms or in any other physical way, and transmission or information storage and retrieval, electronic adaptation, computer software, or by similar or dissimilar methodology now known or hereafter developed. Exempted from this legal reservation are brief excerpts in connection with reviews or scholarly analysis or material supplied specifically for the purpose of being entered and executed on a computer system, for exclusive use by the purchaser of the work. Duplication of this publication or parts thereof is permitted only under the provisions of the Copyright Law of the Publisher's location, in its current version, and permission for use must always be obtained from Springer. Permissions for use may be obtained through RightsLink at the Copyright Clearance Center. Violations are liable to prosecution under the respective Copyright Law. The use of general descriptive names, registered names, trademarks, service marks, etc. in this publication does not imply, even in the absence of a specific statement, that such names are exempt from the relevant protective laws and regulations and therefore free for general use.

While the advice and information in this book are believed to be true and accurate at the date of publication, neither the authors nor the editors nor the publisher can accept any legal responsibility for any errors or omissions that may be made. The publisher makes no warranty, express or implied, with respect to the material contained herein.

Printed on acid-free paper

Springer is part of Springer Science+Business Media (www.springer.com)

### Jury

Prof. Dr. C. Waelkens, chair (KU Leuven, Belgium)

Prof. Dr. C. Aerts, supervisor (KU Leuven, Belgium)

Dr. R.H. Østensen, co-supervisor (KU Leuven, Belgium)

Prof. Dr. H. Van Winckel (KU Leuven, Belgium)

Prof. Dr. T. Hertog (KU Leuven, Belgium)

Dr. H. Hu (SRON, The Netherlands)

Prof. Dr. S.D. Kawaler (Iowa State University, USA)

Prof. Dr. T.R. Marsh (University of Warwick, UK)

### Supervisor's Foreword

Binary stars play a crucial role in astrophysics, not only because they allow stringent tests of stellar evolution models but also because they are laboratories in which specific physical processes, which do not occur in single stars, take place. Understanding these processes is important because at least half of all stars occur in multiple systems. Close binaries are subjected to strong tidal forces and evolve quite differently from single stars, particularly if they undergo phases of spiral-in through a common envelope. The physical description of this phase is a missing ingredient in close binary star evolution.

With the current Ph.D. thesis, the aim was to bring studies of compact binaries to a new level of precision, by relying on a multitude of new kinds of data, original analysis tools, and modern theoretical concepts. The binary targets under study all include a subdwarf star or a white dwarf. These are evolved low-mass stars, which are beyond the stage of core hydrogen fusion and are now burning helium in their non-degenerate core (subdwarfs) or have stopped central nuclear fusion and are being held from collapse thanks to the pressure delivered by their degenerate electrons (white dwarfs). The companions of these compact binaries under study are either sub-solar mass red dwarf stars, intermediate-mass core-hydrogen burning stars or white dwarfs.

Two of the targets under study were intermediate polars. These are binaries with orbital periods up to several hours, containing a rapidly spinning magnetic white dwarf surrounded by an accretion disc. Our aim was to deduce the spin period of the white dwarf and better understand the accretion processes. Since the spin periods of such white dwarfs can be as short as one to a few minutes, our study required ultra-fast high-precision spectroscopy. With the new observing technique based on integration times as short as a few seconds, we could get an unprecedented view on the accretion processes in velocity space.

The NASA Kepler space telescope implied a revolution in exoplanet hunting and stellar variability in general. The nominal mission observed some 150,000 stars, most of which were sampled at half an hour cadence for exoplanet hunting. Luckily, some 512 targets were sampled with a short cadence of about one minute

and this implied a new era in uninterrupted time-resolved  $\mu$  mag precision space photometry of stars, among which compact objects. In this Ph.D. thesis, we used Kepler data to detect, model, and interpret Doppler beaming and Rømer delay in compact binaries. These effects occur when the spectrum of a star in a binary gets Doppler shifted in such a way that its photon emission shows a modulation because it is slightly beamed towards the observer during the orbital motion. We have shown that the Doppler beaming effect in the Kepler light curves is fully compatible with radial velocities obtained from follow-up ground-based spectroscopy. Our study was pioneering in this subject and implies that spectroscopy is no longer needed to derive the orbital motion of binaries when Doppler beaming signals, as have meanwhile been found in many additional binaries observed with the Kepler satellite, can be detected.

Finally, attention was paid to the poorly understood physics of the common envelope phase, which is currently still described by an ad hoc parameter connected with the envelope ejection efficiency. It is assumed that the orbital energy released during the spiral-in is used to eject the common envelope of the two stars. It is a happy circumstance that pulsators occur among the subdwarf stars that must have undergone a common envelope phase in order to explain their existence. Following up on a previous Ph.D. study on theoretical models of subdwarf B stars by our colleague Haili Hu, we embarked on a seismic study to tune the core mass and the thickness of the hydrogen layers of pulsating subdwarfs. A grid of stellar evolution models and their pulsation characteristics has been computed with state-of-the-art physical ingredients, including a full description of atomic diffusion, as it was developed by Haili Hu. On the observational side, the Leuven Institute of Astronomy took up the construction, inauguration, and commissioning of the highprecision multi-colour camera MAIA, installed at the 1.2-m Mercator telescope at La Palma Observatory, specifically designed and built to tackle the science case of asteroseismology of subdwarf B stars. This camera is composed of three highquality CCD chips built by the company e2v for the European Space Agency's Eddington space mission, which was cancelled from the ESA science programme. The plan to exploit the MAIA data in terms of asteroseismology of pulsating subdwarf B stars has just started with the final chapter in this thesis.

The originality of this work lies in the fact that it encompasses engineering (Chap. 7), observational astronomy including time series analysis (Chaps. 2–5), and theoretical astrophysics (Chap. 6). Its breath is impressive and seldom seen in the context of one Ph.D. thesis.

Leuven, May 2014

Prof. Dr. Conny Aerts

### **Preface**

Binary stars are essential laboratories in stellar astrophysics. Observations of binary stars allow us to determine fundamental parameters of stars, such as mass, radius and luminosity, to high precision. These measurements are used to calibrate stellar structure and evolution models. Furthermore, stars in binaries can undergo processes not seen in single stars, such as mass transfer, due to which one star can influence the life of the other.

In this book, we present detailed studies of a variety of compact variable stars as well as new theoretical and instrumental tools to aid such studies. The individual systems studied in this thesis are all binary stars that are undergoing or underwent an epoch of mass transfer from one star to the other.

We start with spectroscopic studies of two moderately magnetic cataclysmic variables (intermediate polars) that are among those with the fastest spinning white dwarfs. Our study of the prototype of the intermediate polars, DQ Her, revealed the presence of a spiral density structure in its accretion disc. By folding our spin resolved spectroscopic measurements on the spin period of the white dwarf, we detected spectral line variations that can clearly not be explained by reprocessing of X-rays in the accretion disc, which was long assumed to be the cause of the variability. We detected very different but equally intriguing spin cycle variations in the spectra of the second intermediate polar we have studied; V455 and our findings indicate that accretion curtain emission is probably observed. Our study of V455 and provides a beautiful demonstration of the power of Electron Multiplying CCDs (EMCCDs) to perform high-speed astronomical observations of relatively faint targets.

Next, we present an in-depth study of light curves of two compact binaries obtained with the *Kepler* satellite. These two targets, KPD1946+4340 and KOI-74, are the first binaries that were found to show very significant Doppler beaming signals. We have modelled the light curves, taking into account the effects of reflection, ellipsoidal modulation, microlensing, Doppler beaming and eclipses. Accurate system parameters were determined, while paying special attention to deriving reliable uncertainty estimates. Our study of KPD1946+4340 presents the first comparison of a star's radial velocity amplitude as measured from

x Preface

spectroscopy and as measured from photometry using the observed Doppler beaming amplitude. We conclude that the photometric and spectroscopic radial velocity amplitudes are in agreement, for both targets, and that Doppler beaming can successfully be used to measure radial velocities. In the case of KOI-74 we have shown how one can derive the mass ratio of selected binaries from photometry alone, by exploiting Doppler beaming and light travel time (Rømer) delay signals.

Finally, we discuss ongoing efforts in the field of asteroseismology of hot subdwarf stars. We present a grid of evolutionary subdwarf B star models that are computed while taking into account diffusion processes. We show that the Fe and Ni enhancements in the pulsation driving regions are higher than previously assumed, and we show the influence on the predicted instability strips for *p*- and *g*-mode pulsators. Using the grid of subdwarf structure models, synthetic amplitude ratios of pulsation modes observed in different colour filters are computed. Such amplitude ratios are sensitive to the spherical degree of the pulsation modes and provide valuable observational constraints to asteroseismic studies. The new 3-channel Mercator Advanced Imager for Asteroseismology, MAIA, was developed to provide measurements of pulsation amplitudes in different colour bands. We end this thesis with a status update of the commissioning of this new camera, which was installed at the Mercator telescope in the Spring of 2012.

All efforts presented in this book where the subject of my Ph.D. research, which I conducted at the University of Leuven from September 2009 until May 2013 under the supervision of Prof. Conny Aerts and Dr. Roy Østensen. It was a very rewarding experience to work with great colleagues on such a variety of topics, using state-of-the-art techniques and instrumentation. I hope that, through this diversity, the readers of this book will appreciate the beautiful and sometimes unexpected ways in which binary stars present us with clues to what they look like and how they live.

### Acknowledgments

I am greatly indebted to my supervisors, Conny Aerts and Roy Østensen for their guidance, their advice, and for the opportunities they offered me. I wish to thank everyone I have had the pleasure to collaborate with. Tom Marsh and Danny Steeghs deserve a special mention, for the inspiring time during my Erasmus stay in Warwick and the continued collaboration after my return to Leuven. A special note of thanks also to Haili Hu, for providing me with her codes, and for all her efforts to help me even after she left the astronomical scene.

I wish to thank the Mercator teams in La Palma and Leuven, and the Kepler teams, for providing the great instrumentation that was essential for my work.

Many thanks to my colleagues in Leuven for the great times we had.

A big thanks to my friends and family for their continuous support.

Finally, to Valentina, thank you for being there when I needed you, for being the wonderful person you are.

The research presented in this Ph.D. thesis was based on funding from the European Research Council under the European Community's Seventh Framework Programme (FP7/2007–2013)/ERC grant agreement n°227224 (PROSPERITY) and from the Fund for Scientific Research of Flanders, grant agreement G.0332.06. The CCDs of the MAIA camera were developed by e2v in the framework of the Eddington mission project and are owned by the European Space Agency; they were offered on loan to the Institute of Astronomy of KU Leuven, Belgium, for use on the 1.2-m Mercator telescope at La Palma Observatory, Canary Islands.

# **Contents**

1	Intr	oduction	1
	1.1	Stellar Evolution	2
		1.1.1 Single Stars	2
		1.1.2 Binary Stars	3
	1.2	Instrumentation Used in This Thesis	5
		1.2.1 ISIS Spectrograph at the William Herschel Telescope	5
		1.2.2 The <i>Kepler</i> Space Telescope	6
	1.3	Doppler Tomography	7
	1.4	Outline of This Thesis	8
	Refe	erences	10
2	Spir	n-Resolved Spectroscopy of the Intermediate Polar	
	_	Her	13
	2.1	DQ Her Among the Intermediate Polars	13
	2.2	Doppler Maps	15
		2.2.1 Balmer Lines	15
		2.2.2 Spiral Structure on the He I λ4472 and λ6678 Maps	19
		2.2.3 He II λ4686	22
		2.2.4 Discussion	22
	2.3	Spin Phase Dependence of the Spectral Lines	23
		2.3.1 Spin Periodicity in the Red-Shifted Wing	
		of He II λ4686	23
		2.3.2 71s or 142s Periodicity in He II λ4686?	27
		2.3.3 Can 71s Be the Beat Frequency?	27
		2.3.4 Spin Periodicity in the Balmer and He I Lines	29
	2.4	Conclusions	30
	Refe	erences	31
	11011	Actives	
3	Ren	narkable Spectral Variability on the Spin Period	
		he Accreting White Dwarf in V455 And	33
	3.1	The Cataclysmic Variable V455 And	33
		•	

xiv Contents

	3.2	Analysis	35
		3.2.1 Frequency Analysis	35
		3.2.2 Variations on the Orbital Period	37
		3.2.3 Variations on the WD Spin Period	38
	3.3	Summary	39
	Refe	erences	41
4	Kepi	ler Observations of the Beaming Binary KPD 1946+4340	43
	4.1	KPD 1946+4340 Among the Subdwarf B Stars	44
	4.2	Observations, Radial Velocities and Updated Ephemeris	45
	4.3	Light Curve Analysis	47
		4.3.1 Gravity Darkening and Limb Darkening Coefficients	48
		4.3.2 Doppler Beaming Factor	48
		4.3.3 Light Curve Model	50
		4.3.4 Markov Chain Monte Carlo Simulation	51
		4.3.5 Variability in Residuals	55
	4.4	Spectroscopic Analysis	56
	4.5	Discussion	57
	4.6	•	60
	Refe	erences	60
5	Mas	ss Ratio from Doppler Beaming and Rømer Delay	
			63
	5.1	Kepler Object-of-Interest 74	64
	5.2	Spectroscopy	65
	5.3	Kepler Photometry	67
		1 &	68
		5.3.2 Gravity Darkening, Limb Darkening and Doppler	
		Beaming Coefficients	70
		5.3.3 Modelling Code and MCMC Setup	71
			73
		•	77
	5.4	Summary	78
	Refe	erences	79
6	A N	lew Grid of Evolutionary Subdwarf B Star Models	
	and	Their Pulsational Properties	81
	6.1	Introduction	81
	6.2		83
	6.3	Instability Strips	83
	6.4	Amplitude Ratios	88
		6.4.1 Changes in the Amplitude Ratios During	
		the Evolution	89
		6.4.2 Comparison with Previous Work	89

Contents xv

	6.5 Refe		93 94
7			
,	7.1	in the man man and an	
	7.1		٠.
			- •
			_
	7.2		
	7.3	Instrument Calibration	04
		7.3.1 Flatfields	04
		7.3.2 System Throughput	06
	7.4	First Results	10
			10
		· ·	12
	7.5		14
	Refe		14
8	Con	ductions and Future Progresses	17
o	8.1		
	0.1		- '
	8.2	<b>r</b>	
	Refe	rences	21
Cı	ırricu	um Vitae	Mercator Advanced Imager for Asteroseismology   97
Li	st of ]	Publications	25
In	dex .		31

# Chapter 1 Introduction

The laboratory of an observational astronomer is the Universe itself. Compared to the human lifetime and the typical length of astronomical observation campaigns, the evolutionary time scales of stars are extremely long. Astronomical research, and certainly stellar astronomy, therefore often boils down to connecting the dots. It starts with studying individual objects in a variety of different evolutionary phases, trying to understand the physical processes that are going on and figuring out evolutionary paths that logically connect the observed systems.

The study of stellar structure and stellar evolution is not only useful to understand the lives of the stars themselves, but is also crucial to understand several other aspects of astrophysics, from small dust grains up to the size and age of the Universe. Exo-planet research, for example, relies on our knowledge of the host stars of planetary systems. Another example is the use of stars and stellar phenomena, such as supernovae, as standard candles to calibrate the cosmic distance scales. Apart from playing this central and crucial role in astrophysics, stars can be considered as ideal laboratories to test our knowledge of physics in the most extreme conditions of density, temperature and pressure, at the largest speeds and the highest variety of scales.

Although the general picture of stellar evolution is relatively well understood, some facets remain unclear. In this thesis we focus on observational studies of compact stars in late evolutionary stages. The stars studied in detail in this thesis are compact stars in binary systems. The reason for studying stars that have a stellar companion is twofold. Firstly, the evolution of a star can be drastically influenced by the presence of a companion star in a close orbit, governed by physics that is not seen in single stars. Secondly, the mere fact that a star is a component of a binary often offers extra means to uncover the object's detailed nature compared to the case of a single star. Besides the studies of selected binary stars, this thesis also includes work on theoretical and observational tools for the studies of compact stars via the technique of asteroseismology.

In the following sections, a brief introduction is given to stellar evolution, binary stars and the instrumentation used for this work.

1

2 1 Introduction

### 1.1 Stellar Evolution

Extensive monographs on stellar evolution have been published recently, e.g., Maeder (2009) and Kippenhahn et al. (2013), to which we refer for a detailed discussion. Here, we limit to a brief summary of single-star evolution while we highlight the basics of binary-star evolution focussing on some basic ingredients that are of relevance for the research performed in this thesis.

### 1.1.1 Single Stars

Stars are born when a cloud of gas and dust collapses under its own gravity. The temperature of the gas in the cloud then rises, and the cloud fragments into hot cores. These cores contract, and the internal temperature rises until it is high enough to allow hydrogen fusion to take place. A star spends most of its life in this stage, burning hydrogen into helium in its core, which we call the main sequence stage. During this stage, the pressure force counteracts the gravitational force. When a star runs out of hydrogen in the core, the core starts to shrink. The further evolution of the star is highly dependent on its mass. In stars with masses up to  $\sim 2.4 \, \mathrm{M}_{\odot}$  (Solar mass), the helium core contracts until the gas reaches an electron-degenerate state in which the pressure of the degenerate electrons prevents the core from contracting further. Meanwhile, the temperature in the layers above the core becomes high enough to accommodate further hydrogen burning, adding helium to the core. The outer layers of the star gradually expand and the star becomes a red giant. The core gets more massive and its internal temperature rises until helium burning is initiated. In a nondegenerate environment, a temperature increase would cause the core to expand and cool, which stabilizes the burning. In the degenerate core, however, the pressure of the degenerate electrons dominates over the gas pressure. The pressure therefore does not increase when the temperature rises, and the helium burning starts as a runaway process, which causes a sudden temperature increase. As more and more energy becomes available, the electrons can populate higher energy levels, due to which the electron degeneracy eventually gets lifted. The core then experiences an epoch of stable helium burning. In stars with masses above  $\sim 2.4 \, \mathrm{M}_{\odot}$ , the run-away helium burning phase is avoided because helium is ignited in the core before degeneracy sets in.

Core helium burning leads to the production of carbon and oxygen in the core. Massive stars  $(M\gtrsim 9\,M_\odot)$  can have many burning phases in which increasingly heavier nuclei are formed, until the core consists of iron. No energy is released anymore by nuclear fusion to elements more massive than iron, and nuclear fusion therefore halts. If the mass of the iron core exceeds the Chandrasekhar mass of  $\sim\!1.4\,M_\odot$ , the electron degeneracy pressure cannot provide enough support anymore and the core collapses. Gravitational energy is released and the star explodes in a supernova. Stars with a remnant core of more than  $\sim\!3\,M_\odot$  end their evolution as

1.1 Stellar Evolution 3

black holes. If the core mass is below  $\sim 3 \, M_{\odot}$ , neutron degeneracy pressure can withstand the gravitational forces. In this case, the stellar remnant is a neutron star.

In stars born with less than  ${\sim}6\,M_{\odot}$ , essentially no heavier elements than carbon and oxygen are produced. When it runs out of helium, the carbon–oxygen core of the star will gradually contract and become degenerate at that stage. The star becomes a red supergiant as it reaches the asymptotic giant branch. In this phase, strong stellar winds blow off the outer layers of the star. The star loses enough mass for the core to become less massive than the Chandrasekhar limit, and a supernova explosion is avoided. The remaining carbon-oxygen cores are known as white dwarfs and form the final phase of the evolution. In stars with a mass between  ${\sim}6$  and  ${\sim}9\,M_{\odot}$ , carbon burning can take place. These stars end their lives as oxygen-neon-magnesium white dwarfs.

### 1.1.2 Binary Stars

A gas cloud out of which stars are born typically gives birth to several thousands or even millions of stars. Stars therefore often find themselves gravitationally bound to one or more nearby stars. Binary stars and systems with more than two components are more common than single stars. It is estimated that about two thirds of the stars have had at least one companion.

If the stars in a binary are in a wide orbit, stellar evolution proceeds as if both stars were single stars. In close binary stars, where the separation between the stars is small enough for the stars to feel the gravitational pull of the other, stars can interact in a variety of ways. Radiation from one star can heat the other, and stars can get aspherical due to the gravitational pull from the companion, etc.

The equipotential surface within which matter is gravitationally bound to a star in a binary has a droplet shape and is called the star's Roche lobe (see Fig. 1.1).

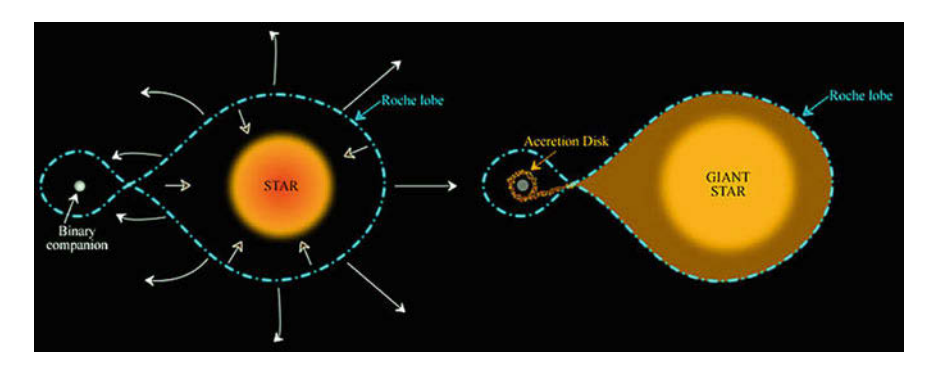


**Fig. 1.1** The Roche lobe of the stars in a binary system. Within the Roche lobe, material is gravitationally bound to the star. On the *left*, a detached system is shown. On the *right*, one star overflows its Roche volume and mass is transferred to its companion. © Swinburne University of Technology; used with permission

4 1 Introduction

If a star fills its Roche lobe, either because the star expands or the Roche lobe volume decreases, mass is transferred from one star to the other (see e.g. Paczyński 1971; Iben and Livio 1993; Podsiadlowski 2008). This mass transfer can be stable or unstable, and the phenomenon is often not well understood. It is estimated that about  $\sim\!25\,\%$  of binaries undergo mass transfer at some stage of their evolution (Willems and Kolb 2004). The initial orbital periods of these binaries are typically  $\lesssim\!10$  years.

Stable Roche lobe overflow occurs when the star that is losing mass expands less rapidly or shrinks faster than it's Roche lobe. Unstable Roche lobe overflow occurs when the donor star reacts to the mass transfer by increasing its radius faster than its Roche lobe increases, or by decreasing its radius less rapidly than its Roche lobe shrinks. Mass transfer then becomes a runaway effect.

If the accreting star cannot instantly accrete all the material that gets transferred from the donor star, an accretion disc can be formed or, in the more extreme case, the transferred material can fill the accreting star's Roche lobe completely and the system will end up in a common-envelope phase where the cores of the two stars sit within the envelope of the donor star. When an accretion disc forms, some material carries away angular momentum while other gas moves inwards. The angular momentum transport mechanism of gas in a disc is one of the major unknowns in binary evolution models. In a common-envelope system, drag forces between the stellar cores and the shared envelope will cause the stars to spiral inwards. This way, the orbital period can go down from several years to only a few hours. Ultimately, enough orbital energy can be transferred to eject the envelope. The common-envelope ejection phase, and more precisely the condition that leads to it, is another important uncertainty in binary evolution theory.

The binary stars that are studied in this thesis are undergoing or have undergone mass transfer. In Chaps. 2 and 3, two cataclysmic variables are studied. Cataclysmic variables, in which a white dwarf accretes mass from a low mass companion via an accretion disc, are typical examples of systems that undergo stable mass transfer. The cataclysmic variables studied in this thesis are of a particular type called intermediate polars. In such systems, the accreting white dwarf is moderately magnetic  $(B \lesssim 10MG)$  and matter gets accreted via the magnetic field lines to the magnetic poles of the white dwarf. Depending on the details of system, the accretion disc can be completely disrupted by the magnetic field, or the accretion disc can appear truncated as is the case in the systems studied here. An artist's impression of an intermediate polar is shown in Fig. 1.2.

In Chap. 4 a close binary that consists of a white dwarf and a subdwarf B star (sdB) is studied. SdBs are core helium burning stars with a thin hydrogen envelope. The evolutionary paths that lead to the formation of sdBs are not well understood. Since the majority of subdwarf B stars are found in close binaries (Maxted et al. 2001), the idea that sdBs are the products of binary evolution channels has gained ground. In such a scenario, a red giant star loses most of its hydrogen envelope in a mass transfer stage to become an sdB (Han et al. 2002). In the particular case of Chap. 4, the star is very likely to be a post common-envelope ejection system. The tools presented in

1.1 Stellar Evolution 5

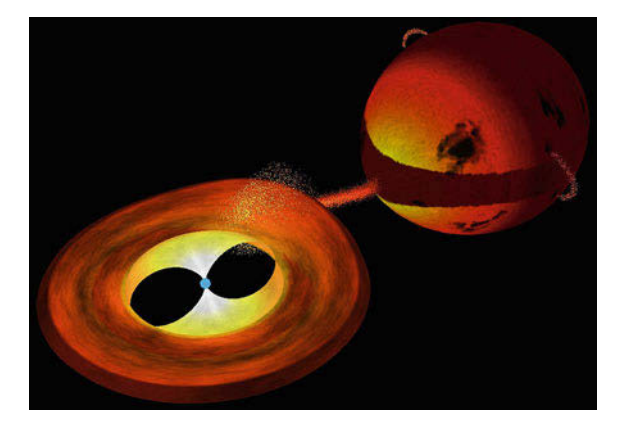


**Fig. 1.2** Artist impression of an intermediate polar. A white dwarf accretes mass from its companion that is overflowing its Roche lobe. The mass is accreted via an accretion disc. The inner part of the disc is disrupted by the magnetic field of the white dwarf. Mass is accreted via the magnetic field lines onto the magnetic poles of the white dwarf. © Andrew Beardmore, University of Leicester; used with permission

Chaps. 6 and 7 are being developed to check the evolutionary scenario of sdBs using asteroseismology.

The target discussed in Chap. 5 is a binary star consisting of a white dwarf with a main sequence companion. This system has undergone a period of stable Roche lobe overflow.

### 1.2 Instrumentation Used in This Thesis

Advances in observational astrophysics are often driven by the availability of new, more advanced instrumentation. For this thesis, we made use of optical spectroscopy and photometry, obtained with a variety of instruments. In particular, we made extensive use of spectroscopic data obtained with the ISIS spectrograph at the William Herschel Telescope and of photometric data obtained with the *Kepler* space telescope. Both are introduced below. An introduction to the new Mercator Advanced Imager for Asteroseismology (MAIA) constructed in Leuven is given in Chap. 7.

### 1.2.1 ISIS Spectrograph at the William Herschel Telescope

The Intermediate dispersion Spectrography and Imaging System (ISIS) installed at the 4.2-m William Herschel Telescope (WHT, Roque de los Muchachos, La Palma, Spain) is a double-armed, medium-resolution long-slit spectrograph. It saw first light in 1989, but has been upgraded several times since. When our 1998 data of DQ Her

6 1 Introduction

(Chap. 2) were obtained, ISIS was equipped with 1 megapixel Charge Coupled Devices (CCDs). A full readout of these CCDs took several tens of seconds. To minimize the deadtime of our cadence-critical observations, the CCDs were operated in a drift mode. Instead of illuminating the full CCD during the exposure, only a few rows were used, and rapidly shifted to unused areas of the CCD after every exposure.

This drift technique was a predecessor of what is nowadays achieved with frame transfer CCDs, which have a dedicated on-chip image storage area that is as large as the illuminated part to allow to read out one image while the next one is already being taken. Currently, ISIS users have the option to use the QUCAM2 and QUCAM3 CCDs, which are known as Low Light Level CCDs (L3CCDs) or Electron Multiplier CCDs (EMCCDs). As the name indicates, apart from a frame transfer buffer, they also contain an electron multiplication stage which consists of a series of serial stages in the output register that are clocked with a higher voltage than required for simple charge transfer. The charge-carrier electrons are accelerated by the large electric fields and, by impact ionisation, cause a single electron to lead to an avalanche of several hundreds of electrons. The advantage is that the readout-noise, which is normally the critical noise source at very low count levels, becomes negligible compared to signal that results from a single observed photon.

By using a frame transfer buffer to reduce the dead time between subsequent exposures and an electron multiplication stage to overcome the read-out noise at low count levels, one can obtain observations at fast cadence at a low penalty compared to long exposures using standard CCDs. This has been crucial to obtain the observations of V455 And presented in Chap. 3.

ISIS was also used with standard CCDs in normal read-out mode to obtain spectra for radial velocity measurements of *Kepler* Object of Interest KOI-74 (Chap. 5).

### 1.2.2 The Kepler Space Telescope

NASA's *Kepler* space telescope was launched in March 2009. The mission was designed to search for exo-planets around distant stars in our Milky Way. The primary goals are to detect terrestrial planets in the habitable zone of distant stars, and to determine how common planets are. To achieve this, the satellite monitors the brightness of about 150,000 stars in the Cygnus and Lyra constellations, simultaneously and nearly without interruption. It observes at a 6s cadence. Due to telemetry limitations, the data of most stars is stacked on board into  $\sim$ 30 min observations, and for 512 carefully selected stars into  $\sim$  1 min exposures (Gilliland et al. 2010). *Kepler* achieves an unrivalled photometric precision of about 50 parts per million on a 30 min integration of a 12th magnitude star (Jenkins et al. 2010). These brightness measurements allow one to detect planets using the transit method: whenever a planet passes in front of its host star, is casts a shadow on the satellite. This causes a periodic dip in the observed brightness of the star. To date, over 2000 planet candidates have been detected with *Kepler* (Batalha et al. 2012). Noteworthy planet discoveries

include a 6-planet system (Lissauer et al. 2011) and circumbinary planets (e.g. Doyle et al. 2011; Welsh et al. 2012). Although Earth-like planets have been found, as well as planets in the habitable zone, an Earth-analogue in its habitable zone has not been found yet, but that is presumably only a matter of time.

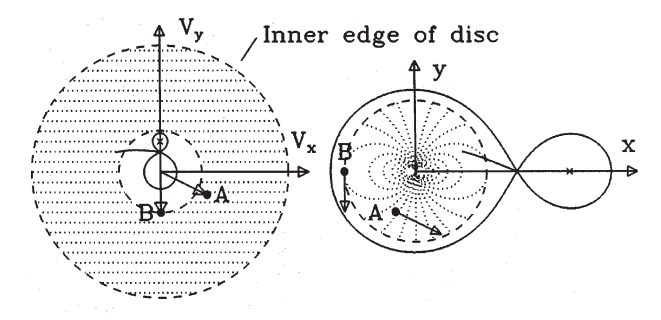
The high quality, continuous brightness measurements that Kepler delivers are not just useful for the planet hunt the mission was primarily designed for. It does not only allow us to study planets around stars, but also the observed stars themselves. The research fields of asteroseismology and eclipsing binary stars in particular have benefitted tremendously from Kepler data. The key to Kepler's success is that it offers a rare combination of high quality and high duty cycle observations that span many years, and that for thousands of stars simultaneously. One can thus study a single target in detail, but the large sample also allows one to do statistical studies and to find odd systems and events which are otherwise hard to discover. Notable examples of Kepler's impact in the field of binary stars are the detections of surprising brightenings in close eccentric binaries (e.g. Thompson et al. 2012), the detection of Doppler beaming (e.g. this thesis van Kerkwijk et al. 2010), orbit determinations from pulsation frequency modulations (Shibahashi and Kurtz 2012; Telting et al. 2012) and the detection of more than 2,100 eclipsing binaries (Prša et al. 2011; Slawson et al. 2011) including a number of triple and higher order systems (e.g. Derekas et al. 2011). In the field of asteroseismology, arguably, the most notable result is the observation of modes that probe the cores of red giants and allows one to measure their internal rotation rates (Beck et al. 2011, 2012; Deheuvels et al. 2012). The satellite also led to the establishment of a new class of pulsators in which the pulsation modes are tidally excited by interaction with a companion star in a close eccentric orbit (Welsh et al. 2011; Fuller and Lai 2012; Hambleton et al. 2012).

### 1.3 Doppler Tomography

While the analysis of photometric time series to study variable phenomena in astronomy is rather standard practice (see e.g. Aerts et al. 2010, Chap. 5) this is less so for spectroscopic time series. When a theoretical model of the underlying variability is not available, the interpretation of spectroscopic data is often challenging.

In Chaps. 2 and 3, spectroscopic measurements of two intermediate polars are presented. To visualise the observed changes in spectral lines with orbital phase, we relied on a technique called Doppler tomography. Starting from spectra covering the orbit of a binary, one can use this technique to make an image in velocity space that shows the components that contribute to the emission of a certain spectral line. Doppler tomography was put forward as a technique to make images of binary systems with accretion discs by Marsh and Horne (1988). In Fig. 1.3, it is shown what an image of a cataclysmic variable looks like in both position and velocity coordinates. The image on the right shows the white dwarf (at the origin of the coordinate system) with its accretion disc, and the donor star to the right of it. The system is assumed to be rotating anticlockwise around its centre of mass. The white

8 1 Introduction



Velocity coordinates Position coordinates

**Fig. 1.3** A cataclysmic variable in velocity coordinates and position coordinates. Using Doppler tomography, spectra taken over the orbital period of a binary can be converted into an image in velocity coordinates, as explained in the text. Figure taken from Marsh and Horne (1988)

dwarf and the donor star therefore have no velocity component in the x-direction. In the velocity image on the left, the donor star is indicated with a cross, at positive velocity in the y-direction, and zero velocity in the x-direction. In the accretion disc, material closer to the white dwarf (point A) has a higher velocity than material at the outer edge of the disc (point B). In velocity space, the disc will therefore appear inside-out: matter that orbits closer to the central object has a higher speed and will appear further away from the white dwarf in the velocity image.

A spectrum taken at a certain orbital phase can be interpreted as a projection of the velocity image, in a direction that rotates during the binary orbit. This is illustrated in Fig. 1.4, which shows how two spectra show projections of the velocity image at two different orbital phases, a quarter of an orbit apart. The spot in the velocity image is receding from the observer at phase 0.25 and shows up in the redshifted part of the spectrum (shown on the right). At phase 0.5, the spot has a small velocity component towards the observer, and shows up in the blueshifted part of the spectrum (bottom). The orbital motion therefore allows one to probe the projected Doppler image from different directions.

In this thesis, we use the maximum entropy method as presented in Marsh and Horne (1988) to convert spectra taken at different orbital phases into an image of the line emitting regions of the binary in velocity space. This method attempts to find the least structured velocity image that fits the data well enough (defined by a  $\chi^2$  criterion). Examples of the use of this method and the interpretation of the resulting Doppler maps are presented for DQ Her in Sect. 2.2 and for V455 And in Sect. 3.2.2.

### 1.4 Outline of This Thesis

While stars seldomly show stellar evolution in action on timescales of a few years or decades, they often do appear differently on much shorter timescales. This variability reveals clues about the nature of the object and the ongoing physical processes. In this

9

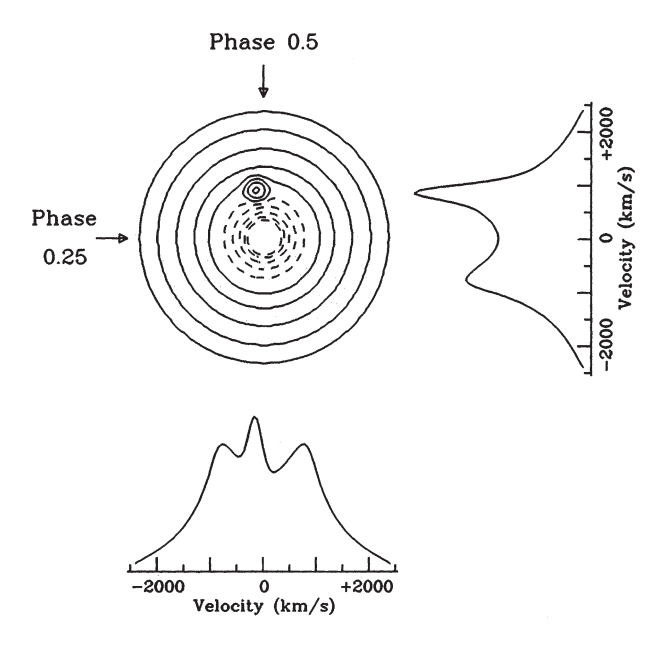


**Fig. 1.4** Spectra are projections of the image in velocity coordinates. The direction in which the images are projected rotates with orbital phase. In Doppler tomography, one attempts to do the opposite, creating the image in velocity coordinates from spectra taken at different orbital phases. Figure taken from Marsh and Horne (1988)

thesis, we present several studies of compact variable stars of quite diverse nature, making use of state-of-the-art instrumentation.

In Chaps. 2 and 3 we discuss fast spectroscopy of two intermediate polars with rapidly spinning white dwarfs: DQ Her with a spin period of 72 or 144 s and V455 And with a spin period of 68 s. The main goal is to gain insight in the ongoing accretion process by studying the variability in emission lines over the spin cycle of the white dwarf and over the orbital cycle of the binary. Initially, the explanation for observed variations in the light intensity of intermediate polars was that it was caused by a light house effect of X-ray emission from the white dwarf's magnetic poles on the accretion disc. A sketch of the idea behind this effect is shown in Fig. 1.5. More recently it was proposed that emission from accretion curtains might be seen. These accretion curtains are formed by material that is being accreted from the inner part of the disc along the magnetic field lines to the white dwarf's magnetic poles, as depicted in Fig. 1.2.

In Chaps. 4 and 5 we present an analysis of *Kepler* observations of two close eclipsing binaries that have undergone a period with mass transfer between the components: KPD 1946+4340 and KOI-74. We present light curve models that explain the observed variability and derive accurate system parameters. Such system parameters are important to calibrate stellar evolution scenarios. The two systems presented were the first two compact binaries with a highly significant Doppler beaming sig-

10 1 Introduction

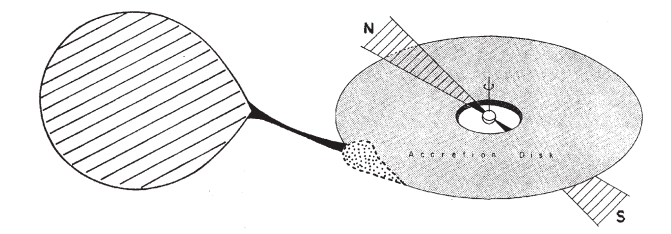


**Fig. 1.5** Artist impression of an intermediate polar. When material is accreted on the magnetic poles of the white dwarf, gravitational energy is released and emitted in the form of X-rays. As the white dwarf is spinning rapidly, these X-rays might act as light house beams, illuminating the accretion disc. Figure taken from Patterson (1994)

nal in their light curves. We present the first comparison of a star's radial velocity amplitude determined from the observed Doppler beaming amplitude with the amplitude seen in spectroscopy, and confirm that the two are in agreement. This opened up the possibility to use Doppler beaming signals to determine stellar masses. We also present the very first application of a light travel time delay (Rømer delay) to determine the mass ratio of a binary from photometry alone.

While Chaps. 2–5 represent research that is already published in peer-reviewed papers, the next two chapters present ongoing work related to the study of subdwarf B stars using asteroseismology. In Chap. 6 we present a new grid of evolutionary sdB models that are computed taking diffusion processes such as radiative levitation and gravitational settling into account. This leads to a much better prediction of pulsation mode excitation compared to the case where these two effects are not taken into account in the model and pulsation computations. In Chap. 7 we present the new multi-colour camera MAIA that was installed at Mercator in 2012.

We end this thesis with concluding remarks and future prospects in Chap. 8.

### References

Aerts, C., Christensen-Dalsgaard, J., & Kurtz, D. W. (2010). *Asteroseismology*. Heidelberg: Springer.

Batalha, N. M., Rowe, J. F., Bryson, S. T., et al. (2012). arXiv:astro-ph/1202.5852.

Beck, P. G., Bedding, T. R., Mosser, B., et al. (2011). Science, 332, 205.

Beck, P. G., Montalban, J., Kallinger, T., et al. (2012). Nature, 481, 55.

Deheuvels, S., García, R. A., Chaplin, W. J., et al. (2012). ApJ, 756, 19.

Derekas, A., Kiss, L. L., Borkovits, T., et al. (2011). Science, 332, 216.

Doyle, L. R., Carter, J. A., Fabrycky, D. C., et al. (2011). Science, 333, 1602.

Fuller, J., & Lai, D. (2012). MNRAS, 420, 3126.

Gilliland, R. L., Jenkins, J. M., Borucki, W. J., et al. (2010). ApJ, 713, L160.

Hambleton, K., Kurtz, D., Prša, A., Bloemen, S., & Southworth, J. (2012). In: M. T. Richards, & I. Hubeny (Eds.), IAU Symposium, vol. 282 of IAU Symposium, KIC 4544587: An Eccentric, Short Period Binary with δ Scuti Pulsations and Tidally Excited Modes (pp. 77–78).

Han, Z., Podsiadlowski, P., Maxted, P. F. L., Marsh, T. R., & Ivanova, N. (2002). MNRAS, 336, 449.

References 11

Iben, I. J., & Livio, M. (1993). PASP, 105, 1373.

Jenkins, J. M., Caldwell, D. A., Chandrasekaran, H., et al. (2010). ApJ, 713, L120.

Kippenhahn, R., Weigert, A., & Weiss, A. (2013). Stellar structure and evolution. Berlin: Springer.

Lissauer, J. J., Fabrycky, D. C., Ford, E. B., et al. (2011). Nature, 470, 53.

Maeder, A. (2009). Physics, formation and evolution of rotating stars. Berlin: Springer.

Marsh, T. R., & Horne, K. (1988). MNRAS, 235, 269.

Maxted, P. f. L., Heber, U., Marsh, T. R., & North, R. C. (2001). MNRAS, 326, 1391.

Paczyński, B. (1971). ARA&A, 9, 183.

Patterson, J. (1994). PASP, 106, 209.

Podsiadlowski, P. (2008). In: A. Evans, M. F. Bode, T. J. O'Brien, & M. J. Darnley (Eds.), RS Ophiuchi (2006) and the Recurrent Nova Phenomenon, vol. 401 of Astronomical Society of the Pacific Conference Series, The Evolution of Close Binaries (p. 63).

Prša, A., Batalha, N., Slawson, R. W., et al. (2011). AJ, 141, 83.

Shibahashi, H., & Kurtz, D. W. (2012). MNRAS, 422, 738.

Slawson, R. W., Prša, A., Welsh, W. F., et al. (2011). AJ, 142, 160.

Telting, J. H., Østensen, R. H., Baran, A. S., et al. (2012). A&A, 544, A1.

Thompson, S. E., Everett, M., Mullally, F., et al. (2012). ApJ, 753, 86.

van Kerkwijk, M. H., Rappaport, S. A., Breton, R. P., Justham, S., Podsiadlowski, P., & Han, Z. (2010). *ApJ*, 715, 51.

Welsh, W. F., Orosz, J. A., Aerts, C., et al. (2011). ApJS, 197, 4.

Welsh, W. F., Orosz, J. A., Carter, J. A., et al. (2012). Nature, 481, 475.

Willems, B., & Kolb, U. (2004). A&A, 419, 1057.

## Chapter 2 Spin-Resolved Spectroscopy of the Intermediate Polar DQ Her

**Abstract** We present high-speed spectroscopic observations of the intermediate polar DQ Herculis. Doppler tomography of two He I lines reveals a spiral density structure in the accretion disc around the white dwarf primary. The spirals look very similar to the spirals seen in dwarf novae during outburst. DQ Her is the first well established intermediate polar in which spirals are seen, that are in addition likely persistent because of the system's high mass transfer rate. Spiral structures give an alternative explanation for sidebands of the WD spin frequency that are found in IP light curves. The Doppler tomogram of He II λ4686 indicates that a large part of the emission is not disc-like. Spin trails of spectra reveal a pulsation in the He II λ4686 emission that is believed to result from reprocessing of X-rays from the white dwarf's magnetic poles in the accretion flow close to the WD. We confirm the previous finding that the pulsation is only visible in the red-shifted part of the line when the beam points to the back side of the disc. The absence of reprocessed light from the front side of the disc can be explained by obscuration by the front rim of the disc, but the absence of extra emission from the blue-shifted back side of the disc is puzzling. Reprocessing in accretion curtains can be an answer to the problem and can also explain the highly non-Keplerian velocity components that are found in the He II  $\lambda 4686$  line. Our spin trails can form a strong test for future accretion curtain models, with the possibility of distinguishing between a spin period of 71 s or 142 s. Spin trails of data taken at selected orbital phases show little evidence for a significant contribution of the bright spot to the pulsations and allow us to exclude a recent suggestion that 71 s is the beat period and 70.8 s the spin period.

### 2.1 DQ Her Among the Intermediate Polars

DQ Her is the prototype of the intermediate polars, which are therefore also called 'DQ Herculis stars'. Intermediate polars are cataclysmic variables with moderately magnetic white dwarfs. The magnetic field in such systems is not strong enough to synchronise the binary orbit and the spin period of the white dwarf (contrary to the

This chapter is based on S. Bloemen, T.R. Marsh, D. Steeghs and R.H. Østensen, Monthly Notices of the Royal Astronomical Society, 2010, vol. 407, pp. 1903–1912.

<sup>©</sup> Springer International Publishing Switzerland 2015

S. Bloemen, High-Precision Studies of Compact Variable Stars,

systems with higher magnetic fields, called polars) but it disrupts the inner part of the accretion disc. The disc material finally accretes on the magnetic poles of the white dwarf via the magnetic field lines. The gravitational energy that gets released is radiated in X-rays, which results in X-ray beams from the magnetic poles of the white dwarf. Reprocessing of X-rays from the beams in the accretion disc or on the surface of the secondary star leads to periodicities in photometry and spectra, which are a very important characteristic of IPs. An excellent review on intermediate polars can be found in Patterson (1994).

Walker (1954, 1956) first reported a periodic 71 s variation in DQ Her's light curve. Spectroscopic studies revealed that a disc is present in the system Greenstein and Kraft (1959). Warner et al. (1972) found a phase shift in the 71 s pulsations during eclipse, which was later confirmed (e.g., Patterson et al. 1978; Zhang et al. 1995). Several studies (see e.g., Chanan et al. 1978; Chester 1979; Petterson 1980) showed that this phase shift is naturally explained by pulsations in the light curve that arise from illumination of the accretion disc by energetic beams from the white dwarf with the front side of the disc hidden behind the disc rim.

For decades a debate has gone on as to whether the true spin period of the white dwarf is the observed 71 s or 142 s. In the latter case, the 71 s periodicity that is observed could be the result of two beams illuminating the disc with a 0.5 phase difference. In power spectra of photometric data, usually no power is found at 142 s (e.g., Kiplinger and Nather 1975; Wood et al. 2005). The radiation beams from the two magnetic poles of the white dwarf should thus be identical to a very high approximation, which is not impossible but at least physically difficult to achieve. Weak photometric evidence of a 142 s periodicity was, however, presented in Nelson (1975) and Schoembs and Rebhan (1989). Furthermore, the models for the phase shift that were presented in the 1970 and 1980s did not rule out a 142 s spin period. Zhang et al. (1995) claimed to have found a better agreement with their observations for a 142 s model than for a 71 s model. In polarimetric data, Kemp et al. (1974) and Swedlund et al. (1974) found a stronger 142 s than 71 s periodicity. In the polarimetric study by Butters et al. (2009), only the 142s periodicity was searched for (and detected but with low significance) because the time resolution and signal-to-noise ratio of the dataset were not high enough to allow a study of the 71s periodicity (O. Butters, private communication). Spectroscopy has so far supported both the 71 s and 142 s spin periods (Chanan et al. 1978; Martell et al. 1995). All things considered, it is not clear yet which of the spin periods is to be preferred.

DQ Her is eclipsing, with an inclination of  $\approx 89^{\circ}$  (Petterson 1980). It has an orbital period of 4 h 39 m and consists of a white dwarf with a mass near 0.6  $M_{\odot}$  and a red dwarf companion with a mass near 0.4  $M_{\odot}$  (Horne et al. 1993).

This chapter relies on the observations and the data reduction process discussed in Bloemen et al. (2010), to which we refer for details, and summarized in Table 2.1. In Sect. 2.2, the variations in the spectral lines on the timescale of the binary orbit are studied using Doppler tomography to get more insight in the binary's structure. Next, in Sect. 2.3, the dependence on the spin phase is analysed in an attempt to get clues about the true spin period and the X-ray reprocessing regions. Finally, the conclusions are given in Sect. 2.4.

2.2 Doppler Maps 15

Date	UT	Seeing	Instrument	Grating	Exp.	Number
					time (s)	
08-09/07/1998	22:32-04:19	≈1.2	ISIS blue arm	R1200B	5.1	2,419
		arcsec				
			ISIS red arm	R600R	15.1	908
09-10/07/1998	22:48-05:25	1–2 arcsec	ISIS blue arm	R1200B	5.1	3,181
			ISIS red arm	R600R	15.1	1,170
10-11/07/1998	00:06-04:35	≈1 arcsec	ISIS blue arm	R1200B	5.1	1,792
		but worse				
		during last				
		hour				
			ISIS red arm	R600R	15.1	780

**Table 2.1** Overview of our high-speed spectroscopic observations of DQ Her, performed with the William Herschel Telescope

### 2.2 Doppler Maps

We first study the dependence of the spectral lines on the orbital phase of the binary. The orbital phases of the spectra were calculated using the quadratic ephemeris of Wood et al. (2005). The continuum subtracted spectra were phasebinned and rebinned to a constant velocity scale of  $50\,\mathrm{km\,s^{-1}}$  per pixel for the blue arm spectra and  $18\,\mathrm{km\,s^{-1}}$  for the red arm spectra. The top panels of Figs. 2.1, 2.2, 2.3, 2.4, 2.5 and 2.6 show the resulting orbital trails for selected emission lines. Blank horizontal lines indicate uncovered orbital phases. To shed light on the binary components that contribute to the phase-dependent line profiles, Doppler tomograms have been produced, which are shown on the bottom panels of the same figures.

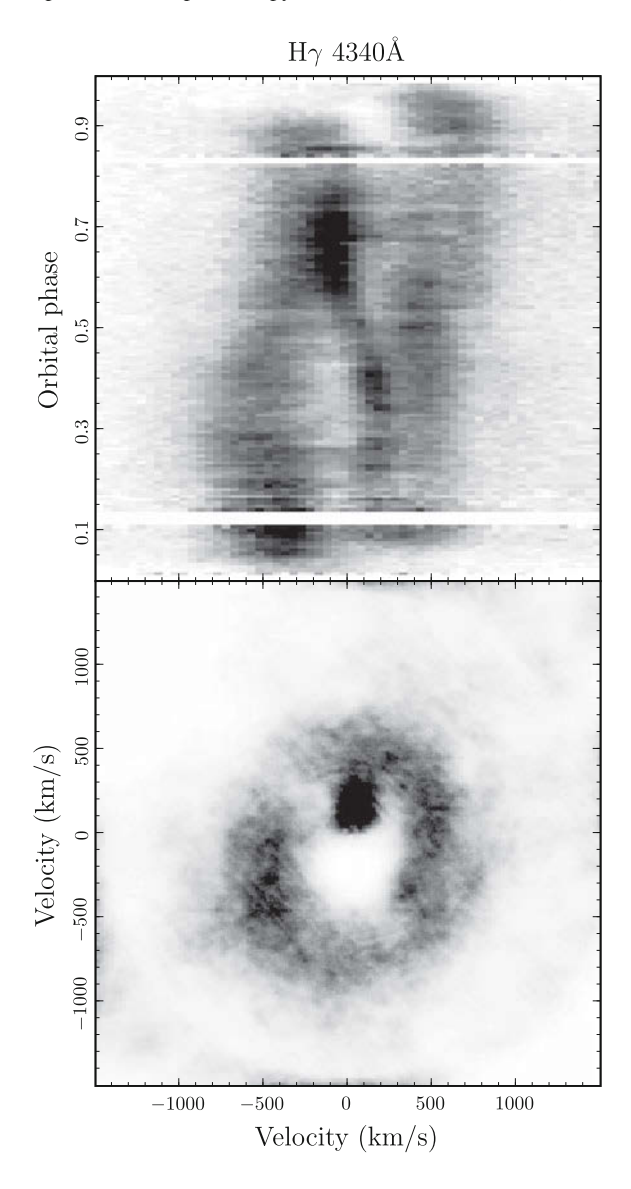
Line profiles that are observed at different orbital phases are effectively projections of a rotating velocity image of the binary. Doppler tomography allows the construction of the velocity image from observed spectra. The images shown here have been created using the maximum entropy method (MEM) as implemented in TRM's DOPPLER package<sup>0</sup>, which is an iterative procedure to build up an image that reproduces the observed profiles best while striving towards a map of least structure. A detailed description of Doppler tomography using MEM is presented in Marsh and Horne (1988).

Spectra taken between orbital phases -0.1 and 0.1 have not been used to avoid fitting the effect of the eclipse. A systemic velocity of  $\gamma = -60 \, \mathrm{km \, s^{-1}}$  was adopted (Hutchings et al. 1979).

### 2.2.1 Balmer Lines

The tomograms of H $\gamma$  and H $\beta$  (Figs. 2.1 and 2.2) look like the velocity images of a typical cataclysmic variable. The broad line wings that are emitted by the accretion

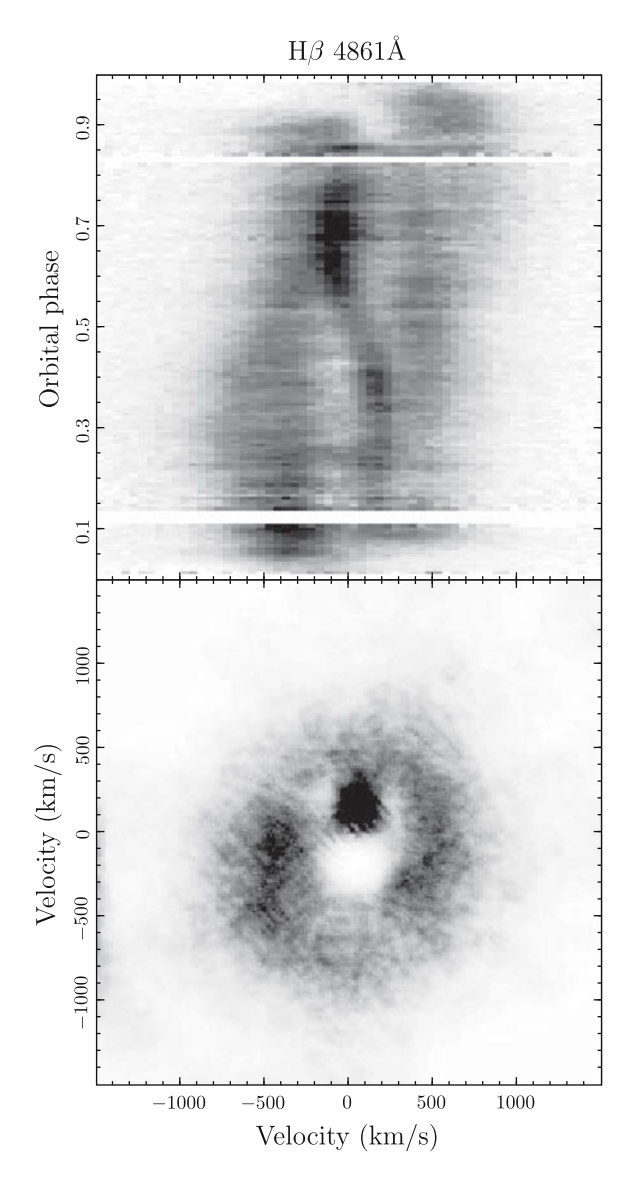
Fig. 2.1 The observed H $\gamma$  flux of DQ Her in function of orbital phase (top panel) and the corresponding Doppler map (bottom panel). The continuum level is set to white. The accretion disc and the secondary star show up in the Doppler map, as expected for a cataclysmic variable



disc around the white dwarf map onto the diffuse ring in the Doppler maps. The ring is shown inside out because the disc components with the highest velocities are the ones closest to the white dwarf in positional space. The S-wave on the trail is emission from the secondary star and maps onto a bright dot around  $K_2$ , which Horne et al. (1993) determined to be 227 km s<sup>-1</sup>. On the trails of the spectra, the rotational disturbance of the line through eclipse is clearly visible (Young and Schneider 1980).

2.2 Doppler Maps 17

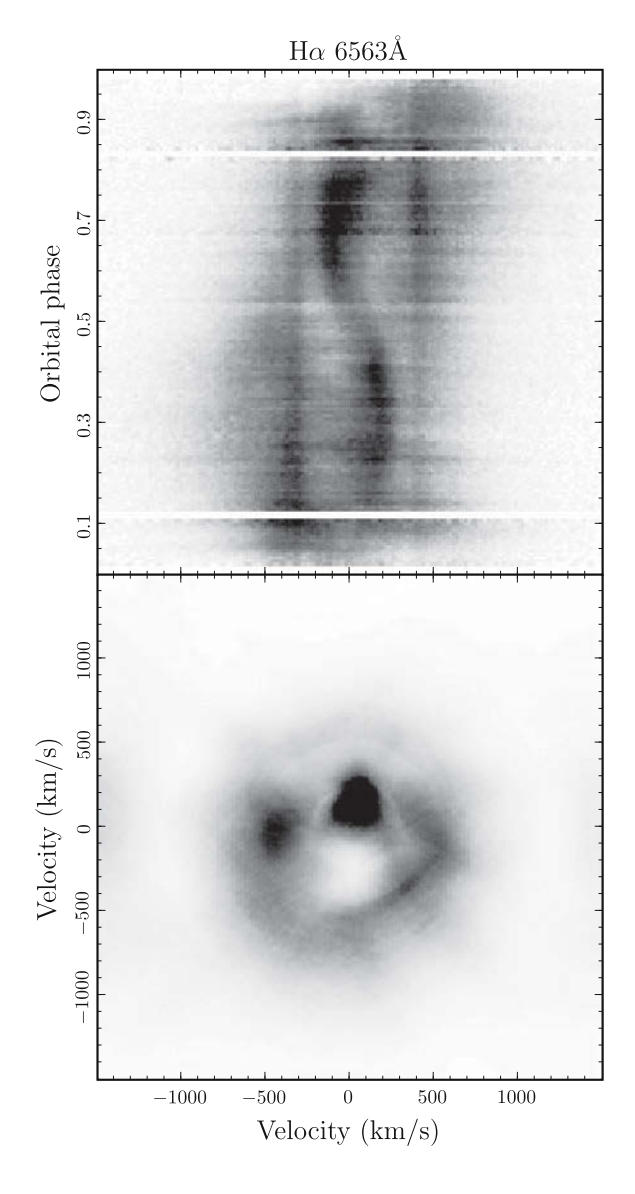
Fig. 2.2 The observed H $\beta$  flux of DQ Her in function of orbital phase (top panel) and the corresponding Doppler map (bottom panel). The Doppler map shows the same components as the H $\gamma$  map in Fig. 2.1



The blue-shifted part of the accretion disc emission gets eclipsed first and reappears earlier than the red-shifted part.

The H $\alpha$  line (Fig. 2.3) is found to have stationary components at  $-388 \pm 2$  and  $+337 \pm 2$  km s<sup>-1</sup>. These components were already reported by Bianchini et al. (2004). Contrary to their findings, however, we do see emission from the nova shell in the 'sky regions' of our 2D spectra and therefore believe that the stationary emission components are emitted by this shell. The shell is the result of the nova which took

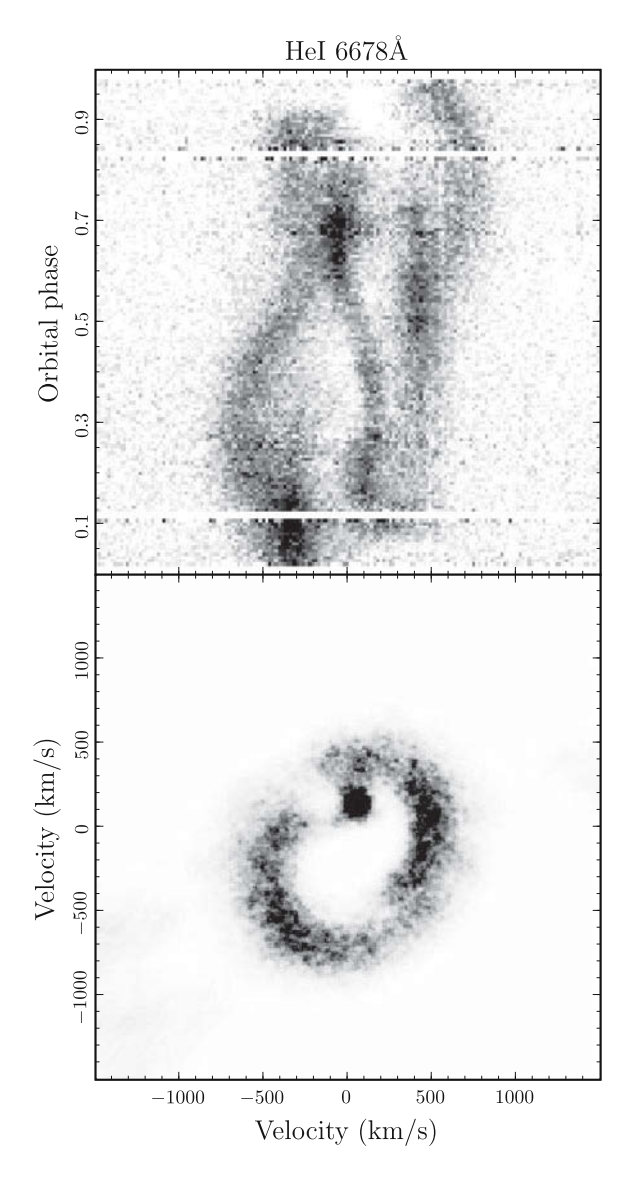
**Fig. 2.3** The observed  $H\alpha$ flux of DQ Her in function of orbital phase (top panel) and the corresponding Doppler map (bottom panel). Emission from the accretion disc and the secondary is present as in the other Balmer lines, but additional stationary components are observed at  $-388 \pm 2$  and  $+337 \pm 2 \,\mathrm{km}\,\mathrm{s}^{-1}$  which are probably emitted by DO Her's nova shell. A region of  $160 \, \mathrm{km} \, \mathrm{s}^{-1}$  around these components was masked when creating the Doppler image



place in 1934. Vaytet et al. (2007) estimated the expansion velocity of the nova at 370 km s<sup>-1</sup>, which looks to be consistent with our findings. Doppler tomography assumes that all light is emitted by material that corotates with the binary. When creating the Doppler map for H $\alpha$ , a region of  $160 \, \text{km s}^{-1}$  around the stationary components was masked to give the best possible representation of the structure of the binary system, but this masking also introduces uncertainties in a ring with a width of  $\approx 160 \, \text{km s}^{-1}$  and a radius of  $\approx 350 \, \text{km s}^{-1}$  from the center of the map.

2.2 Doppler Maps 19

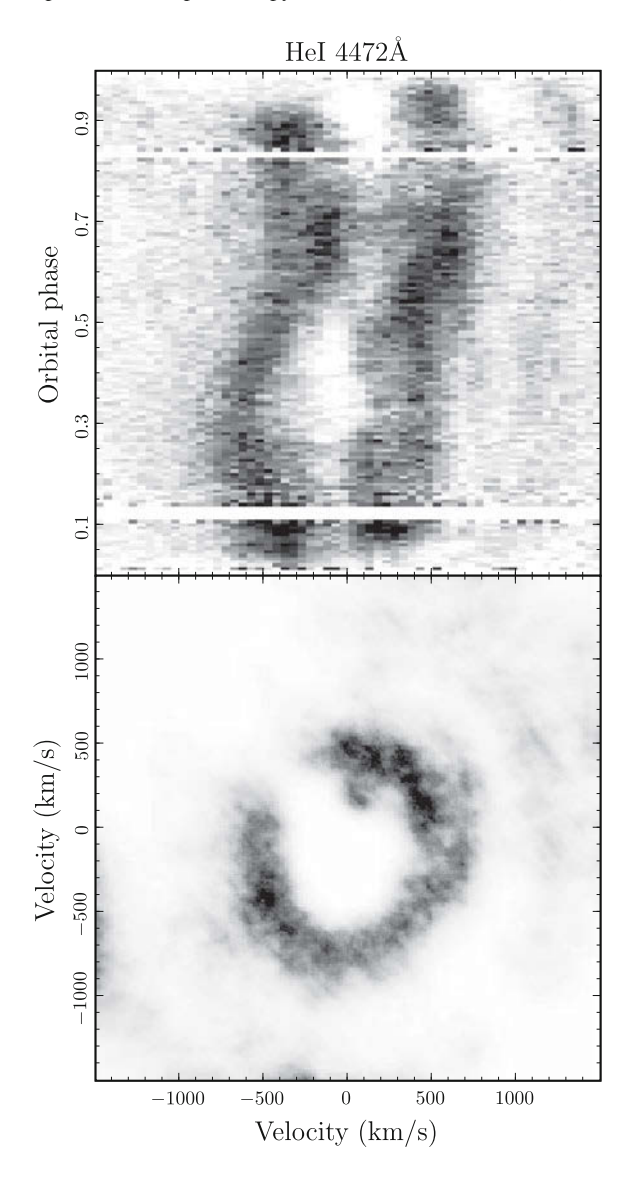
Fig. 2.4 The observed He I λ6678 flux of DQ Her in function of orbital phase (top panel) and the corresponding Doppler map (bottom panel). Spiral arms are detected in the accretion disc, which are caused by tidal effects from the secondary on the outer part of the disc



### 2.2.2 Spiral Structure on the He I $\lambda 4472$ and $\lambda 6678$ Maps

The He I maps (Figs. 2.4 and 2.5) reveal spiral structure in the disc, which is also present on the H $\gamma$  tomogram. The spiral pattern is comparable to that found in a number of dwarf novae during outburst and in novalike CVs. Spirals were first discovered in the dwarf nova IP Peg in outburst by Steeghs et al. (1997). In that paper it was shown that spirals in velocity space map onto spirals in positional

Fig. 2.5 The observed He I  $\lambda 4472$  flux of DQ Her in function of orbital phase (*top panel*) and the corresponding Doppler map (*bottom panel*). As in the He I  $\lambda 6678$  map (Fig. 2.4), spiral arms are seen in the accretion *disc* 

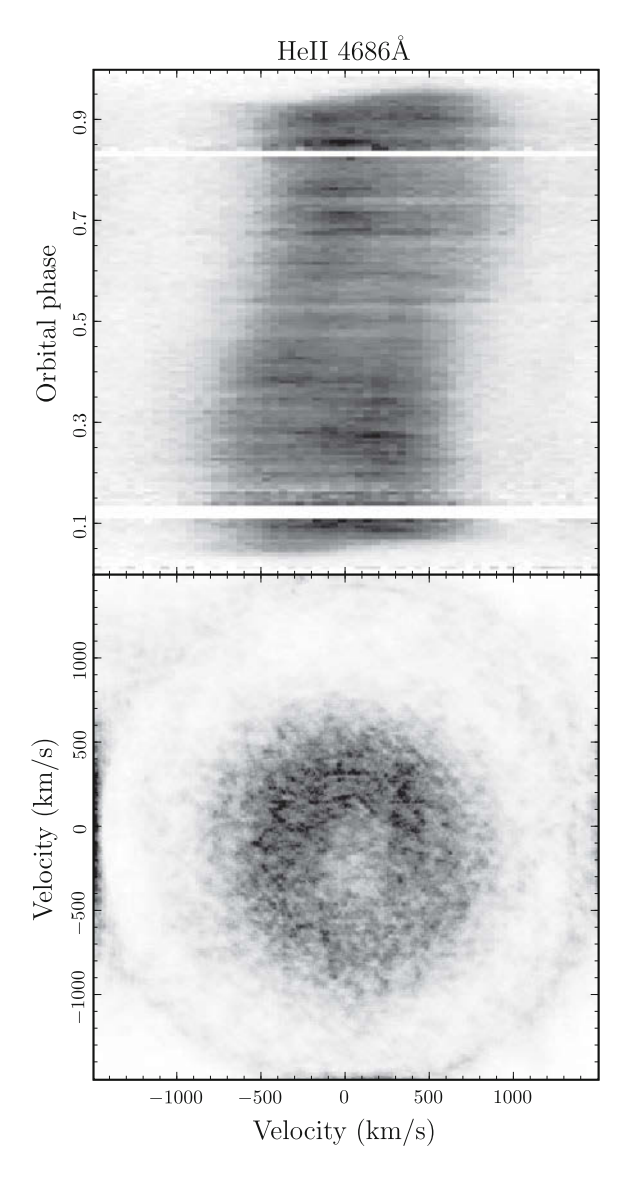


coordinates as well. A review of observations of spirals in CV discs can be found in Steeghs (2001). Spirals in accretion discs of CVs are believed to arise from tidal forces from the secondary on the outer regions of the disc. Because the material in the disc gradually spirals inwards to orbits with a higher Keplerian velocity, a double spiral arm is created.

Systems in which spirals are seen, have a high mass transfer rate and thus a large accretion disc, filling most of the Roche lobe of the white dwarf. This is necessary for

2.2 Doppler Maps 21

Fig. 2.6 The observed He II λ4686 flux of DQ Her in function of orbital phase (top panel) and the corresponding Doppler tomography image (bottom panel). The very diffuse disc probably indicates that a substantial part of the line emitting material has a strong non-Keplerian velocity component



the secondary to have a large enough tidal effect (Savonije et al. 1994). The disc of DQ Her extends up to at least 87 of the white dwarf's Roche lobe (Harrop-Allin and Warner 1996, determined from the eclipse duration). In dwarf novae, the spirals are only observed during outburst when the mass transfer rate is temporarily increased, i.e. for only a few days in an outburst cycle of the order of months. This makes them particularly difficult to observe because the outburst moments are difficult to predict.

This is the first detection of spirals in the accretion disc of a well-established intermediate polar. The fact that the WD is magnetic does not seem to preclude spirals. Given that their formation is driven by tides in the outer disc and does not directly depend on the magnetically-controlled inner disc, this does not come as a surprise. In WZ Sge, which is possibly an IP, spirals have been detected as well (Baba et al. 2002) but only during outburst.

Several systems have been proposed to explain the apparent presence of spiral structure in accretion discs (see e.g., Steeghs and Stehle 1999; Smak 2001; Ogilvie 2002). Our data do not allow to descriminate between the different explanations, but DQ Her is a good candidate system for further research on the spirals in accretion discs. Since the mass transfer in DQ Her is believed to be in an equilibrium state, the spiral structure is very likely to be permanently visible, which is a huge advantage over the known dwarf novae which only show spirals during outbursts.

### 2.2.3 He II \(\lambda\)4686

The map of He II  $\lambda$ 4686 (Fig. 2.6) shows a filled ring. As Martell et al. (1995) already pointed out, this reflects the absence of a double peaked line profile. The He II  $\lambda$ 4686 line is formed after electron capture by He III. The ionisation energy of He I is 24.6 eV and further ionisation of He II requires 54.4 eV. High temperatures are needed to make this possible, which are only found in the inner regions of the disc. In this region, the material has high Keplerian velocities. The presence of a lot of emission at lower velocities shows that the line has a much higher non-Keplerian component than the other lines. We therefore consider it very likely that a substantial part of the line is produced in a region that is influenced by the magnetic field, because material that gets trapped by magnetic field lines gets a larger than usual velocity component towards the white dwarf as well as a non-negligible component in the direction perpendicular to the disc. We can also confirm the observation by Martell et al. (1995) of high emission regions on the upper half of the map. The higher emission in the disc part  $V_X < 0$ ,  $V_Y > 0$  can be associated with the accretion stream, but the high emission at  $V_X > 0$  is not easily explained.

In an attempt to find the variations in the line profiles due to reprocessed X-rays of the white dwarf in the disc or on the secondary star, Doppler maps were also created for different phases in the spin period and the beat period, but no significant variations were found.

### 2.2.4 Discussion

Angular momentum transport in accretion discs is still actively studied. The famous " $\alpha$ -description" by Shakura and Sunyaev (1973) explains the momentum transport by a viscosity effect. The effective viscosity is believed to be driven by MHD instabilities

2.2 Doppler Maps 23

that make shear flows turbulent (for an extensive review see Balbus 2003). Spiral arms are of notable astrophysical interest because spiral shocks are believed to be an alternative (or complementary) means to transfer angular momentum. A review of the theoretical efforts on spiral shocks is presented in Boffin (2001). The establishment of spiral waves in an accretion disc of an IP also re-enforces the findings by Murray et al. (1999) that tidally induced spirals can propagate sufficiently far into the disc of an IP such that they can modulate the accretion rate onto the white dwarf. This could explain the sidebands of the spin frequency that are often found in X-ray and optical light curves of IPs. These sidebands were thought to be a sign of mass accretion via a direct mass stream from the first Lagrange point to the white dwarf rather than via an accretion disc and have been used to discriminate between systems that have only disc accretion, only stream accretion or a mixture of both (see e.g., Norton et al. (1996) for a model of the X-ray power spectrum and Hellier (2007) for a review on accretion in IPs). If spirals can cause the sidebands as well, the conclusions drawn on this basis may require reassessment.

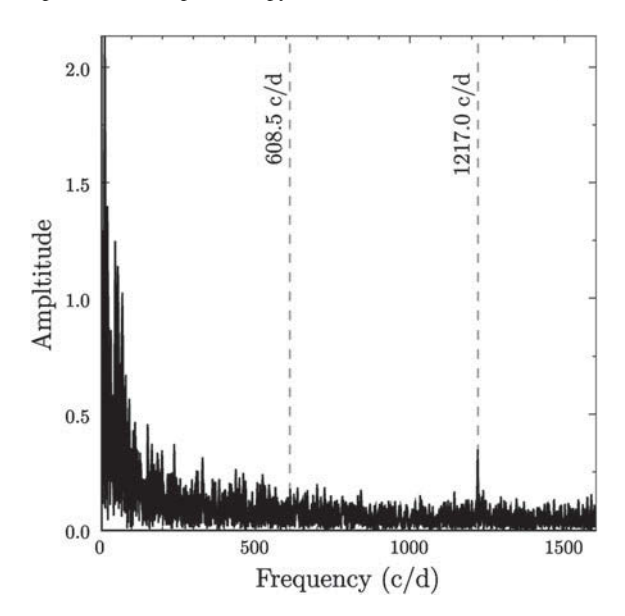
### 2.3 Spin Phase Dependence of the Spectral Lines

Our high-speed spectroscopic dataset also allowed us to study the variations in the spectral line shapes on the spin period of the binary's white dwarf. X-rays that are emitted from the white dwarfs' magnetic poles in intermediate polars can make the spin period of the white dwarf visible in light curves and spectra of an IP. As the white dwarf spins, the X-ray beams sweep around, creating a light house effect. If such a beam (or both beams) illuminate the accretion disc, reprocessing of the X-rays can lead to enhanced continuum and line emission. As mentioned in Sect. 2.1, in the case of DQ Her, depending on the study a 71 s or 142 s periodicity is found. This periodicity is too stable to be an asteroseismological effect and is therefore very likely to be associated with the spin frequency of the white dwarf. A less favoured explanation is that the 71 s periodicity is in fact the beat period ( $\omega_{beat} = \omega_{spin} - \omega_{orb}$ ), which would be the case if the vast majority of reprocessing is done in the bright spot where the accretion stream hits the disc (e.g., Saito and Baptista 2009) or on the surface of the secondary star, since both orbit at the orbital frequency.

### 2.3.1 Spin Periodicity in the Red-Shifted Wing of He II λ4686

Since our spectra were taken without a comparison star in the slit, we could not correct for variations in the observed intensity that are due to atmospheric conditions and slit losses. We thus worked with continuum-subtracted spectra and limited our study of the oscillations to the flux in the emission lines. These can fluctuate more than the continuum level if the high energetic UV and X-ray photons of the WD beams trigger extra line transitions. A Lomb-Scargle periodogram (Lomb 1976; Scargle

**Fig. 2.7** Periodogram of the flux in the He II  $\lambda$ 4686 *line*. The 71 s periodicity (1217.0 d<sup>-1</sup>) is retrieved, but no 142 s periodicity (608.5 d<sup>-1</sup>) is found



1982) for the He II  $\lambda$ 4686 line flux is shown in Fig. 2.7. A peak is found at 1,217 cycles per day (d<sup>-1</sup>), which is equivalent to a period of 71 s. No pulsation amplitude is found at the 142 s period (608.5 d<sup>-1</sup>). This result is in line with the outcome of most photometric studies which find the white dwarf spin period of 71 s, as described in Sect. 2.1. Periodograms of the fluxes in the Balmer and He I lines that were used in Sects. 2.2.1 and 2.2.2 show no frequencies above noise level (not shown). The line transition in which these photons are emitted is thus not strongly influenced by the beam photons or the emitting region is not easily reached by the beam.

To visualise the effect of the X-ray reprocessing on the spectral line flux, we followed the same approach as Martell et al. (1995). We folded the data on the 71 s and 142 s periods and subtracted a mean spectrum. This way, only the deviations from the mean value are left. Only spectra taken at orbital phases from 0.1 up to 0.9 are used, i.e. spectra taken during eclipse are omitted.

In Fig. 2.8, a trail of He II  $\lambda$ 4686 is plotted after folding on a 71 s period. The cycle is repeated to ease comparison with the 142 s trails. Light pixels indicate a line flux that is lower than the average over the spin cycle on that particular wavelength, dark indicates a higher than average flux. The black sinusoidal curve shows the path of the enhanced emission that would be seen when the reprocessing region is a small part of the disc that follows a circular orbit, as also shown on the spin trails of Martell et al. (1995). Figure 2.9 shows the result of folding on a 142 s period. For a 71 s spin period, one reprocessing region is needed. For a 142 s spin period, one needs two reprocessing regions that are half a spin phase apart to produce the observed periodicity. Therefore, two sine curves with a phase difference of 180° have been plotted.

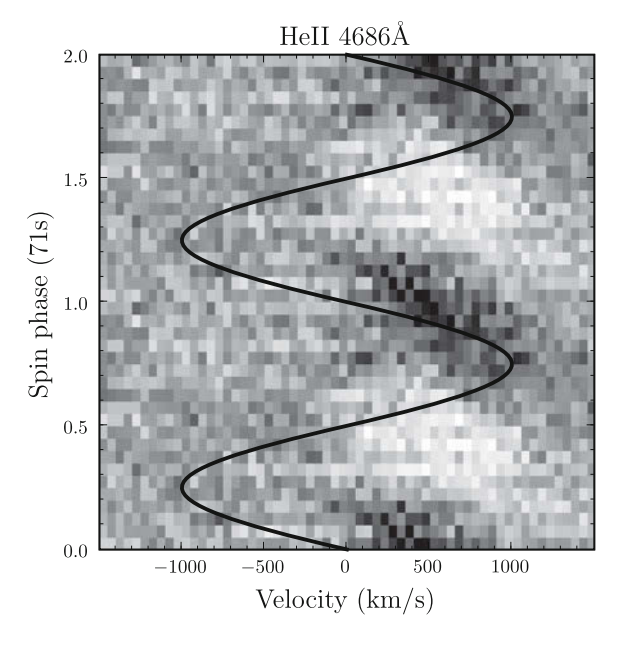
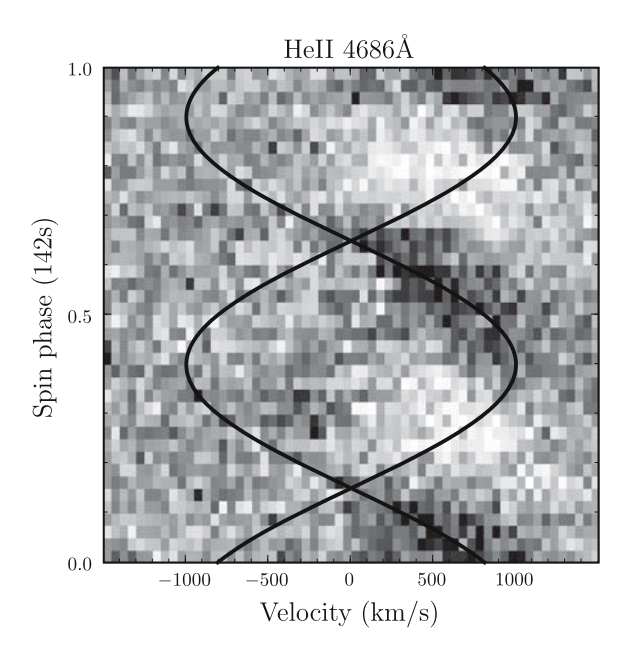


Fig. 2.8 Trail of continuum and mean subtracted He II  $\lambda$ 4686 *line* profiles, folded on a 71 s period. The spin phase is shown twice to ease comparison with the next figure. In the *blue*-shifted part of the *line*, no modulation is seen on the 71 s period. In the *red*-shifted part, however, enhanced emission is seen once per phase (*darker region*). Note that the *white region* does not denote a lower emission than the *grey region* in the *blue-shifted part*, but a lower emission than the average on those particular wavelengths. The *black sinusoidal curve* shows where enhanced emission from reprocessing of the light of one white dwarf X-ray beam in a small part of the disc would be seen

We confirm, but with greater significance, the observation of Martell et al. (1995) that a pulsation is visible in He II  $\lambda$ 4686 when the beam illuminates the red-shifted part of the back side of the disc, but invisible when the beam points to the front side or the blue-shifted part of the back side. The absence of fluctuations in the light coming from the front side of the disc is not surprising: the inclination is close to 90° and since a disc is not flat but rather concave, our view of the front part might well be blocked by the thick edge (the rim) of the disc. The fact that no fluctuations are seen in the blue-shifted part of the back side of the disc is more puzzling. Martell et al. (1995) propose that the pulsation comes from the threading region, i.e. the region at the inner edge of the disc where the material gets trapped by the magnetic field of the white dwarf. If this region is optically thick, a velocity gradient in the direction of our line of sight will result in enhanced emission (Horne 1995).

Another possible explanation is that the X-rays are reprocessed by (optically thick) accretion curtains. Due to the curvature of such curtains, one can imagine that the X-ray beam might only illuminate the curtain side closest to the white dwarf (the 'bottom' side), and not the 'top' side. If the curtain is optically thick, then it might be the case that we see the bottom side of the curtain when it is receding

Fig. 2.9 Figure similar to Fig. 2.8 but assuming a spin period of 142 s. The black curves show the emission that can be expected from inner disc reprocessing of two white dwarf X-ray beams. Two similar regions with enhanced emission can be seen, which suggests that the true spin frequency is rather 71 s. However, the slope of the sinusoidal curves fits the slope of the enhanced emission better than in the case of 71s



from us and the non-illuminated top side when it is approaching us. Such a scenario would produce variations in the red-shifted part of the line, but no fluctuations in the blue-shifted part.

A scenario in which the accretion from the disc onto the white dwarf's surface switches on and off during the spin cycle was also considered. This can be the case when the orientation of the WD's magnetic axis is offset from the rotation axis such that the magnetic field disconnects from and reconnects with the material in the disc. One would expect that if at a certain orbital phase the magnetic field is connected when the magnetic pole is red-shifted and disconnected when the pole is blue-shifted, the opposite would be true half an orbit later. Therefore, as much variation should be observed in the blue-shifted parts of the line as in the red-shifted, which is not the case. Furthermore, in Sect. 2.3.3 we will show that the periodicity in the red-shifted wing of the line is observed at all orbital phases, which also rules out this explanation.

Spin trails have been published earlier for IPs with slower spinning white dwarfs, e.g., for EX Hya in Hellier et al. (1987), for FO Aqr in Hellier et al. (1990), for AO Psc in Hellier et al. (1991), for BG CMi and PQ Gem in Hellier (1997), and for V2400 Oph and V1025 Cen in Hellier (1999). All of these reveal variations in both the blue- and redshifted parts of the lines. One has to keep in mind, however, that the accretion region in DQ Her might be fundamentally different since its WD is one of the fastest spinning of the known IPs (the spin periods in the other IPs mentioned here range from 805 s for AO Psc to 4,022 s for Ex Hya). Though technically challenging, high speed spectroscopy of other fast spinning IPs is necessary to check whether DQ Her's spin effects are common among this group of IPs.

#### 2.3.2 71 s or 142 s Periodicity in He II $\lambda 4686$ ?

The spin trail of He II  $\lambda$ 4686 also potentially offers a means to conclude the discussion on whether the spin period is 71 s or rather 142 s with two spots contributing to the pulsation. The slope of the simplistic disc reprocessing model clearly fits the 142 s trail (Fig. 2.9) better than the 71 s trail (Fig. 2.8). The sinusoidal curves would be fairly correct if a small part of the disc at semi-Keplerian orbits, e.g., the inner part of the disc, reprocesses the X-rays of the WD poles. If that is the case, a 142 s spin period is to be preferred. If the extra emission, however, comes from accretion curtains (as was suggested already for some of the IPs with slower spinning WDs, see e.g., Hellier et al. 1990), a sinusoidal radial velocity trace is too simple and a more detailed model would be required to draw a conclusion. As discussed in Sect. 2.2.3, the Doppler map of this He II line (Fig. 2.6) shows a large non-circular component, which can also be explained by the reasoning that the He II emission would primarily come from an accretion curtain. The fact that we do not see any significant difference between the first half and second half of a 142 s cycle confirms earlier suggestions that if the spin period is really 142 s, the two poles would have to be almost identical.

#### 2.3.3 Can 71s Be the Beat Frequency?

Very recently, Saito and Baptista (2009) used the dataset formerly used by Martell et al. (1995) for eclipse mapping. Comparing eclipse maps of different spin phases, they claimed to have found compelling evidence for the existence of a rotating component at the inner radius of the disc, which they associated with an accretion curtain, and pulsating emission from the bright spot in the outer part of the disc. They conclude that mostly the bright spot and to a lesser extent accretion curtains contribute to the 71 s fluctuations, and that the observed frequency should be the beat frequency instead of the spin frequency because of the larger contribution by the bright spot.

Given the much higher signal-to-noise ratio of our data compared to the spectra used by Martell et al. (1995), we were able to check the variability in the pulsation of the He II  $\lambda$ 4686 line over different orbital phases. Figure 2.10 displays the spin trails (folded on the 71 s period) for five orbital phase intervals. The amplitude of the pulsation in the red-shifted wing of the line seems a little lower at the later orbital phases but the variability is still obvious. This indicates that most of the pulsation originates from the disc, and not from the bright spot or the secondary star. Note that some variability can be seen in the blue-shifted wing of the line at late orbital phases as well.

The 71 s pulsation in the red-shifted wing at orbital phases where the possible beat frequency contributors (the bright spot and the secondary) are in the blue-shifted part of the line rules out the possibility that the spin period would be 70.8 s, with the dominant 71 s pulse being the beat period. The time baseline of the observations is long enough to resolve the difference between a 70.8 s and a 71.0 s period. On the

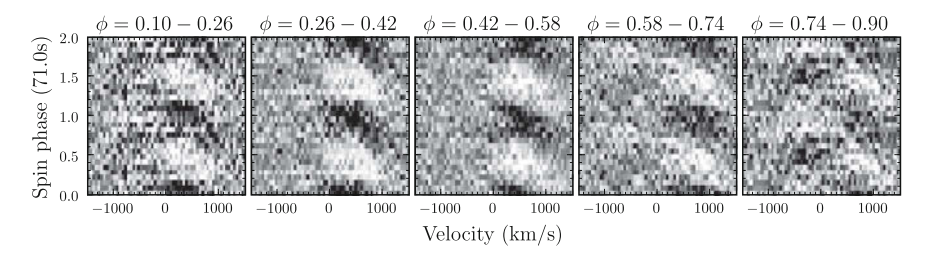


**Fig. 2.10** Spin trails of He II  $\lambda$ 4686 similar to Fig. 2.8, assuming a 71 s spin period, but produced using spectra taken during different orbital phase ( $\phi$ ) intervals. The variation in the *red*-shifted wing of the *line* is visible on all orbital phases, which indicates that the pulsation cannot originate from reprocessing on the *bright spot* or the secondary *star*. In that case, the variations would not be visible at late orbital phases, when the *bright spot* and *secondary star* are at *blue*-shifted velocities. A weak variability component is detected in the *blue*-shifted wing of the *line* at late orbital phases

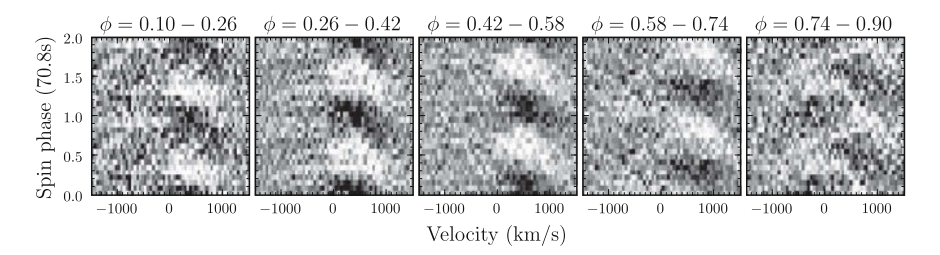


Fig. 2.11 Spin trails of He II  $\lambda$ 4686 similar for different orbital phase intervals like Fig. 2.10, but assuming a 70.8 s spin period. This would be the case if 71 s is the beat period. The dataset clearly allows to distinguish a 70.8 s from a 71 s periodicity, since it can clearly be seen that the pulsation occurs at later spin phases on the plots of later orbital phases. No 70.8 s periodicity is found, because it is dominated by the 71 s frequency or because it is absent

71s trails, the pulsation profile in the red-shifted part of the line stays at the same phase, while for 70.8s it shifts over 1 spin phase in 1 orbital cycle. This is illustrated on Fig. 2.11 which shows the trails folded on the 70.8s period for the same orbital phase chunks as Fig. 2.10. The shift of the pulsation in the red wing is clearly visible, which also strengthens our believe that if a 70.8s periodicity is present at all, it is certainly not dominant over the 71s period.

The detection of the 71 s pulsation in the red-shifted part of the line at all orbital phases and the fact that eclipse mapping is not as well constrained as Doppler mapping and the spin trails because it only uses data taken during eclipse, during which part of the disc remains hidden from view, we believe that further evidence is necessary to confirm that the He II-pulsation arises from the curtains. The bright spot might contribute as well, but probably not as much as derived by Saito and Baptista (2009) from the eclipse maps because we can rule out the possibility that 70.8 s is the true spin period, which would be necessary if the bright spot is the dominant source of the pulsations.

#### 2.3.4 Spin Periodicity in the Balmer and He I Lines

Signs of a variation on the spin period are also visible in the trails of the Balmer lines, which are shown in Fig. 2.12 for H $\gamma$  and H $\beta$  folded on the 71 s period and in Fig. 2.13 for the same lines folded on the 142 s period. The amplitude is only marginally above noise level, but it seems that there is a fluctuation visible in the blue parts of the Balmer lines as well, which is similar to the variations in He II  $\lambda$ 4686 at late orbital phases. The red wings seem to show a pattern that is different from the one seen in He II  $\lambda$ 4686. The pulsation is not well fitted by the simple 71 s pulse model, but the same holds for the 142 s model. This observation also points in the direction of a more complicated geometry of the reprocessing region. The spin behaviour of H $\alpha$  could not be checked because this line was observed with the red arm of ISIS using exposure times of 15.1 s, contrary to the other lines which were observed with the blue arm at a 5.1 s cadence.

The pulsations in the He I lines are too weak to be detected on spintrails.

Fig. 2.12 Spin trail similar to Fig. 2.12 for H $\gamma$  and H $\beta$ , assuming a 71 s spin period. Variations are seen in both the *blue*- and *red*-shifted parts of the *line*. The simple *disc* reprocessing model does not fit the emission features well

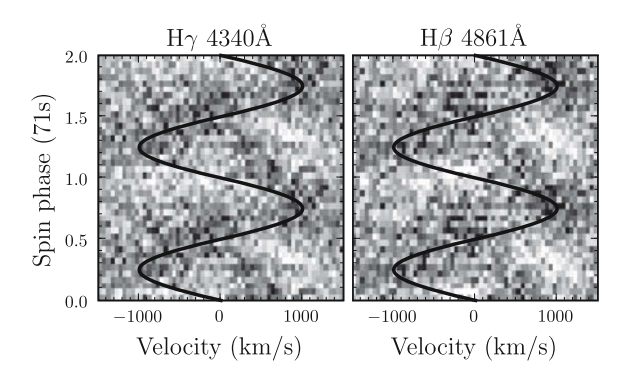
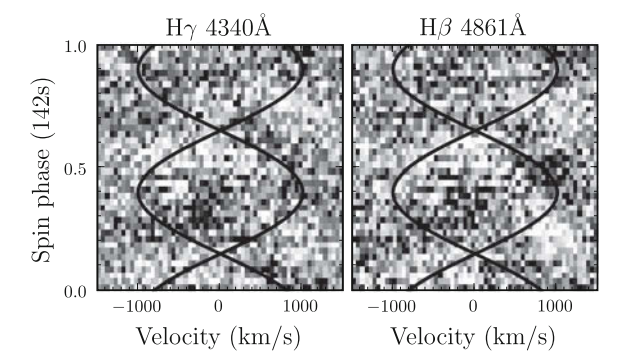


**Fig. 2.13** Spin trail similar to Fig. 2.12 but assuming a 142 s spin period. The *disc* reprocessing model fits the slope of the *red*-shifted emission features well, but fails completely in explaining the variations in the *blue*-shifted wing of the *line* 



#### 2.4 Conclusions

We studied high-speed spectroscopy of the prototype intermediate polar DQ Her. We report the first detection of spiral arms in the accretion disc of an intermediate polar. Spiral arms are seen in Doppler maps of H $\gamma$ , He I  $\lambda$ 4472 and He I  $\lambda$ 6678. Spirals arise from tidal effects from the secondary star on the accretion disc. They were found before in dwarf novae in outburst and in nova-like variables. Since spiral shocks are believed to be an additional mechanism for the transport of angular momentum in a disc besides viscosity effects, they can form a crucial clue in the understanding of disc related accretion processes and other astrophysical phenomena like planet and star formation. If spiral arms can propagate far enough into the disc, as indicated by the simulations of Murray et al. (1999), they can modulate the accretion rate onto the white dwarf. Inner disc asymmetries such as those produced by spiral arms can therefore possibly explain the sidebands of the spin frequency that are often observed in X-ray and optical light curves of IPs. Until now, it was believed that these sidebands indicate that (part of) the accretion proceeds via a direct stream from the first Lagrangian point to the white dwarf rather than through the disc. If spiral arms in accretion discs can explain the sidebands equally well, accretion streams might be less frequent than currently thought.

We built upon the study of the pulsation pattern in emission lines from the accretion disc as presented earlier by Martell et al. (1995). We confirm with greater significance that reprocessed light from the WD beam is mainly visible in He II  $\lambda 4686$  when the beam points to the red-shifted back side of the disc. The slope of the pulsation on a spin trail does not match with what would be expected from a simple model for a spin period of 71 s in which a small region of the disc reprocesses the X-rays from the WD beam. The same model for two reprocessing spots and a 142s spin period results in a better fit. However, the Doppler map of He II  $\lambda 4686$  suggests that the line emitting region has a substantial non-Keplerian component. Reprocessing in accretion curtains might be a solution to fit both the slope of the pattern and the absence of observed pulsations in the blue-shifted part of the line, but further modelling is required to check this suggestion. The lack of a good model thus currently prevents us from settling the discussion as to whether 71 s or 142 s is the true white dwarf spin period. The spin trails of the He I and Balmer lines show weak pulsation components as well, with puzzling slopes. We are not aware of any fully developed IP model that can quantitatively explain our observations. The spin trails clearly provide much more information than can be derived from photometric studies and provide a strong test for enhanced IP accretion models in the future.

Pulsations are still observed at a 71s periodicity in the red-shifted wing of He II  $\lambda$ 4686 at orbital phases where the bright spot is in the blue-shifted part of the disc. We therefore refute the assertion by Saito and Baptista (2009) that most of the reprocessed light comes from the bright spot, and rule out the possibility that 70.8s would be the true spin period.

References 31

#### References

Baba, H., Sadakane, K., Norimoto, Y., Ayani, K., Ioroi, M., Matsumoto, K., et al. (2002). PASJ, 54, L.7

Balbus, S. A. (2003). ARA&A, 41, 555.

Bianchini, A., Mastrantonio, E., Canterna, R., Stute, J., & Cantrell, K. (2004). A&A, 426, 669.

Bloemen, S., Marsh, T. R., Steeghs, D., & Østensen, R. H. (2010). MNRAS, 407, 1903.

Boffin, H. M. J. (2001). Spiral waves in accretion discs—Theory. In H. M. J. Boffin, D. Steeghs & J. Cuypers (Eds.), *Astrotomography, indirect imaging methods in observational astronomy* (Vol. 573, p. 69). Lecture Notes in Physics. Berlin: Springer.

Butters, O. W., Katajainen, S., Norton, A. J., Lehto, H. J., & Piirola, V. (2009). A&A, 496, 891.

Chanan, G. A., Nelson, J. E., & Margon, B. (1978). ApJ, 226, 963.

Chester, T. J. (1979). ApJ, 230, 167.

Greenstein, J. L., & Kraft, R. P. (1959). ApJ, 130, 99.

Harrop-Allin, M. K., & Warner, B. (1996). MNRAS, 279, 219.

Hellier, C. (2007). Disc magnetosphere interactions in cataclysmic variable stars. In J. Bouvier & I. Appenzeller (Eds.), *IAU Symposium* (Vol. 243, p. 325).

Hellier, C., Mason, K. O., Rosen, S. R., & Cordova, F. A. (1987). MNRAS, 228, 463.

Hellier, C., Mason, K. O., & Cropper, M. (1990). MNRAS, 242, 250.

Hellier, C., Cropper, M., & Mason, K. O. (1991). MNRAS, 248, 233.

Hellier, C. (1997). MNRAS, 288, 817.

Hellier, C. (1999). *ApJ*, *519*, 324.

Horne, K., Welsh, W. F., & Wade, R. A. (1993). ApJ, 410, 357.

Horne, K. (1995). A&A, 297, 273.

Hutchings, J. B., Cowley, A. P., & Crampton, D. (1979). ApJ, 232, 500.

Kemp, J. C., Swedlund, J. B., & Wolstencroft, R. D. (1974). ApJ, 193, L15.

Kiplinger, A. L., & Nather, R. E. (1975). Nature, 255, 125.

Lomb, N. R. (1976). Ap&SS, 39, 447.

Marsh, T. R., & Horne, K. (1988). MNRAS, 235, 269.

Martell, P. J., Horne, K., Price, C. M., & Gomer, R. H. (1995). ApJ, 448, 380.

Murray, J. R., Armitage, P. J., Ferrario, L., & Wickramasinghe, D. T. (1999). Spiral waves and periodic accretion in intermediate polars. In C. Hellier & K. Mukai (Eds.), Annapolis workshop on magnetic cataclysmic variables (Vol. 157, p. 25). Astronomical Society of the Pacific Conference Series.

Nelson, M. R. (1975). ApJ, 196, L113.

Norton, A. J., Beardmore, A. P., & Taylor, P. (1996). MNRAS, 280, 937.

Ogilvie, G. I. (2002). MNRAS, 330, 937.

Patterson, J., Robinson, E. L., & Nather, R. E. (1978). ApJ, 224, 570.

Patterson, J. (1994). PASP, 106, 209.

Petterson, J. A. (1980). ApJ, 241, 247.

Saito, R. K., & Baptista, R. (2009). ApJ, 693, L16.

Savonije, G. J., Papaloizou, J. C. B., & Lin, D. N. C. (1994). MNRAS, 268, 13.

Scargle, J. D. (1982). ApJ, 263, 835.

Schoembs, R., & Rebhan, H. (1989). A&A, 224, 42.

Shakura, N. I., & Sunyaev, R. A. (1973). A&A, 24, 337.

Smak, J. I. (2001). Acta Astronomica, 51, 295.

Steeghs, D. (2001). Spiral waves in accretion discs—Observations. In H. M. J. Boffin, D. Steeghs, & J. Cuypers (Eds.), *Astrotomography, indirect imaging methods in observational astronomy* (Vol. 573, p. 45). Lecture Notes in Physics. Berlin: Springer.

Steeghs, D., Harlaftis, E. T., & Horne, K. (1997). MNRAS, 290, L28.

Steeghs, D., & Stehle, R. (1999). MNRAS, 307, 99.

Swedlund, J. B., Kemp, J. C., & Wolstencroft, R. D. (1974). ApJ, 193, L11.

Vaytet, N. M. H., O'Brien, T. J., & Rushton, A. P. (2007). MNRAS, 380, 175.

Walker, M. F. (1954). PASP, 66, 230.

Walker, M. F. (1956). ApJ, 123, 68.

Warner, B., Peters, W. L., Hubbard, W. B., & Nather, R. E. (1972). MNRAS, 159, 321.

Wood, M. A., Robertson, J. R., Simpson, J. C., Kawaler, S. D., O'Brien, M. S., & Nather, R. E. (2005). *ApJ*, 634, 570.

Young, P., & Schneider, D. P. (1980). ApJ, 238, 955.

Zhang, E., Robinson, E. L., Stiening, R. F., & Horne, K. (1995). ApJ, 454, 447.

# Chapter 3 Remarkable Spectral Variability on the Spin Period of the Accreting White Dwarf in V455 And

**Abstract** We present spin-resolved spectroscopy of the accreting white dwarf binary V455 And. With a suggested spin period of only 67 s, it has one of the fastest spinning white dwarfs known. To study the spectral variability on the spin period of the white dwarf, we observed V455 And with 2s integration times, which is significantly shorter than the spin rate of the white dwarf. To achieve this cadence, we used the blue arm of the ISIS spectrograph at the 4.2-m William Herschel telescope, equipped with an electron multiplying CCD (EMCCD). Strong coherent signals were detected in our time series, which lead to a robust determination of the spin period of the white dwarf ( $P_{\rm spin} = 67.619 \pm 0.002 \, \rm s$ ). Folding the spectra on the white dwarf spin period uncovered very complex emission line variations in  $H\gamma$ , He I λ4472 and He II λ4686. We attribute the observed spin phase dependence of the emission line shape to the presence of magnetically controlled accretion onto the white dwarf via accretion curtains, consistent with an intermediate polar type system. We are, however, not aware of any specific model that can quantitatively explain the complex velocity variations we detect in our observations. The orbital variations in the spectral lines indicate that the accretion disc of V455 And is rather structureless, contrary to the disc of the prototype of the intermediate polars, DQ Her. This work demonstrates the potential of electron multiplying CCDs to observe faint targets at high cadence, as readout noise would make such a study impossible with conventional CCDs.

# 3.1 The Cataclysmic Variable V455 And

V455 And, also known as HS 2331+3905, is a grazingly eclipsing short period cataclysmic variable ( $P_{\rm orb}=81.08\,{\rm mins}$ ) identified from the Hamburg Quasar Survey whose variability is very complex (Araujo-Betancor et al. 2005; Pyrzas 2011). It contains a rapidly spinning white dwarf (WD) accreting from a low mass

*This chapter is based on* S. Bloemen, D. Steeghs, K. De Smedt, J. Vos, B. T. Gänsicke, T. R. Marsh and P. Rodriguez-Gil, Monthly Notices of the Royal Astronomical Society, 2013, vol. 429, 3433–3438.

companion star. Araujo-Betancor et al. (2005) found two closely spaced signals at 67.2 and 67.6 s, and labelled the strongest of the two, at 67.2 s, as the WD spin period. By studying the stability of both signals in a longer photometric dataset spanning 25 d, (Gänsicke 2007) concluded that the signal at 67.6 s must be related to the true spin period. The shorter period signal is more likely to be a beat between the spin period and the  $\sim$ 3.5 h periodicity detected in spectroscopy at some epochs (Araujo-Betancor et al. 2005; Tovmassian et al. 2007). V455 And also shows variability which could be interpreted as WD pulsations. The system exhibited its first known super-outburst in 2007 (Matsui et al. 2009). The temperature of the WD is  $10,500 \pm 500 \,\mathrm{K}$  in quiescence (Araujo-Betancor et al. 2005). Dwarf nova outbursts heat up the WD, which make V455 And an important test bed for our understanding of the WD instability strip (Szkody et al. 2010; Silvestri et al. 2012).

In this study, we focus on fast spectroscopy resolving the spin cycle of the accreting WD. A strong modulation on the WD spin is expected when the WD is sufficiently magnetic to control the accretion flow onto its surface, funnelling the material onto its poles. Cataclysmic variables with a magnetic WD whose magnetic field is not strong enough to synchronise the WD spin with the orbit of the system are known as intermediate polars (IPs). In most of the known IPs, including V455 And, the region where the accretion flow is controlled by the magnetic field is limited in radial extent from the WD and the bulk of the accretion flow still proceeds via a traditional accretion disc that is steadily fed by the mass donor star.

Studies of the spectral line variations of IPs on the spin period have been performed for a series of IPs with slowly spinning WDs (see e.g., Hellier et al. (1987) for a spin trail of EX Hya, Hellier et al. (1990) for FO Aqr, Hellier et al. (1991) for AO Psc, Hellier (1997) for BG CMi and PQ Gem, and Hellier (1999) for V2400 Oph and V1025 Cen). Of the IPs with faster spinning WDs, however, only spin variations of AE Aqr (Welsh et al. 1998; Reinsch and Beuermann 1994) and DQ Her (Martell et al. 1995; Chap. 2) have been studied. The observed changes in the DQ Her spectra remain largely unexplained. No significant spectral line variations have been detected on the spin period of AE Aqr. This could be explained by the fact that the system is probably a propeller system (Eracleous and Horne 1996; Wynn et al. 1997) in which most of the material lost from the companion gets expelled from the system rather than being accreted on the WD.

The earlier papers on IPs (see Patterson 1994, for a review), suggested variations in the light curve on the spin period to arise from X-ray reprocessing in the disc or bright spot. Reprocessing of X-rays from the magnetic poles of the WD would lead to sinusoidally shaped brightness enhancements in the spin trails, as the beam sweaps around and illuminates different parts of the disc at different spin phases. More recently, it has become clear that magnetically controlled accretion via accretion curtains is likely to have an important influence on the observed light, by its changing orientation (and hence visibility) during a spin cycle, and possibly by acting as an extra reprocessing region. The idea of curtain-like accretion flows from the disc to the magnetic poles of the WD was originally proposed by Rosen et al. (1988).

To better understand the accretion geometry near rapidly spinning WDs, we targeted V455 And which, given its expected spin period of only  $\sim$ 67 s, is one of the

Date	UT	Seeing (arcsec)	Exposure time (s)	Number
11-12/07/2008	02:02-03:59	0.8-1.8	2.0	3102
12-13/07/2008	01:13-05:39	$\approx 0.7$	2.0	7020
13-14/07/2008	01:46-05:25	0.5-0.8	2.0	5674

**Table 3.1** Overview of our spin-resolved spectroscopic observations of V455 And, performed with an EMCCD (QUCAM2) at the blue arm of the ISIS spectrograph at the William Herschel Telescope

See Bloemen et al. (2013) for details

most rapidly spinning WDs known after AE Aqr ( $P_{spin}=33.1\,s$ , Patterson 1979; de Jager et al. 1994) and V842 Cen ( $P_{spin}=56.8\,s$ , Woudt et al. 2009). The required observations are technically challenging given the need to obtain relatively high spectral resolution spectroscopy with very short exposure times. The instrumental setup and data reduction methods involving an electron multiplying CCD are described in detail in Bloemen et al. (2013), to which we refer the reader for details. The observations used in this chapter are summarized in Table 3.1.

#### 3.2 Analysis

Figure 3.1 shows an example single exposure (grey) and the average (black) spectrum of V455 And. Double peaked line profiles of H $\gamma$   $\lambda$ 4340 and He I  $\lambda$ 4471, characteristic for accretion disc emission, can clearly be seen. He II  $\lambda$ 4686 is visible as well, but is much weaker.

# 3.2.1 Frequency Analysis

To search for pulsations in the emission lines, we present a Lomb-Scargle periodogram (Scargle 1982; Lomb 1976) of the net line flux in H $\gamma$  in Fig. 3.2. The net line flux was obtained by integrating the flux in the line (above the continuum level) over a region of 60 Å centered at H $\gamma$ . Our short exposure times allow us to resolve line flux modulations out to several thousand cycles/day. The highest peaks are found at the orbital frequency of  $17.5\,\mathrm{d}^{-1}$ , and its one-day aliases (the window function is shown in grey in the insets, centered at the highest peak). In addition, the highest amplitude peak in the second inset is at 1,277.8 d<sup>-1</sup>. This coherent signal would be most naturally identified as the spin period of the WD, as IPs often show a spin-locked signal in their emission lines. Furthermore, no peak is found above noise level at 1,284.7 d<sup>-1</sup>, which Araujo-Betancor et al. (2005) suggested to be WD spin frequency but is more likely a beat frequency, as explained in Sect. 3.1. The third inset zooms in on the region around 2,555.6 d<sup>-1</sup>, the first harmonic of the spin period whose peak power is higher than the fundamental. The variation of the spectra on

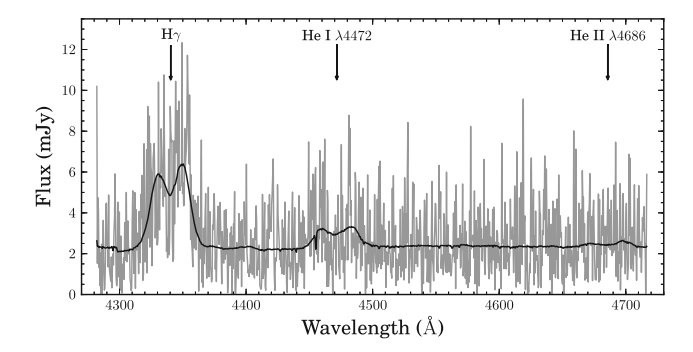


Fig. 3.1 The average (black) blue arm spectrum of V455 And overplotted on a single spectrum (grey)

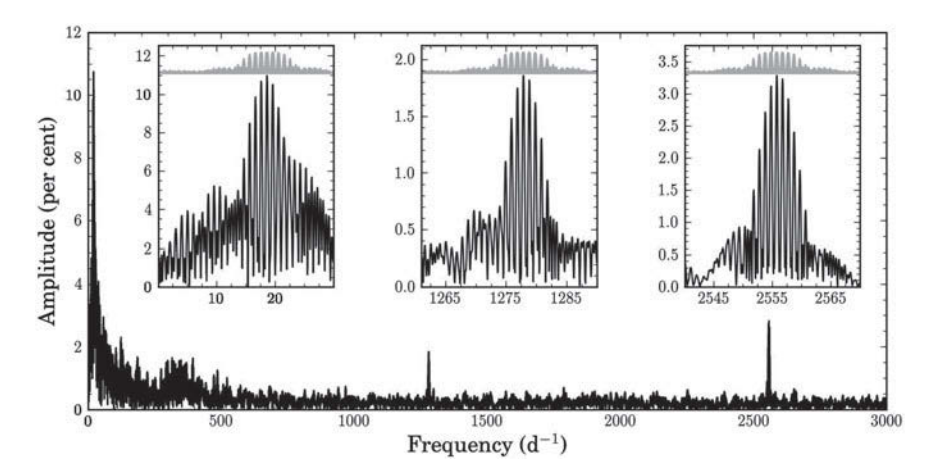


Fig. 3.2 Scargle periodogram of the flux in  $H\gamma$  above the continuum. In the insets, the window function is plotted in *grey*, shifted to the frequency of the strongest peak. The *highest peak* in the *left inset* is  $18.5\,\mathrm{d}^{-1}$  which is the one day alias of the orbital frequency peak at  $17.5\,\mathrm{d}^{-1}$ , which is almost equally strong. In the *second inset*, the highest amplitude is found at  $1,277.8\,\mathrm{d}^{-1}$  which is identified as the spin period of the *white* dwarf. The peak in the *third inset*, at  $2,555.6\,\mathrm{d}^{-1}$ , is the first harmonic of this spin period

the orbital period is further discussed in Sect. 3.2.2 and the variability on the spin period in Sect. 3.2.3.

We do see excess power in the emission line power spectrum near the nominal pulsation period range ( $\sim 300\,d^{-1}$ ). This implies that the pulsation source is not a pure continuum source, but must have a variability component in the  $H_{\gamma}$  line. This could be caused by variability in the underlying Balmer absorption profile from a pulsating WD, but is also consistent with a variable contribution from the line emission sources. Our data cannot distinguish between these two given that both the WD absorption line and the accretion powered emission line have comparable widths and thus, at all

3.2 Analysis 37

velocities where we detect variability, overlap (see Fig. 12 in Araujo-Betancor et al. 2005).

We have also checked the variability in the continuum part of the spectra (between 4,520 and 4,670 Å). We found variability at the same frequencies as in the H $\gamma$  line, but at lower amplitude, except for the variability at 1,277.8 d<sup>-1</sup> which is not detectable above the noise level. This is in agreement with the photometric studies mentioned earlier, which find a much lower variability amplitude at 1,277.8 d<sup>-1</sup> than at the first harmonic of this frequency.

#### 3.2.2 Variations on the Orbital Period

We rebinned the spectra on a constant velocity scale of  $28 \text{ km s}^{-1}$  per pixel and folded the spectra on the orbital ephemeris of Araujo-Betancor et al. (2005). The resulting orbital trails for H $\gamma$ , He I  $\lambda$ 4472 and He II  $\lambda$ 4686 are shown in the upper panels of Fig. 3.3. Apart from the double peaked profile emitted by the accretion disc, a strong bright spot contribution is seen as an S-wave in the trails. A weak WZ Sge-like 'bright spot shadow' (Spruit and Rutten 1998) can be seen in the red-shifted part of the lines at orbital phase  $\sim$ 0.25. Around orbital phase 1, a shallow eclipse is observed. In all three lines, the red-shifted peak appears to be brighter than the blue-shifted peak

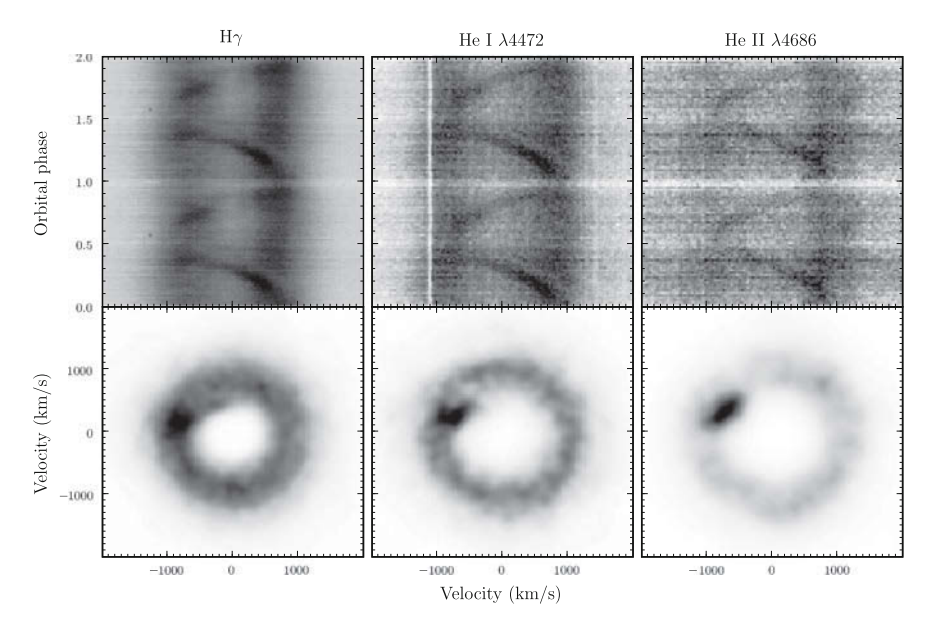


Fig. 3.3 Orbital trails and Doppler maps for H $\gamma$ , He I  $\lambda$ 4472, He II  $\lambda$ 4686. White is minimum flux, black maximum flux. A grazing eclipse can be seen at orbital phase 1. The three lines result in comparable Doppler maps that show emission of the accretion disc (ring) and the bright spot where the mass stream from the companion hits the disc (brighter dot at the ring)

at all orbital phases. This difference is probably due to a slightly warped or slowly precessing accretion disc of which the red-shifted surface was better visible and/or brighter at the time of our observations compared to the blue-shifted side. Comparing night-by-night averages reveals no significant evolution in this line asymmetry across our three nights.

The bottom panels of Fig. 3.3 shows the Doppler maps of the trails, produced using the maximum entropy method as presented by Marsh and Horne (1988) and implemented in the DOPPLER<sup>1</sup> package. The three maps are not significantly different. The accretion disc emission maps onto a diffuse ring. The disc appears to be structureless, as is the case for most IPs but contrary to the prototype DQ Her, which was found to have spiral density structures (see Chap. 2). The dot around  $(V_X, V_Y) \approx (-900, 100) \, \mathrm{km} \, \mathrm{s}^{-1}$  represents the strong bright spot emission component which is hot enough to contribute significantly to He II. No line emission from either the WD or the secondary star is detected. These maps show that the bulk of the line emission originates from an extended accretion disc, implying that any magnetically controlled flow is confined to the zone near the WD.

#### 3.2.3 Variations on the WD Spin Period

To exploit our observational setup and study the changes in the line profiles at the WD's spin period, the spectra were phase folded into 50 bins at the spin period of 67.619 s (1277.75 d<sup>-1</sup>). An average spectrum was subtracted to highlight the spin modulation, similar to the procedure outlined in Chap. 2. The resulting spin trails are shown in Fig. 3.4 for the three spectral lines. The detection of a clear pattern is strong evidence for the fact that, as concluded by Gänsicke (2007), 67.619 s is the true spin

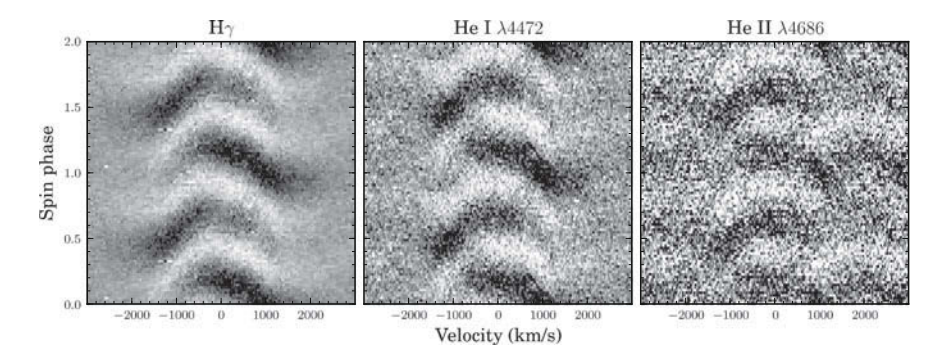


Fig. 3.4 Trails of normalised and mean subtracted line profiles, folded on V455 And's spin period of 67.619 s. The colour scales are  $\pm$  0.5, 0.2 and 0.1 mJy compared to average. White indicates lower than average fluxes, black higher than average

 $<sup>^{1} \ {\</sup>tt DOPPLER} \ is \ available \ for \ download \ at \ http://deneb.astro.warwick.ac.uk/phsaap/software/.$ 

3.2 Analysis 39

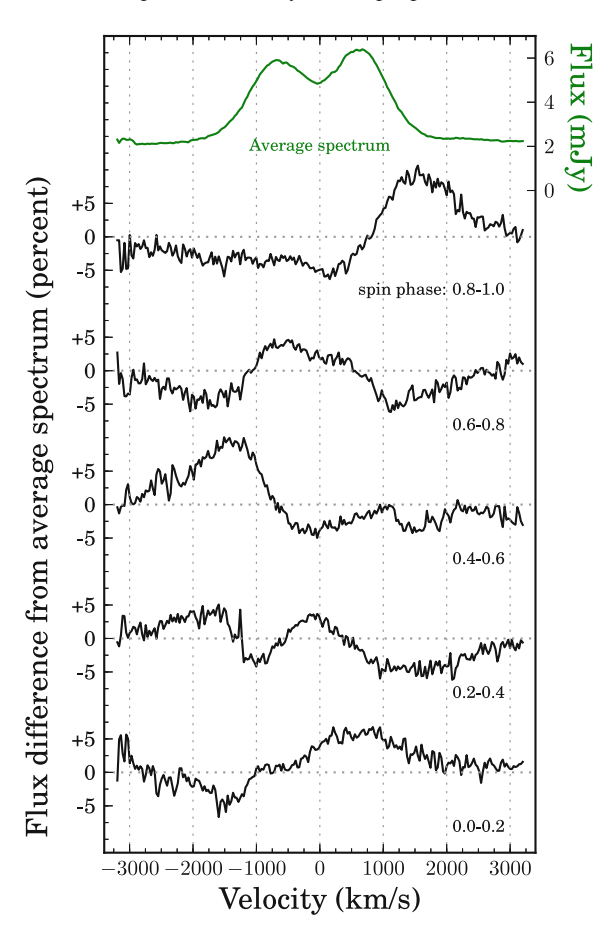
period because folding the spectra on slightly different periods, such as the 67.24s period that was suggested by Araujo-Betancor et al. (2005), washes out the structure. In DQ Her there is still a debate whether the spin signal is at the spin period or its harmonic. Here we can confidently conclude that the folded trails robustly designate  $67.619 \pm 0.002\,\mathrm{s}$  to be the rotation period of the WD, with the power detected at the 1st harmonic caused by the two-sided pattern in Fig. 3.4. The uncertainty on the spin period was determined by comparing how well spin trails of the different nights phase up, after folding the data on various different periods that are slightly different from the optimal spin period value.

The observed pattern is puzzling. Previously published spin trails of IPs with relatively slowly spinning IPs (see references in Sect. 3.1) appear to be totally different to the trails we find for V455 And. Also the recently published spin trails of DQ Her (see Chap. 2), although also being an IP with a fast-spinning WD, are fundamentally different. Firstly, DQ Her's variations in He II λ4686 are found to be much stronger in the red-shifted parts of the line than in the blue-shifted, which is clearly not the case for V455 And. The spin modulations can be detected out to large velocities and their amplitudes peak at velocities significantly beyond the disc peak. To illustrate this, we plot several representative normalised spin profiles in Fig. 3.5. These illustrate the amplitude of the observed spin signal as a function of velocity, with an average emission line profile provided as a reference. The structure in the spin trials and profiles cannot be explained by the 'old school' hypothesis of X-ray reprocessing in the disc and the bright spot. If reprocessing of X-rays by the bright spot contributed significantly, we would expect a higher spin modulation amplitude in the spectral lines at the radial velocity of the bright spot, which would cause the spin pattern to be orbital phase dependent. Spin trails were therefore also produced using subsets of the spectra, taken at selected orbital phase intervals, but no variability of the spin trails over the orbital period could be detected. The complex pattern more likely results from magnetically controlled accretion near the WD. Accretion curtains flowing towards the WD would involve large velocities, switching from maximum to minimal radial velocity as they rotate along the line of sight across 1/4 spin cycle. However, we do not know which exact geometry can explain the observed modulations. A thorough modelling effort of the accretion curtain geometry and its optical properties will be required to quantitatively test this idea and see whether such a geometry could reproduce the observed spin modulations as a function of radial velocity and spin phase.

# 3.3 Summary

We observed the intermediate polar V455 And with the electron multiplying CCD 'QUCAM2' installed at the ISIS spectrograph at the William Herschel Telescope. We demonstrate the potential of this detector to observe faint targets at high cadence. With a conventional detector, spin-resolved spectroscopy of the IPs with the fastest spinning WDs would be hard if not impossible to achieve as readout noise would

Fig. 3.5 Five spin profiles for the H $\gamma$  line normalised to show the spin modulation in percent compared to the average line profile at the *top*. The spin modulation peaks at velocities well beyond the disc peaks and can be detected out to large radial velocities



swamp any signal. We developed a strategy to reduce the faint spectra, making full use of a brighter in-slit comparison star and correcting for instrument and telescope flexure.

We were able to detect strong coherent signals in our time-series allowing us to robustly identify the spin period of the WD to be  $67.619\pm0.002\,\mathrm{s}$ , which confirms the spin period reported by Gänsicke (2007). Furthermore, by folding our 15 796 spectra on this spin period, a complex emission line variation is recovered, resolving the spin modulation as a function of both radial velocity as well as spin phase. The observed variations are totally different from the results of previous observations of other intermediate polars, including the canonical IP DQ Her discussed in Chap. 2. We believe that the observed patterns are evidence of magnetically controlled accretion curtains near the WD, but are not aware of any specific model that can reproduce our observations in detail.

References 41

#### References

Araujo-Betancor, S., Gänsicke, B. T., Hagen, H., Marsh, T. R., Harlaftis, E. T., Thorstensen, J. et al. (2005) A&A, 430, 629.

Bloemen, S., Steeghs, D., De Smedt, K., Vos, J., Gänsicke, B. T., Marsh, T. R., et al. (2013). *MNRAS*, 429, 3433.

de Jager, O. C., Meintjes, P. J., O'Donoghue, D., & Robinson, E. L. (1994). MNRAS, 267, 577.

Eracleous, M., & Horne, K. (1996). ApJ, 471, 427.

Gänsicke, B. T. (2007). In R. Napiwotzki & M. R. Burleigh, (Ed.), 15th European Workshop on White Dwarfs, Vol. 372 of Astronomical Society of the Pacific Conference Series, HS 2331+3905, the Brightest CV White Dwarf Pulsator. p. 597.

Hellier, C. (1999). In C. Hellier, K. Mukai (Eds.), Annapolis Workshop on Magnetic Cataclysmic Variables, Vol. 157 of Astronomical Society of the Pacific Conference Series, Recent results on intermediate polars. p. 1.

Hellier, C., Mason, K. O., Rosen, S. R., & Cordova, F. A. (1987). MNRAS, 228, 463.

Hellier, C., Mason, K. O., & Cropper, M. (1990), MNRAS, 242, 250.

Hellier, C., Cropper, M., & Mason, K. O. (1991). MNRAS, 248, 233.

Hellier, C. (1997). MNRAS, 288, 817.

Lomb, N. R. (1976). Ap&SS, 39, 447.

Marsh, T. R., & Horne, K. (1988). MNRAS, 235, 269.

Martell, P. J., Horne, K., Price, C. M., & Gomer, R. H. (1995). ApJ, 448, 380.

Matsui, R., Uemura, M., Arai, A., et al. (2009). PASJ, 61, 1081.

Patterson, J. (1979). ApJ, 234, 978.

Patterson, J. (1994). PASP, 106, 209.

Pyrzas, S. (2011) Ph.D. thesis, University of Warwick, UK.

Reinsch, K., & Beuermann, K. (1994). A&A, 282, 493.

Rosen, S. R., Mason, K. O., & Cordova, F. A. (1988). MNRAS, 231, 549.

Scargle, J. D. (1982). ApJ, 263, 835.

Silvestri, N. M., Szkody, P., Mukadam, A. S., Hermes, J. J., Seibert, M., Schwartz, R. D., et al. (2012). *AJ*, 144, 84.

Spruit, H. C., & Rutten, R. G. M. (1998). MNRAS, 299, 768.

Szkody, P., Mukadam, A., Gänsicke, B. T., Henden, A., Templeton, M., Holtzman, J., et al. (2010). *ApJ*, 710, 64.

Tovmassian, G. H., Zharikov, S. V., & Neustroev, V. V. (2007). ApJ, 655, 466.

Welsh, W. F., Horne, K., & Gomer, R. (1998). MNRAS, 298, 285.

Woudt, P. A., Warner, B., Osborne, J., & Page, K. (2009). MNRAS, 395, 2177.

Wynn, G. A., King, A. R., & Horne, K. (1997). MNRAS, 286, 436.

# Chapter 4 *Kepler* Observations of the Beaming Binary KPD 1946+4340

Abstract The Kepler Mission has acquired 33.5d of continuous one-minute photometry of KPD 1946+4340, a short-period binary system that consists of a subdwarf B star (sdB) and a white dwarf. In the light curve, eclipses are clearly seen, with the deepest occurring when the compact white dwarf crosses the disc of the sdB (0.4%) and the more shallow ones (0.1%) when the sdB eclipses the white dwarf. As expected, the sdB is deformed by the gravitational field of the white dwarf, which produces an ellipsoidal modulation of the light curve. Spectacularly, a very strong Doppler beaming (also known as Doppler boosting) effect is also clearly evident at the 0.1 % level. This originates from the sdB's orbital velocity, which we measure to be  $164.0 \pm 1.9 \,\mathrm{km \, s^{-1}}$  from supporting spectroscopy. We present light curve models that account for all these effects, as well as gravitational lensing, which decreases the apparent radius of the white dwarf by about 6% when it eclipses the sdB. We derive system parameters and uncertainties from the light curve using Markov Chain Monte Carlo simulations. Adopting a theoretical white dwarf mass-radius relation, the mass of the subdwarf is found to be  $0.47 \pm 0.03 \,\mathrm{M}_{\odot}$  and the mass of the white dwarf  $0.59 \pm 0.02 \,\mathrm{M_{\odot}}$ . The effective temperature of the white dwarf is  $15,900 \pm 300 \,\mathrm{K}$ . With a spectroscopic effective temperature of  $T_{\rm eff} = 34{,}730 \pm 250 \,\rm K$  and a surface gravity of  $\log q = 5.43 \pm 0.04$ , the subdwarf has most likely exhausted its core helium, and is in a shell He burning stage. The detection of Doppler beaming in Kepler light curves potentially allows one to measure radial velocities without the need of spectroscopic data. For the first time, a photometrically observed Doppler beaming amplitude is compared to a spectroscopically established value. The sdB's radial velocity amplitude derived from the photometry (168  $\pm$  4 km s<sup>-1</sup>) is in perfect agreement with the spectroscopic value. After subtracting our best model for the orbital effects, we searched the residuals for stellar pulsations but did not find any significant pulsation frequencies.

This chapter is based on

S. Bloemen, T. R. Marsh, R. H. Østensen, S. Charpinet, G. Fontaine, P. Degroote,

U. Heber, S. D. Kawaler, C. Aerts, E. M. Green, J. Telting, P. Brassard, B. T. Gänsicke,

G. Handler, D. W. Kurtz, R. Silvotti, V. Van Grootel, J. E. Lindberg, T. Pursimo, P. A. Wilson,

R. L. Gilliland, H. Kjeldsen, J. Christensen-Dalsgaard, W. J. Borucki, D. Koch, J. M. Jenkins,

T. C. Klaus, Monthly Notices of the Royal Astronomical Society, 2011, vol. 410, pp. 1787–1796.

#### 4.1 KPD 1946+4340 Among the Subdwarf B Stars

Subdwarf B stars are mostly assumed to be extreme horizontal branch stars, i.e., core helium burning stars with a thin inert hydrogen envelope (Heber 1986; Saffer et al. 1994). In order to reach such high temperatures and surface gravities, the progenitor must have lost almost its entire hydrogen envelope. The majority of sdBs is expected to have lost its envelope via binary interaction channels, as elaborated by Han et al. (2002, 2003). Our target, KPD 1946+4340 (KIC 7975824), is a subdwarf B star (sdB) with a white dwarf (WD) companion in a 0.403739(8) day orbit (Morales-Rueda et al. 2003), which identifies the theoretical formation channel for this system as the second common-envelope ejection channel of Han et al. (2002, 2003). In this scenario the white dwarf is engulfed by the sdB progenitor as it ascends the first giant branch. The white dwarf will deposit its angular momentum in the atmosphere of the giant and spin up the envelope until it is ejected. There are two subchannels to this scenario, depending on the initial mass of the progenitor. If sufficiently massive, it will ignite helium non-degenerately, and the resulting extended horizontal branch (EHB) star will have a mass of  $\sim 0.35 \,\mathrm{M_{\odot}}$ . The more common scenario, starting with a roughly solar-mass giant, produces an EHB star with a mass that must be very close to the canonical mass of  $0.47\,\mathrm{M}_{\odot}$  at the occurrence of the helium flash. A third possibility occurs when the white dwarf companion ejects the envelope before the core has attained sufficient mass to ignite helium. In this case the remaining core will evolve directly to the white dwarf cooling track. On its way it crosses the domain of the EHB stars, but, without helium ignition, the period in which it appears as an sdB star is brief, making this channel a very small contributor to the sdB population. For a recent extensive review on hot subdwarf stars, their evolution and observed properties, see Heber (2009).

The exact physical details involved in common-envelope (CE) ejection are not well understood. This uncertainty is commonly embodied in the efficiency parameter  $\alpha$ , which denotes the amount of orbital energy used to eject the envelope (see e.g. de Kool 1990; Hu et al. 2007). Eclipsing subdwarf binaries could help constrain the permitted values of  $\alpha$ , but studies have hitherto been hampered by the fact that both sdB+WD and sdB+M-dwarf binaries have virtually invisible companions and are therefore single lined, leaving the masses indeterminate. Firmly establishing the parameters of both components of a post-CE system therefore has substantial implications not just for confirming that our formation scenarios are correct, but also in order to tune future binary population synthesis studies by confining the  $\alpha$  parameter.

The target studied here, KPD 1946+4340, is an sdB star discovered by the *Kitt Peak Downes* survey (Downes 1986). KPD 1946+4340 has a *V*-band magnitude of 14.284  $\pm$  0.027 (Allard et al. 1994), a *y*-magnitude of 14.299  $\pm$  0.002 (Wesemael et al. 1992) and a *Kp* (*Kepler*) magnitude of 14.655. The star was included in the radial velocity survey of Morales-Rueda et al. (2003), who found the target to be a spectroscopic binary with a period of 0.403739(8)d and a velocity amplitude  $K_1 = 167 \pm 2 \,\mathrm{km \, s^{-1}}$ . They also concluded that the sdB primary should be in a

post-EHB stage of evolution, due to its relatively low surface gravity placing it above the canonical EHB in the HR diagram. This implies that the sdB exhausted all available helium in its core and is now in a helium shell burning stage. Assuming the sdB mass to be  $0.5\,M_{\odot}$ , they found a minimum mass of  $0.628\,M_{\odot}$  for the companion.

In this chapter we present the first light curve of KPD 1946+4340 obtained from space. The target was observed for 33.5 d by the *Kepler Mission*, and the light curve reveals sufficient low level features to permit purely photometric measurements of velocities, radii and masses of both components. A review of the *Kepler Mission* and its first results is given in Koch et al. (2010).

We combine the *Kepler* photometry with new and old spectroscopic measurements, use light curve modelling to estimate the system parameters and Markov Chain Monte Carlo (MCMC) simulations to establish the uncertainties. The relativistic Doppler beaming effect is clearly detected in the light curve, and can be used to determine the orbital velocity of the primary. This effect, which is also known as Doppler boosting, was recently noted in a *Kepler* light curve of KOI-74 by van Kerkwijk et al. (2010). We present the first comparison of a radial velocity amplitude as derived from the amplitude of the Doppler beaming to the spectroscopically determined value. We also use the spectroscopic data to provide a revised ephemeris, as well as to determine the effective temperature, surface gravity and helium fraction of the atmosphere. After detrending the *Kepler* light curve with our best model for the orbital effects, we search the residuals for stellar pulsations.

# 4.2 Observations, Radial Velocities and Updated Ephemeris

We used 33.5 d of Q1 short cadence *Kepler* data with a time resolution of 59 s. A general review of the characteristics of the first *Kepler* short cadence datasets is presented by Gilliland et al. (2010), while the treatment of the data for KPD 1946+4340is fully described in Bloemen et al. (2011), to which we refer for details. The full light curve we used for our analysis is shown on Fig. 4.1. The time span of the dataset is BMJD(TDB)<sup>1</sup> 54 964.00314–54 997.49381.

The high signal-to-noise spectra from Green et al. (2008) were used to derive  $T_{\rm eff}$  and  $\log g$ ; see Sect. 4.4 for details. To refine the orbital period determination of Morales-Rueda et al. (2003), spectra were collected with the 2.56 m Nordic Optical Telescope (NOT) (see Bloemen et al. 2011, for details). The radial velocities are listed in Table 4.1. We carried out a least-squares sinusoidal fit to the combined dataset finding a best fit of  $\chi^2=21.6$  (25 points). The next best alias had  $\chi^2=39$ , and so we consider our best alias to be the correct one. This gave the following spectroscopic ephemeris:

BMJD(TDB) = 
$$53652.84813(62) + 0.40375026(16)E$$
,

<sup>&</sup>lt;sup>1</sup> BMJD(TDB) refers to Barycentric-corrected Modified Julian Date on the Barycentric Dynamical Timescale.

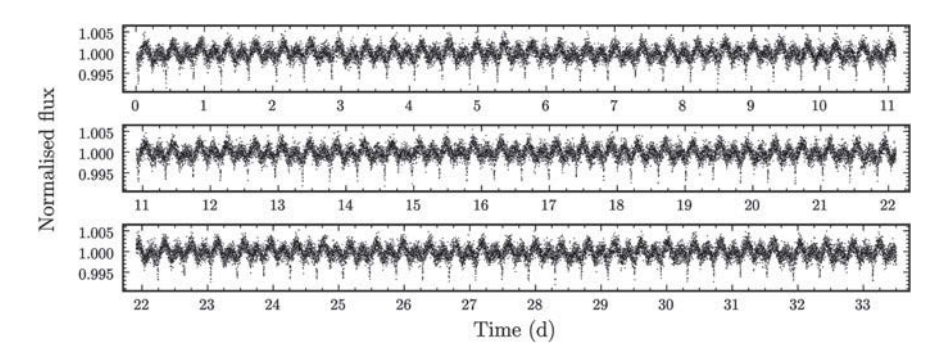


Fig. 4.1 Kepler light curve of KPD 1946+4340 after detrending and removing outliers

**Table 4.1** Radial velocities of the sdB in KPD 1946+4340 determined from NOT spectroscopy

BMJD (TDB)	RV (km s <sup>-1</sup> )
55170.81118	$-139.8 \pm 3.5$
55170.86268	$-162.0 \pm 3.3$
55170.90743	$-109.2 \pm 3.8$
55170.95896	$22.5 \pm 5.7$
55174.80952	$-73.5 \pm 3.0$
55174.84999	$-154.7 \pm 3.3$
55174.90291	$-171.9 \pm 4.0$
55174.93220	$-127.6 \pm 4.7$
55175.80006	$2.3 \pm 4.4$
55175.84379	$102.4 \pm 4.7$
55175.88328	$148.3 \pm 6.5$

marking the times when the sdB is closest to Earth. The corresponding radial velocity amplitude was  $K_1 = 164.0 \pm 1.9 \, \mathrm{km \, s^{-1}}$ . The WD's spectrum will slightly reduce the observed velocity amplitude of the sdB. We estimate that this effect is less than  $1 \, \mathrm{km \, s^{-1}}$ . The radial velocity measurements and the fit are shown in Fig. 4.2. From fitting light curve models to the *Kepler* photometry (see Sect. 4.3.3) we derived the following photometric ephemeris:

BMJD(TDB) = 
$$54\,979.975296(25) + 0.40375000(96)E$$
.

The two independent periods agree to within their uncertainties. The 9 yr baseline of the spectroscopic ephemeris gives a more precise value and henceforth we fix it at this value in our light curve models. The cycle count between the spectroscopic and photometric ephemerides (using the spectroscopic period) is  $3287.0001 \pm 0.0015$ , an integer to within the uncertainties. The *Kepler*-based zeropoint is the more precise one and is therefore retained as a free parameter in our models.

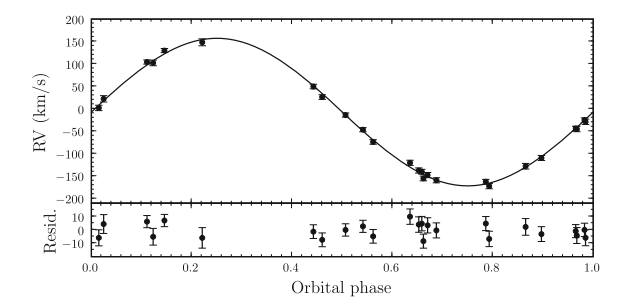


**Fig. 4.2** Radial velocity curve of the sdB in KPD 1946+4340. Both our new radial velocity measurements and the ones from Morales-Rueda et al. (2003) are shown, folded on the orbital period. The error bars of the datapoints show the uncertainties after adding  $3.6\,\mathrm{km\,s^{-1}}$  and  $4.1\,\mathrm{km\,s^{-1}}$  in quadrature to the values of Morales-Rueda et al. (2003) and our new data respectively. We find a radial velocity amplitude of  $K_1 = 164.0 \pm 1.9\,\mathrm{km\,s^{-1}}$ 

#### 4.3 Light Curve Analysis

The *Kepler* light curve we analyse in this chapter (Fig. 4.1) reveals that KPD 1946+4340 is an eclipsing binary. We graphically determined the eclipse depths and durations. The eclipses of the WD by the sdB are  $0.13 \pm 0.03\%$  deep and the eclipses of the sdB by the white dwarf  $0.38 \pm 0.03\%$ . The duration of the eclipses at half maximum depth is  $0.0236 \pm 0.0003$  in orbital phase units. There is a clear asymmetric ellipsoidal modulation pattern in which the flux maximum after the deeper eclipses is larger than the maximum after the shallower eclipses. We attribute this to Doppler beaming, see Sect. 4.3.2.

To determine the system properties, we modelled the light curve with the LCURVE code written by TRM (for a description of the code, see Copperwheat et al. 2010 Appendix A). This code uses grids of points to model the two stars, taking into account limb darkening, gravity darkening, Doppler beaming and gravitational lensing when the white dwarf eclipses its companion. It assumes the ellipsoidally deformed star to be in corotation with the binary orbit, which is usually a good assumption because of the large tidal interactions between the two binary components. Reprocessing of light from the sdB by the WD is included in the light curve models as well ("reflection effect").

To speed up the computation of the models used in this chapter we implemented a new option in the code whereby a finer grid can be used along the track of the white dwarf as it eclipses the sdB. This reduces the overall number of points needed to model the light curve to the demanding precision required to model the *Kepler* data. In addition, we only used the finely-spaced grid during the eclipse phases, taking care to make the model values continuous when changing between grids by applying normalisation factors (very close to unity) to the coarse grid fluxes. We used  $\sim 100,000~(\sim 37,000)$  grid points for the fine (coarse) grids for the sdB and 3000 for the white dwarf. To model the finite exposures more accurately during the eclipses,

where smearing occurs due to the 1 m integration time, we calculated 7 points for each exposure (i.e., one point for every  $\sim 10$  s) and took their trapezoidal average.

# 4.3.1 Gravity Darkening and Limb Darkening Coefficients

We used model spectra to compute the gravity darkening coefficient (GDC) of the sdB and the limb darkening coefficients for both the sdB and the white dwarf, which are all important parameters for the modeling of a close binary's light curve. The GDC is needed to model the effects of the white dwarf's gravity on the sdB, which slightly distorts the sdB's shape. The bolometric flux from a stellar surface depends on the local gravity as  $T^4 \propto g^{\beta_b}$  in which  $\beta_b$  is the bolometric GDC. For radiative stars,  $\beta_b = 1$  (von Zeipel 1924). We observe the band-limited stellar flux, not the bolometric flux, and hence we require a different coefficient defined by  $I \propto g^{\beta_K}$ . The GDC for the *Kepler* bandpass,  $\beta_K$  was computed from

$$\beta_K = \frac{\mathrm{d}\log I}{\mathrm{d}\log g} = \frac{\partial\log I}{\partial\log g} + \frac{\partial\log I}{\partial\log T} \frac{\mathrm{d}\log T}{\mathrm{d}\log g} \tag{4.1}$$

in which I is the photon-weighted bandpass-integrated specific intensity at  $\mu=1$  and  $\frac{d \log T}{d \log g}=\frac{\beta_b}{4}=0.25$ . We used a grid of sdB atmosphere models calculated from the LTE model atmosphere grid of Heber et al. (2000) using the Linfor program (Lemke 1997) and assumed  $T_{\rm eff}=34,500{\rm K}$ ,  $\log g=5.5$ ,  $\log (n_{\rm He}/n_{\rm H})=-1.5$  and  $\log (Z/Z_{\odot})=-2$ . To estimate the interstellar reddening, we compared the observed B-V colour of  $-0.20\pm0.01$  mag (Allard et al. 1994) with the colours expected from a model atmosphere. We found an intrinsic colour of B-V=-0.26 mag and consequently adopted a reddening of E(B-V)=0.06. To account for this interstellar reddening the model spectra were reddened following Cardelli et al. (1989). The gravity darkening coefficient was found to be  $\beta_K=0.448$ .

Using a model for the same set of parameters, we computed limb darkening coefficients for the sdB. We adopted the 4-parameter limb darkening relation of Claret (2004, Eq. 5) and determined  $a_1 = 0.818$ ,  $a_2 = -0.908$ ,  $a_3 = 0.755$  and  $a_4 = -0.252$ .

For the white dwarf, angle-dependent model spectra were calculated using the code of Gänsicke et al. (1995) for  $T_{\rm eff}=17,000\,\rm K$  (estimated from a comparison of model surface brightnesses given initial light curve fits) and  $\log g=7.8$ . We adopted the same limb darkening law as for the sdB and found  $a_1=0.832, a_2=-0.681, a_3=0.621$  and  $a_4=-0.239, a_2=-0.669, a_3=0.612$  and  $a_4=-0.236$ .

# 4.3.2 Doppler Beaming Factor

The asymmetry in KPD 1946+4340's ellipsoidal modulation pattern is the result of Doppler beaming. Doppler beaming is caused by the stars' radial velocity shifting the

spectrum, modulating the photon emission rate and beaming the photons somewhat in the direction of motion. The effect was, as far as we are aware, first discussed in Hills and Dale (1974) for rotation of white dwarfs and by Shakura and Postnov (1987) for orbital motion in binaries. It was first observed by (Maxted et al., 2000). Its expected detection in *Kepler* light curves was suggested and discussed by Loeb and Gaudi (2003) and Zucker et al. (2007). Van Kerkwijk et al. (2010) report the detection of Doppler beaming in the long cadence *Kepler* light curve of the binary KOI-74. For the first time, they measured the radial velocity of a binary component from the photometrically detected beaming effect. The measured radial velocity amplitude, however, did not match the amplitude as expected from the mass ratio derived from the ellipsoidal modulation in the light curve. When this chapter was published, the derived velocity of the primary of KOI-74 was yet to be confirmed spectroscopically. We discuss this spectroscopic confirmation in Chap. 5. For KPD 1946+4340, radial velocities were available before the launch of the *Kepler Mission*, which allows the first spectroscopic check of a photometrically determined radial velocity.

For radial velocities that are much smaller than the speed of light, the observed flux  $F_{\lambda}$  is related to the emitted flux  $F_{0,\lambda}$  as

$$F_{\lambda} = F_{0,\lambda} \left( 1 - B \frac{v_r}{c} \right), \tag{4.2}$$

with B the beaming factor

$$B = 5 + \mathrm{d} \ln F / \mathrm{d} \ln^{\circ} \tag{4.3}$$

(Loeb and Gaudi 2003). The beaming factor thus depends on the spectrum of the star and the wavelength of the observations. For the broadband *Kepler* photometry, we use a photon weighted bandpass-integrated beaming factor

$$\langle B \rangle = \frac{\int \epsilon_{\lambda} \lambda F_{\lambda} B \, d\lambda}{\int \epsilon_{\lambda} \lambda F_{\lambda} \, d\lambda} \tag{4.4}$$

in which  $\epsilon_{\lambda}$  is the response function of the *Kepler* bandpass.

We determined the beaming factor from a series of fully metal line-blanketed LTE models (Heber et al. 2000, see also Sect. 4.3.1) with metallicities ranging from  $\log{(Z/Z_{\odot})} = -2$  to +1, as well as from NLTE models with zero metals and with Blanchette metal composition (see Sect. 4.4 of this paper for more information about the NLTE models). Without taking reddening into account, the beaming factor is found to be  $\langle B \rangle = 1.30 \pm 0.03$ . The uncertainty incorporates the dependence of the beaming factor on the model grids and the uncertainty on the sdB's effective temperature, gravity and, most importantly, metallicity. The metal composition of the model atmospheres is a poorly known factor that can only be constrained with high-resolution spectroscopy.

The effect of reddening has to be accounted for by changing the spectral response accordingly, instead of reddening the model atmosphere spectrum. Using a

reddened spectrum would in this case erroneously imply that the reddening is caused by material that is co-moving with the sdB star. With reddening, the beaming factor is determined to be  $\sim$ 0.006 lower. Reddening thus only marginally affects the beaming of KPD 1946+4340 but should certainly be taken into account in case of higher reddening values.

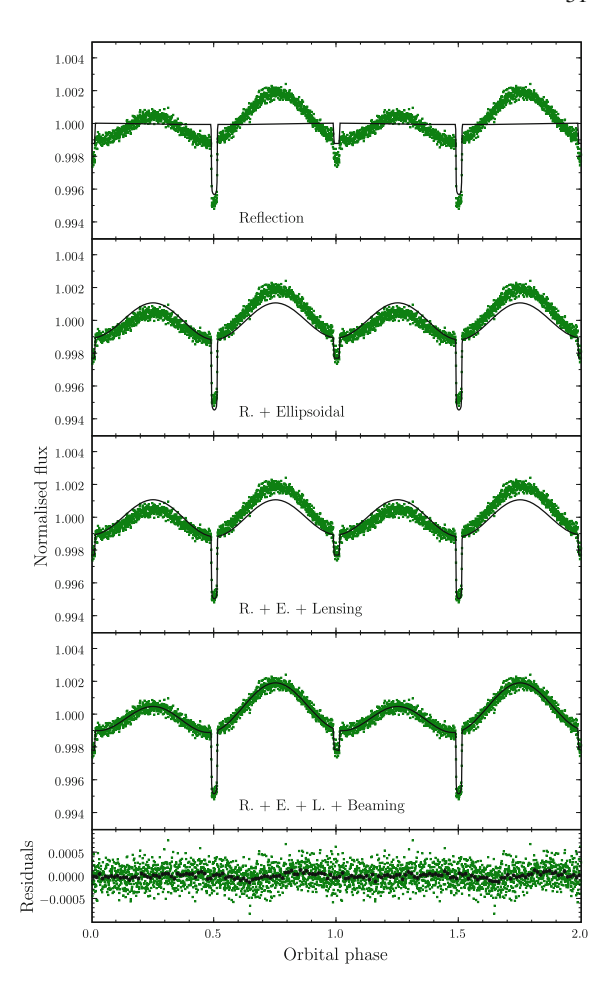
There are three contributions to the beaming factor. The enhanced photon arrival rate of an approaching source contributes +1 to the beaming factor. Aberration also increases the number of photons that is observed from an approaching source, adding +2 to the beaming factor because of the squared relation between normal angle and solid angle. Finally, when the sdB comes towards us, an observed wavelength  $\lambda_o$  corresponds to an emitted wavelength  $\lambda_e = \lambda_o \, (1 + v_r/c)$ . Since sdBs are blue, looking at a longer optical wavelength reduces the observed flux which counteracts the other beaming factor components. In case of an infinite temperature Rayleigh-Jeans spectrum, this Doppler shift contribution to the beaming factor would be -2. For the primary of KPD 1946+4340, we find a contribution of  $\sim -1.70$  which brings the total beaming factor to  $\sim 1.30$ . The contribution of the Doppler shift does not always have to be negative; a red spectrum could actually increase the effect of beaming.

#### 4.3.3 Light Curve Model

A typical fit to the data is shown in Fig. 4.3, with the different contributions switched on, one-by-one. From the residuals (bottom panel) it is clear that the model reproduces the variations at the orbital period very well. When we fit the light curve outside the eclipses with sine curves to represent the reflection effect, ellipsoidal modulation and the beaming, the phase of the ellipsoidal modulation is found to be off by  $0.0072 \pm 0.0010$  in orbital phase units. We do not know the origin of this offset, which also gives rise to the shallow structure that is left in the residuals. Our best fits have a reduced  $\chi^2$  of 1.06.

The significance of the Doppler beaming is obvious, and even the more subtle gravitational lensing effect is very significant, although it cannot be independently deduced from the data since it is highly degenerate with changes in the white dwarf's radius and temperature. One part of the gravitational lensing is caused by light from the sdB that is bent around the white dwarf, effectively making the white dwarf appear smaller. The second lensing contribution is a magnification effect which is caused by the altered area of the sdB that is visible, given that surface brightness is conserved by the lensing effect. In the case of KPD 1946+4340, the first part of the lensing is the most important. Lensing effects in compact binaries were discussed in e.g. Maeder (1973), Gould (1995), Marsh (2001) and Agol (2002, 2003). Sahu and Gilliland (2003) explored the expected influence of microlensing effects on light curves of compact binaries and planetary systems observed by *Kepler*. They found that the lensing effect of a typical white dwarf at 1 AU of a main sequence star will swamp the eclipse signal. A transit of a planet, which is of similar size but a lot less

Fig. 4.3 Phase-folded light curve of KPD 1946+4340 (green, datapoints grouped by 30) and our best fitting model (black). In the top panel, only the eclipses and reflection effects are modelled. In the second panel, ellipsoidal modulation is added. In the third panel, gravitational lensing is taken into account as well, which affects the depth of the eclipse at orbital phase 0.5. The bottom panels show the full model—taking into account Doppler beaming—and the residuals (grouped by 30 in green and grouped by 600 in black)



massive, can therefore easily be distinguished from an eclipse by a white dwarf. In the case of KPD 1946+4340, the separation of the two components is a lot less. An eclipse is still seen, but with reduced depth. For the most likely system parameters, gravitational lensing reduces the eclipse depth by  $\sim$ 12% which is equivalent to a  $\sim$ 6% reduction of the apparent white dwarf radius. The effect of gravitational lensing is implemented in our light curve modelling code following Marsh (2001).

#### 4.3.4 Markov Chain Monte Carlo Simulation

The parameters which determine models can be fixed by minimisation of  $\chi^2$ . If the signal-to-noise is high, a quadratic approximation around the point of minimum  $\chi^2$ 

can lead to the uncertainties of, and correlations between, the best-fit parameters. The *Kepler* data have superb signal-to-noise, but owing to the very shallow depths of the eclipses the quadratic approximation does not work well. Strong correlations between several parameters play a significant role in this problem. The duration of the eclipses essentially fix the scaled radius of the sdB star (which we take to be the primary)  $r_1 = R_1/a$ , where a is the binary separation. The scaled radius is a function of orbital inclination i,  $r_1 = r_1(i)$ . The depth of the eclipse of the sdB by the white dwarf fixes the ratio of radii  $r_2/r_1 = R_2/R_1$ , so  $r_2$  is also a function of orbital inclination. The duration of the ingress and egress features provides an independent constraint on  $r_2$  as a function of i, which can break the degeneracy. In this case, however, one is limited by a combination of signal-to-noise and the minute-long cadence which is not sufficient to resolve the ingress/egress features.

Under these circumstances, a Markov Chain Monte Carlo (MCMC) method can be very valuable. The MCMC method allows one to build up a sequence of models in which the fitting parameters, which we denote by the vector  $\mathbf{a}$ , have a probability distribution matching the Bayesian posterior probability of the parameters given the data,  $P(\mathbf{a}|\mathbf{d})$ . From long chains of models one can then calculate variances and plot confidence regions. The MCMC method also has the side benefit of helping with the minimisation which can become difficult when parameters are highly correlated. For data in the form of independent Gaussian random variables, this probability can be written as

$$P(\mathbf{a}|\mathbf{d}) \propto P(\mathbf{a})e^{-\chi^2/2},$$
 (4.5)

i.e., the product of one's prior knowledge of the model parameters and a factor depending upon the goodness of fit as expressed in  $\chi^2$ . We implemented the MCMC method following procedures along the line of Collier Cameron et al. (2007). We incorporated prior information in two ways. In all cases we used our constraint  $K_1 = 164 \pm 2 \,\mathrm{km}\,\mathrm{s}^{-1}$ . Using our own spectroscopic analysis and the results of Morales-Rueda et al. (2003), we decided to put also the following constraint on the effective temperature of the sdB:  $T_1 = 34,500 \pm 400 \,\mathrm{K}$ . These two constraints were applied by computing the following modified version of  $\chi^2$ 

$$-2\ln\left(P(\mathbf{a}|\mathbf{d})\right) = \chi^2 + \left(\frac{K_1 - 164}{2}\right)^2 + \left(\frac{T_1 - 34,500}{400}\right)^2,\tag{4.6}$$

where  $K_1$  and  $T_1$  are the values in the current MCMC model under test. The period of the binary orbit was kept fixed at the spectroscopically determined value (see Sect. 4.2). The parameters that were kept free during the modelling are the scaled stellar radii  $R_1/a$  and  $R_2/a$ , the mass ratio q, the inclination i, the effective temperature of the WD  $T_2$ , the beaming factor  $\langle B \rangle$  and the zero point of the ephemeris. The radial velocity scale (which leads to the masses  $M_1$  and  $M_2$ ) and the effective temperature of the primary  $T_1$  were included in the fits as well, but with the spectroscopically allowed range as a prior constraint. Note that the beaming factor  $\langle B \rangle$  is kept as a free parameter, which allows the code to fit the Doppler beaming amplitude

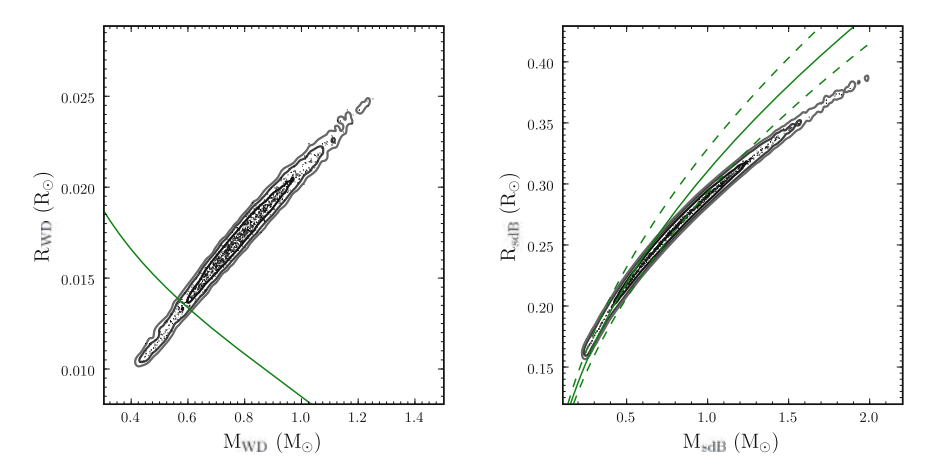


Fig. 4.4 Mass-radius relations of the WD (left) and sdB (right). One tenth of our MCMC models are shown ( $black\ dots$ ). The contour plots show the regions in which 68, 95 and 99% of the models reside. The contours that are shown are somewhat artificially broadened by the binning process. The Eggleton mass-radius relation, inflated by a factor 1.08 to allow for the finite WD temperature (see text for details), is shown as a *solid green* track on the left plot. The mass-radius relation intersects the Eggleton relation very nearly within its 1- $\sigma$  region. On the right panel the solid green line gives the mass-radius relation for  $\log g = 5.45$ , the  $dashed\ lines$  for  $\log g = 5.40\ (left)$  and  $\log g = 5.50\ (right)$ 

while we constrain the allowed range of  $K_1$ . By comparing the MCMC results for  $\langle B \rangle$  with the theoretical beaming factor, we can check if the beaming amplitude is consistent with our expectations.

As explained above, this led to parameter distributions with strong correlations between  $R_1$ ,  $R_2$ ,  $M_1$ ,  $M_2$ , q, etc. The mass-radius relations for the two stars are shown in Fig. 4.4. The favoured parameters for the secondary (left panel) clearly show that it is a white dwarf and the allowed distribution nicely crosses the expected track of mass-radius (solid green line) which we calculated from the zero temperature relation of Eggleton (quoted in Verbunt and Rappaport 1988), inflated by a factor of 1.08. We estimated this factor from the cooling models of Holberg and Bergeron (2006) for white dwarfs with a mass between 0.5 and 0.7  $M_{\odot}$  (white dwarfs with masses outside this range are ruled out by the mass-radius relation) using our preferred temperature for the white dwarf of around 16,000 K and assuming an envelope that consists of  $M_{\rm H} = 10^{-4}\,{\rm M_{WD}}$  and  $M_{\rm He} = 10^{-2}\,{\rm M_{WD}}$ .

Given that the secondary is a white dwarf and given that the secondary's theoretical mass-radius relation intersects the mass-radius distribution very nearly within the 1- $\sigma$  region, we also undertook MCMC runs where we added the prior constraint that the secondary had to match the white dwarf M-R relation to within an RMS of 5%. This was added in exactly the same manner as the  $K_1$  and  $T_1$  constraints. The system parameters we derive from these MCMC runs are listed in Table 4.2. The mass-radius relation after applying the constraint is shown in Fig. 4.5. Especially after applying the white dwarf mass-radius relation constraint, the sdB's mass-radius relation fits perfectly with the one defined by the surface gravity derived from spectroscopy in

	Primary (sdB)	Secondary (WD)		
P <sub>orb</sub> (d)		0.40375026(16)		
$\overline{q}$		$1.27 \pm 0.06$		
i (deg)		$87.14 \pm 0.15$		
<i>R</i> (R <sub>⊙</sub> )	$0.212 \pm 0.006$	$0.0137 \pm 0.0004$		
<i>M</i> (M <sub>☉</sub> )	$0.47 \pm 0.03$	$0.59 \pm 0.02$		
T <sub>eff</sub> (K)	$34.500 \pm 400$	$15.900 \pm 300$		

**Table 4.2** Properties of KPD 1946+4340. The orbital period and the effective temperature of the sdB were derived from spectroscopy

The other parameters are obtained by modelling the *Kepler* light curve. The uncertainties on these values are determined by MCMC analysis, using the prior constraint that the *white* dwarf mass-radius relation has to match the Eggleton relation to within 5 % RMS

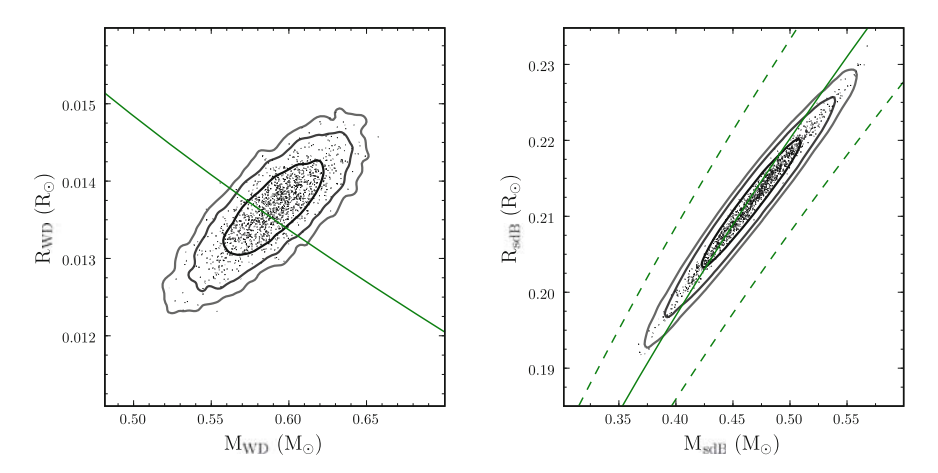


Fig. 4.5 Figure equivalent to Fig. 4.4 but for an MCMC run with a prior constraint that the *white* dwarf mass-radius relation has to match the Eggleton relation to within 5 % RMS

**Table 4.3** Correlation coefficients of the different parameters that were varied in the MCMC simulations, after applying the Eggleton mass-radius relation constraint

	11110000				
	$R_2$	i	$T_1$	$T_2$	q
$R_1$	0.95	-0.95	0.02	0.02	-0.95
$R_2$		-0.98	0.07	0.02	-0.99
i			-0.06	-0.02	0.96
$T_1$				0.44	-0.09
$T_2$					-0.02

Sect. 4.4. The correlation coefficients between the different parameters are given in Table 4.3. The binary's inclination, its mass ratio and the stellar radii are highly correlated.

	Frequency $(d^{-1})$	Amplitude	S/N	
		(µmag)		
$f_1$	$0.2758 \pm 0.0011$	$97.5 \pm 7.2$	13.5	
$f_2$	$0.5936 \pm 0.0013$	$97.5 \pm 7.2$	13.5	Instrumental
$\overline{f_3}$	$0.1417 \pm 0.0014$	$86.6 \pm 7.2$	12.1	$= f_2/4$
$\overline{f_4}$	$1.1820 \pm 0.0015$	$81.0 \pm 7.2$	11.3	$=2f_{2}$
$f_5$	$1.7730 \pm 0.0018$	$67.5 \pm 7.2$	9.4	$=3f_2$
$\overline{f_6}$	$440.4386 \pm 0.0022$	$54.2 \pm 7.2$	7.6	Instrumental
$\overline{f_7}$	$4.9548 \pm 0.0024$	$49.1 \pm 7.2$	6.9	$=2f_{orb}$
$f_8$	$0.3115 \pm 0.0027$	$44.9 \pm 7.2$	6.3	

Table 4.4 Significant variability frequencies in the residuals of the light curve of KPD 1946+4340

The signal to noise (S/N) value was determined by dividing the amplitude of the peak by the uncertainty on the amplitude

#### 4.3.5 Variability in Residuals

One of the goals of the *Kepler Mission* is to allow detailed asteroseismic studies of pulsating stars. The asteroseismology programme is discussed in Gilliland et al. (2010). For more information about the search for pulsations in compact objects with *Kepler*, see Østensen et al. (2010).

The Fourier transform of the original light curve of an eclipsing close binary like KPD 1946+4340 is highly contaminated by frequencies and their harmonics due to the binary orbit. Subtraction of a good model of the binary signatures of the light curve allows one to get rid of this contamination. Since a number of sdBs have been found to be multiperiodically pulsating (for a review on asteroseismology of EHB stars, see Østensen 2009), we checked the residuals of the light curve for signs of pulsations. Using the analysis method and significance criteria outlined in Degroote et al. (2009), 8 significant frequencies were found, which are listed in Table 4.4.

The frequency  $f_2$  is a known artefact frequency caused by an eclipsing binary that was used as one of the fine-guidance stars during Q1 (see Haas et al. 2010; Jenkins et al. 2010). Three other frequencies ( $f_3$ ,  $f_4$  and  $f_5$ ) are related to  $f_2$ . The highest frequency,  $f_6$ , is related to the processing of the long cadence data (see Gilliland et al. 2010), while  $f_7$  is the first harmonic of the orbital frequency of KPD 1946+4340, which indicates that there is still a weak orbital component left after subtracting our light curve model.  $f_1$  and  $f_8$  are not related to any of the other frequencies and corresponds to periods that are too long to arise from stellar pulsations of the WD or the sdB. If these signals are not instrumental, they might result from the rotation of the WD, or they might be due to a background star.

The best candidate peak for p-mode pulsations of the sdB is at 5018.2  $\mu$ Hz with an amplitude of 37  $\mu$ mag. From ground based data, Østensen et al. (2010) did not detect pulsations, with a limit of 0.68 mmag. This is consistent with the *Kepler* photometry.

### 4.4 Spectroscopic Analysis

Low resolution high S/N spectra for KPD 1946+4340 were taken with the B&C spectrograph at Steward Observatory's 2.3 m Bok telescope on Kitt Peak, as part of a long term homogeneous survey of hot subdwarf stars (Green et al. 2008), in September and October 2004. The properties of the data and reduction is discussed in Bloemen et al. (2011) to which we refer for details.

The reduced KPD 1946+4340 spectrum was fitted using two separate grids of NLTE models designed for sdB stars, in order to derive the effective temperature, surface gravity and He/H ratio. The first set of models assumed zero metals, while the second included an adopted distribution of metals based on the analysis of FUSE spectra of five sdB stars by Blanchette et al. (2008), see also Van Grootel et al. (2010). From the set of models without metals, we derive  $\log g = 5.45 \pm 0.04$ ,  $T_{\rm eff} = 34,400 \pm 220$  K and  $\log({\rm He/H}) = -1.37 \pm 0.05$ . Assuming the Blanchette composition, we find  $\log g = 5.43 \pm 0.04$ ,  $T_{\rm eff} = 34,730 \pm 250$  K and  $\log({\rm He/H}) = -1.36 \pm 0.04$ . These results are in good agreement with  $\log g = 5.37 \pm 0.10$ ,  $T_{\rm eff} = 34,500 \pm 1,000$  K,  $\log({\rm He/H}) = -1.35 \pm 0.10$  determined by Morales-Rueda et al. (2003) and  $\log g = 5.43 \pm 0.10$ ,  $T_{\rm eff} = 34,200 \pm 500$  K determined by Geier et al. (2010) using different spectra and model grids.

The fit definitely improves when going from the zero-metal solution (Fig. 4.6) to the Blanchette composition (Fig. 4.7), although there still remains a slight "Balmer"

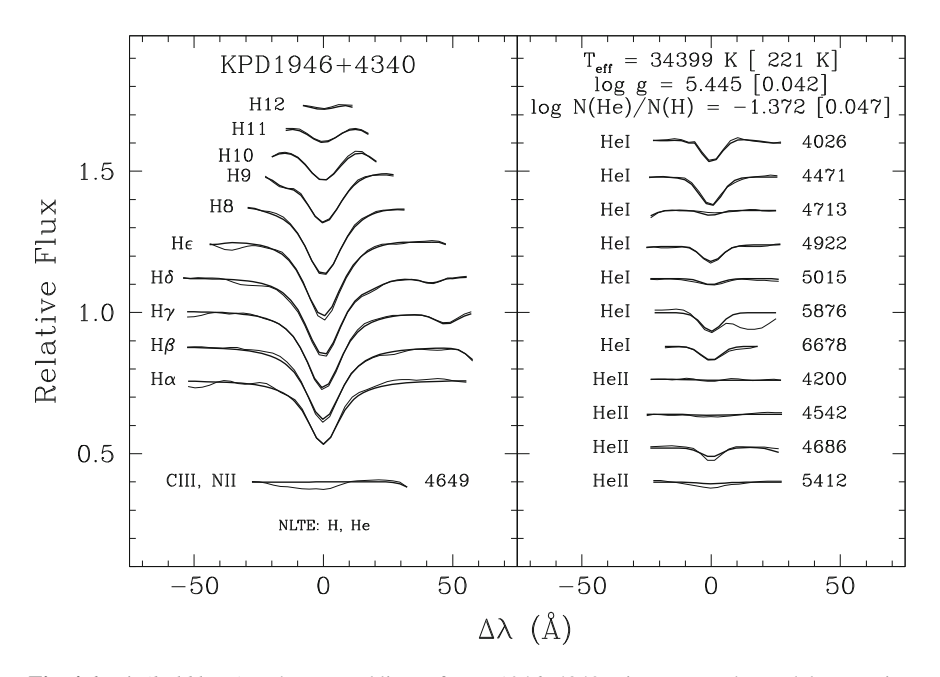


**Fig. 4.6** Fit (*bold lines*) to the spectral lines of KPD 1946+4340 using NLTE sdB models assuming zero metals

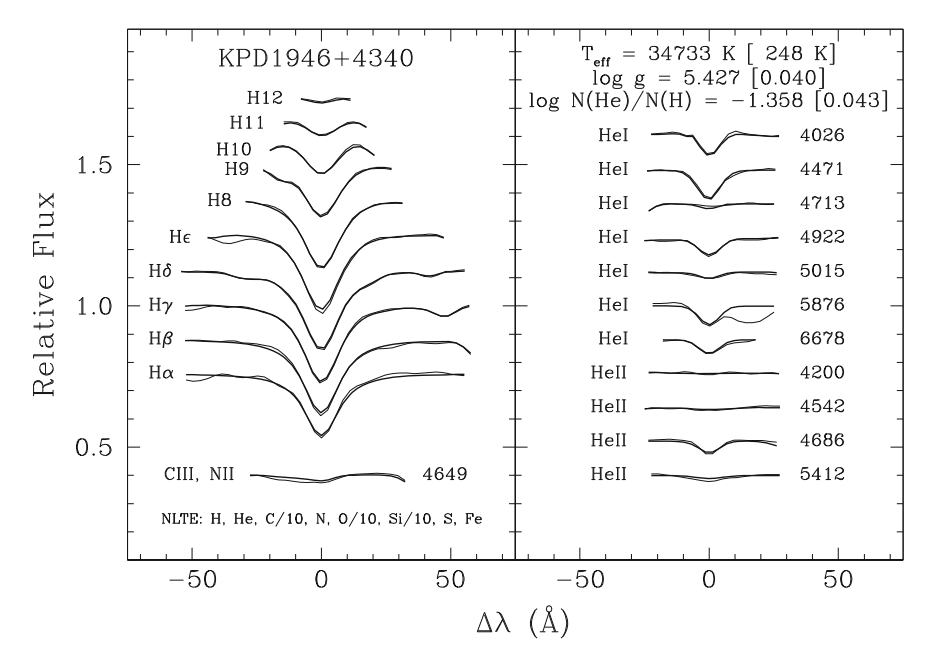


**Fig. 4.7** Fit (*bold lines*) to the spectral lines of KPD 1946+4340 using NLTE sdB models assuming a Blanchette metal composition

problem, especially noticeable in the core of  $H\beta$ . There are definitely metals in the spectrum of KPD 1946+4340: the strongest features are (1) an unresolved C III + N II complex around 4,649 Å (compare the two figures for that feature), and (2) another weaker complex (C III + O II) in the blue wing of  $H\delta$  that the Blanchette model reproduces quite well. All of the major discrepancies between the spectra and the models are due to strong interstellar absorption: the K line of Ca II in the blue wing of  $H\epsilon$ , the Ca II H line in the core of  $H\epsilon$ , and the Na I doublet strongly affecting the red wing of He I 5876. It is reassuring that the derived atmospheric parameters are not too strongly dependent on the presence of metals, as might be expected for such a hot star, particularly one in which downwards diffusion of metals is important.

#### 4.5 Discussion

The beaming factor we derived for KPD 1946+4340 using MCMC runs is  $\langle B \rangle = 1.33 \pm 0.02$ , which is in perfect agreement with the theoretically expected value calculated in Sect. 4.3.2. The uncertainty on the beaming factor is a direct reflection of the uncertainty on the spectroscopic radial velocity amplitude of the sdB. If, contrary to our assumption, the *Kepler* fluxes would be severely contaminated by light from other (constant) stars, the observed beaming factor would be lower. The

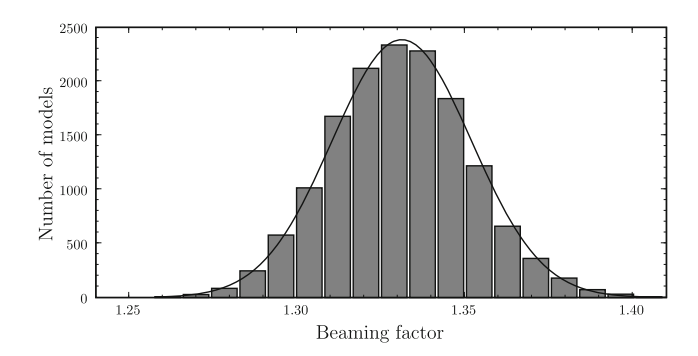


**Fig. 4.8** Distribution of the sdB's beaming factor for an MCMC run (using the M-R constraint for the WD; see text for details). The beaming factor is found to be  $\langle B \rangle = 1.33 \pm 0.02$ , which is in agreement with the theoretically expected  $\langle B \rangle = 1.30 \pm 0.03$ 

distribution of beaming factors from our MCMC computations is shown in Fig. 4.8. If the radial velocity would be measured from the Doppler beaming amplitude, using the theoretical beaming factor, the result would be  $168 \pm 4\,\mathrm{km\,s^{-1}}$  compared to  $164.0 \pm 1.9\,\mathrm{km\,s^{-1}}$  derived from spectroscopy. The uncertainty on the photometric radial velocity is dominated by the uncertainty on the theoretical beaming factor, primarily due to its dependence on the poorly known metallicity of the sdB, and to a lesser extent due to the uncertainties on the sdB's effective temperature and surface gravity.

Under the assumption of corotation, we find a projected rotational velocity of the sdB of  $v \sin i = 26.6 \pm 0.8 \,\mathrm{km \, s^{-1}}$ . From spectroscopy and using LTE models with ten times Solar metallicity, Geier et al. (2010) found  $v \sin i = 26.0 \pm 1.0 \,\mathrm{km \, s^{-1}}$ , which is in agreement with our photometric result. We conclude that the assumption of corotation is likely to be correct. Using the Zahn (1975) theory of tidal interaction we can determine the synchronization timescale for stars with a radiative envelope. Following methods outlined in Pablo (2012), we found a synchronization timescale of  $2.6 \times 10^9$  yr. This would mean that the star did not have time yet to reach a corotation state, but Goldreich and Nicholson (1989) suggested that stars tend to synchronize from the outside to the inside of the star. This would mean that the outer layers that are observed in spectroscopic measurements can be in corotation much earlier.

The spectroscopically determined surface gravity of the sdB (log  $g=5.43\pm0.04$  and  $5.45\pm0.04$  using atmosphere models with and without metals respectively) agrees perfectly with the surface gravity of  $5.452\pm0.006$  we derived from the mass-radius distribution of our light curve models.

As concluded earlier by Morales-Rueda et al. (2003), the sdB is probably in a post-EHB phase. This is illustrated in Fig. 4.9, which shows the zero age extended horizontal branch (ZAEHB) and the terminal age extended horizontal branch (TAEHB) for an sdB with a typical core mass of  $0.47\,\mathrm{M}_\odot$ , together with evolutionary tracks for

4.5 Discussion 59

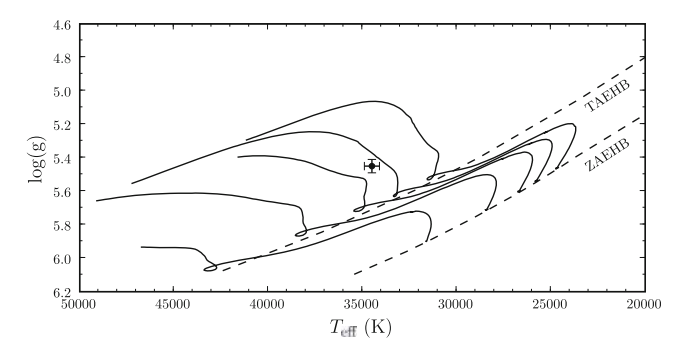


Fig. 4.9 The sdB of KPD 1946+4340 in the  $T_{\rm eff}$  –  $\log g$  plane. The theoretical zero age and terminal age extended *horizontal* branches for a 0.47  $\rm M_{\odot}$  are shown, together with evolutionary tracks for different envelope thicknesses ( $10^{-4}$ ,  $10^{-3}$ ,  $2 \times 10^{-3}$ ,  $3 \times 10^{-3}$  and  $4 \times 10^{-3}$   $\rm M_{\odot}$ ). The sdB is found to be in the post-EHB phase

different hydrogen envelope masses ( $10^{-4}$ ,  $10^{-3}$ ,  $2 \times 10^{-3}$ ,  $3 \times 10^{-3}$  and  $4 \times 10^{-3}$  M $_{\odot}$ ) from Kawaler and Hostler (2005).

Because of its low surface gravity, the sdB component of KPD 1946+4340 falls in a region of the  $T_{\rm eff}$  – log g plane relatively far from the center of the instability strip. However, at least one pulsator exists in this region of the  $T_{\rm eff}$  – log g plane, V338 Ser, that should be in a post-EHB phase (see Østensen 2009, Fig. 3). Moreover, 'transient pulsators' with varying pulsation amplitudes that can go down to undetectable values in a particular epoch might exist (see the case of KIC 2991276 in Østensen et al. 2010). For these reasons, and because we found at least one candidate p—mode pulsation frequency, it is worth continuing a photometric monitoring by *Kepler*.

The white dwarf mass implies that it is a CO white dwarf. The progenitor of the sdB must have been the less massive star in the original binary and by the time it reached the ZAEHB, the white dwarf was already cooling. The accretion of material by the white dwarf does not change the WD's internal energy content significantly (see e.g. related work on cataclysmic variables by Townsley and Bildsten 2002). The cooling time of the white dwarf therefore sets an upper limit to the time since the sdB was on the ZAEHB. For our best estimates of the temperature and mass of the white dwarf, the cooling tracks of Holberg and Bergeron (2006) indicate that it has been cooling for about 155–170 Myr (depending on the unknown envelope composition). The sdB's evolution from the Zero Age Extended Horizontal Branch to its current post-EHB-phase took 125–145 Myr (Kawaler and Hostler 2005, depending on the exact current evolutionary stage), which means that the sdB must have formed very shortly after the white dwarf.

#### 4.6 Summary

We have analysed a 33.5 d short cadence *Kepler* light curve of KPD 1946+4340, as well as low resolution spectroscopy. In the light curve, primary and seconday eclipses, ellipsoidal modulation and Doppler beaming are detected. We model the binary light curve, taking into account the Doppler beaming and gravitational lensing effects. System parameters and uncertainties are determined using Markov Chain Monte Carlo simulations.

The binary is found to consist of a  $0.59 \pm 0.02\,M_\odot$  white dwarf and a  $0.47 \pm 0.03\,M_\odot$  post-EHB sdB star. The surface gravity and corotation rotational velocity of the sdB as derived from the light curve models are found to be consistent with spectroscopic values. The observed Doppler beaming amplitude is in perfect agreement with the amplitude expected from spectroscopic radial velocity measurements. It would thus have been possible to derive the radial velocity amplitude of the sdB from the *Kepler* light curve directly.

Subtracting a good light curve model allowed us to search for stellar pulsations. No significant stellar variability of the sdB or white dwarf could be detected. At least one candidate p-mode pulsation frequency was found, however, and the sdB can also possibly be a transient pulsator.

#### References

Agol, E. (2002). ApJ, 579, 430.

Agol, E. (2003). ApJ, 594, 449.

Allard, F., Wesemael, F., Fontaine, G., Bergeron, P., & Lamontagne, R. (1994). AJ, 107, 1565.

Blanchette, J., Chayer, P., Wesemael, F., Fontaine, G., Fontaine, M., Dupuis, J., et al. (2008). *ApJ*, 678, 1329.

Bloemen, S., Marsh, T. R., Østensen, R. H., et al. (2011). MNRAS, 410, 1787.

Cardelli, J. A., Clayton, G. C., & Mathis, J. S. (1989). ApJ, 345, 245.

Claret, A. (2004). A&A, 428, 1001.

Collier Cameron A., Wilson D. M., & West R. G., et al. (2007). MNRAS, 380, 1230.

Copperwheat, C. M., Marsh, T. R., Dhillon, V. S., Littlefair, S. P., Hickman, R., Gänsicke, B. T., et al. (2010). MNRAS, 402, 1824.

Degroote, P., Aerts, C., Ollivier, M., et al. (2009). A&A, 506, 471.

Downes, R. A. (1986). ApJS, 61, 569.

Gänsicke, B. T., Beuermann, K., & de Martino, D. (1995). A&A, 303, 127.

Geier S., Heber U., Podsiadlowski P., Edelmann H., Napiwotzki R., & Kupfer, T., et al. (2010). ArXiv:1005.4785.

Gilliland, R. L., Jenkins, J. M., Borucki, W. J., et al. (2010). ApJ, 713, L160.

Gilliland, R. L., Brown, T. M., Christensen-Dalsgaard, J., et al. (2010). PASP, 122, 131.

Goldreich, P., & Nicholson, P. D. (1989). ApJ, 342, 1079.

Gould, A. (1995). ApJ, 446, 541.

Green, E. M., Fontaine, G., Hyde, E. A., For, B., & Chayer, P. (2008). ASPC, 392, 75.

Haas, M. R., Batalha, N. M., Bryson, S. T., et al. (2010). ApJ, 713, L115.

Han, Z., Podsiadlowski, P., Maxted, P. F. L., Marsh, T. R., & Ivanova, N. (2002). MNRAS, 336, 449.

Han, Z., Podsiadlowski, P., Maxted, P. F. L., & Marsh, T. R. (2003). MNRAS, 341, 669.

References 61

Heber, U. (1986). A&A, 155, 33.

Heber, U., Reid, I. N., & Werner, K. (2000). A&A, 363, 198.

Heber, U. (2009). ARA&A, 47, 211.

Hills, J. G., & Dale, T. M. (1974). A&A, 30, 135.

Holberg, J. B., & Bergeron, P. (2006). AJ, 132, 1221.

Hu, H., Nelemans, G., Østensen, R., Aerts, C., Vučković, M., & Groot, P. J. (2007). A&A, 473, 569.

Jenkins, J. M., Caldwell, D. A., Chandrasekaran, H., et al. (2010). ApJ, 713, L120.

Kawaler, S. D., & Hostler, S. R. (2005). ApJ, 621, 432.

van Kerkwijk, M. H., Rappaport, S. A., Breton, R. P., Justham, S., Podsiadlowski, P., & Han, Z. (2010). *ApJ*, 715, 51.

Koch, D. G., Borucki, W. J., Basri, G., et al. (2010). ApJ, 713, L79.

de Kool, M. (1990). ApJ, 358, 189.

Lemke, M. (1997). A&AS, 122, 285.

Loeb, A., & Gaudi, B. S. (2003). ApJ, 588, L117.

Maeder, A. (1973). A&A, 26, 215.

Marsh, T. R. (2001). MNRAS, 324, 547.

Maxted, P. F. L., Marsh, T. R., & North, R. C. (2000). MNRAS, 317, L41.

Morales-Rueda, L., Maxted, P. F. L., Marsh, T. R., North, R. C., & Heber, U. (2003). MNRAS, 338, 752.

Østensen R. H., Oreiro R., Solheim J., Heber U., Silvotti R., González-Pérez J. M., Ulla A., Pérez Hernández F., Rodríguez-López C., & Telting J. H. (2010). *A&A*, *513*, A6.

Østensen, R. H. (2009). Communications in Asteroseismology, 159, 75.

Østensen, R. H., Silvotti, R., Charpinet, S., et al. (2010). MNRAS, 409, 1470.

Pablo, H. (2012). PhD thesis, Iowa State University.

Saffer, R. A., Bergeron, P., Koester, D., & Liebert, J. (1994). ApJ, 432, 351.

Sahu, K. C., & Gilliland, R. L. (2003). ApJ, 584, 1042.

Shakura, N. I., & Postnov, K. A. (1987). A&A, 183, L21.

Townsley, D. M., & Bildsten, L. (2002). ApJ, 565, L35.

Van Grootel, V., Charpinet, S., Fontaine, G., Brassard, P., Green, E. M., Randall, S. K., et al. (2010). ApJ, 718, L97.

Verbunt, F., & Rappaport, S. (1988). ApJ, 332, 193.

von Zeipel, H. (1924). MNRAS, 84, 665.

Wesemael, F., Fontaine, G., Bergeron, P., Lamontagne, R., & Green, R. F. (1992). *AJ*, 104, 203.

Zahn, J.-P. (1975). A&A, 41, 329.

Zucker, S., Mazeh, T., & Alexander, T. (2007). ApJ, 670, 1326.

# Chapter 5 Mass Ratio from Doppler Beaming and Rømer Delay Versus Ellipsoidal Modulation in the *Kepler* Data of KOI-74

**Abstract** We present a light curve analysis and radial velocity study of KOI-74, an eclipsing A star + white dwarf binary with a 5.2 day orbit. Aside from new spectroscopy covering the orbit of the system, we used 212 days of publicly available Kepler observations and present the first complete light curve fitting to these data, modelling the eclipses and transits, ellipsoidal modulation, reflection, and Doppler beaming. Markov Chain Monte Carlo simulations are used to determine the system parameters and uncertainty estimates. Our results are in agreement with earlier studies, except that we find an inclination of  $87.0\pm0.4^{\circ}$ , which is significantly lower than the previously published value. The altered inclination leads to different values for the relative radii of the two stars and therefore also the mass ratio deduced from the ellipsoidal modulations seen in this system. We find that the mass ratio derived from the radial velocity amplitude ( $q = 0.104 \pm 0.004$ ) disagrees with that derived from the ellipsoidal modulation ( $q = 0.052 \pm 0.004$  assuming corotation). This mismatch was found before, but with our smaller inclination, the discrepancy is even larger than previously reported. Accounting for the rapid rotation of the A-star, instead of assuming corotation with the binary orbit, is found to increase the discrepancy even further by lowering the mass ratio to  $q = 0.047 \pm 0.004$ . These results indicate that one has to be extremely careful in using the amplitude of an ellipsoidal modulation signal in a close binary to determine the mass ratio, when a proof of corotation is not firmly established. The same problem could arise whenever an ellipsoidal modulation amplitude is used to derive the mass of a planet orbiting a host star that is not in corotation with the planet's orbit. The radial velocities that can be inferred from the detected Doppler beaming in the light curve are found to be in agreement with our spectroscopic radial velocity determination. We also report the first measurement of Rømer delay in a light curve of a compact binary. This delay amounts to  $-56 \pm 17$  s and is consistent with the mass ratio derived from the radial velocity amplitude. The firm establishment of this mass ratio at  $q = 0.104 \pm 0.004$  leaves little doubt that the companion of KOI-74 is a low mass white dwarf.

This chapter is based on

S. Bloemen, T. R. Marsh, P. Degroote, R. H. Østensen, P. I. Pápics, C. Aerts, D. Koester, B. T. Gänsicke, E. Breedt, R. Lombaert, S. Pyrzas, C. M. Copperwheat, K. Exter, G. Raskin, H. Van Winckel, S. Prins, W. Pessemier, Y. Frémat, H. Hensberge, A. Jorissen, S. Van Eck Monthly Notices of the Royal Astronomical Society, 2012, vol. 422, pp. 2600–2608.

#### 5.1 Kepler Object-of-Interest 74

The primary science goal of the *Kepler* Mission is the detection of Earth-like exoplanets, but its highly accurate photometric observations also reveal hundreds of eclipsing binary stars (Slawson et al. 2011) and are well suited for the study of stellar variability at unprecedentedly low amplitudes (Debosscher et al. 2011). In this chapter, we present an analysis of 212 d of *Kepler* data of the eclipsing binary KOI-74 (KIC 6889235), and spectra taken at different orbital phases.

The system consists of a main-sequence A star primary and a less massive companion. Its light curve shows deeper eclipses than transits, which implies that the companion is hotter than the primary. There is a clear asymmetric ellipsoidal modulation pattern in which the flux maximum after the transits is larger than the maximum after the eclipses. Rowe et al. (2010) suggested that the asymmetry in the ellipsoidal modulation be due to a star spot. Van Kerkwijk et al. (2010) instead attributed it to Doppler beaming. Its expected detection in Kepler light curves was suggested and discussed by Loeb and Gaudi (2003) and Zucker et al. (2007). The detection of Doppler beaming in Kepler light curves has led to the discovery of several noneclipsing short-period binary systems (Faigler et al. 2012) and it has been shown that it can also be observed in planetary systems (see e.g. Mazeh and Faigler 2010; Shporer et al. 2011). In Chap. 4 we detected Doppler beaming in the Kepler light curve of KPD 1946+4340 and presented the first comparison between a radial velocity amplitude derived from Doppler beaming with a spectroscopic value. In the case of KPD 1946+4340, the results were found to be consistent. For KOI-74, spectroscopic radial velocity measurements were recently presented by Ehrenreich et al. (2011). In this chapter, we present independent spectroscopic radial velocity measurements which we compare with the photometric radial velocity amplitude prediction.

Earlier analyses of the *Kepler* light curve of KOI-74 are presented in Rowe et al. (2010) and Van Kerkwijk et al. (2010). Rowe et al. (2010) measured the mass ratio of the system from the amplitude of the ellipsoidal modulation and found a companion mass of  $0.02-0.11\,M_\odot$ . Van Kerkwijk et al. (2010) built on these results (e.g. they used the inclination value reported by Rowe et al. 2010) but claimed that the mass ratio of the system could not be determined reliably from the ellipsoidal modulation amplitude. Instead, they used the radial velocity information from the Doppler beaming signal to derive a companion mass of  $0.22\pm0.03\,M_\odot$ . They concluded that the companion has to be a low mass white dwarf and showed that the system properties are in good agreement with a binary that has undergone a phase of stable Roche lobe overflow from the more massive star to the less massive star. This puts KOI-74 in an evolutionary stage that follows on that of systems such as WASP J0247-2515, which Maxted et al. (2011) recently identified as a binary consisting of an A-star and a red giant core stripped from its envelope. Up to now, 4 close binaries consisting of a white dwarf and a main sequence star of spectral type A or F have been found in

<sup>&</sup>lt;sup>1</sup> We use the terms 'transit' and 'eclipse' to indicate, respectively, the occultation of the A-star by the compact object and the occultation of the compact object by the A-star half an orbit later.

*Kepler* data (Rowe et al. 2010; Van Kerkwijk et al. 2010; Carter et al. 2011; Breton et al. 2012).

We remodel the *Kepler* light curve of KOI-74, adding an additional 175d of data compared to the previous studies and perform Markov Chain Monte Carlo (MCMC) simulations to explore the uncertainty on the derived system parameters. We will revisit the issue of the true mass ratio of the system, using input from the light curve analysis (Doppler beaming, ellipsoidal modulation and Rømer delay) and spectroscopy.

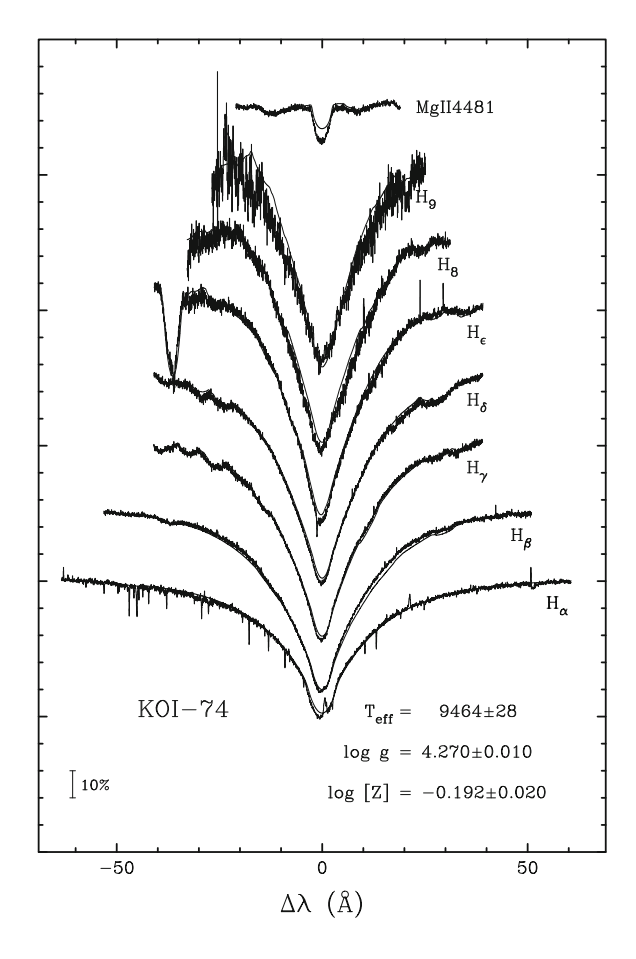
#### 5.2 Spectroscopy

To determine the spectral type, the rotational velocity and the radial velocity amplitude of the primary, we obtained 46 high resolution ( $R \sim 85,000$ ) échelle spectra using the HERMES spectrograph (Raskin et al. 2011) at the 1.2-m Mercator telescope (La Palma, Canary Islands). Additionally, we obtained 29 spectra with the ISIS spectrograph mounted on the 4.2-m William Herschel Telescope (La Palma, Canary Islands). The details of their reduction are provided in Bloemen et al. (2012).

From the average HERMES spectrum, we measured the rotational velocity of the primary  $v \sin i = 164 \pm 9 \,\mathrm{km \, s^{-1}}$ , using the Fourier method presented in Gray (1992), from the Mg II  $\lambda$ 4481 line. Compared to other techniques such as fitting broadened synthetic spectra, the Fourier method has the advantage of being rather unsensitive to other line broadening mechanisms (see e.g. Simón-Díaz and Herrero 2007). The Mg II λ4481 line is a doublet with components at 4.481.126 and 4.481.325 Å, which leads to an overestimation of  $v \sin i$  (see e.g. Royer et al. 2002). By applying the same method to a synthetic spectrum with a comparable rotational broadening, we find that we can expect our  $v \sin i$  measurement to be overestimated by about  $10 \,\mathrm{km} \,\mathrm{s}^{-1}$  due to the double nature of the line. Given this overestimation, our result is in line with the values mentioned in the *Note in proof* of Van Kerkwijk et al. (2010), 150 km s<sup>-1</sup>, and in Ehrenreich et al. (2011),  $145 \pm 5 \,\mathrm{km}\,\mathrm{s}^{-1}$ . If the primary were in corotation with the binary orbit, we would expect  $v \sin i \sim 25 \,\mathrm{km \, s^{-1}}$ . The rotational velocity measured from spectroscopy thus implies that the primary is not in corotation but is instead a fast rotator. We have adopted  $v \sin i = 150 \pm 10 \,\mathrm{km \, s^{-1}}$  for the analysis presented in this chapter.

We also performed a spectral fit to the Balmer lines and Mg II  $\lambda 4481$  using the solar metallicity synthetic spectra of Munari et al. (2005) and assuming a rotational velocity of  $150 \, \mathrm{km \, s^{-1}}$ . The fits to the spectral lines are shown in Fig. 5.1. The small emission feature in the core of the H $\alpha$  and H $\beta$  lines does not originate from any of the two binary components but is caused by sky emission (see also Ehrenreich et al. 2011). It is absent in the ISIS spectra, for which we could perform a background subtraction during the data reduction. We find that the primary has a gravity of  $\log g \sim 4.27$  and an effective temperature of  $T_{\mathrm{eff}} \sim 9,500 \, \mathrm{K}$ . These results are in agreement with the spectral type A1V and  $T_{\mathrm{eff}} = 9,400 \pm 150 \, \mathrm{K}$  derived by

Fig. 5.1 Fit to the spectral lines of KOI-74 using the average HERMES spectrum (after shifting the spectra to the rest frame of the primary) and the solar metallicity synthetic spectra of Munari et al. (2005). The uncertainties on the parameters indicated on the figure only reflect the formal errors on the fit



Rowe et al. (2010), from which they inferred a primary mass of  $M_1 = 2.2 \pm 0.2 \, \mathrm{M}_{\odot}$ . We adopted  $T_{\rm eff} = 9,500 \pm 250 \, \mathrm{K}$  for our analysis.

We have used two techniques to derive the radial velocity amplitude of the A-star. The only metal line that is clearly detected in both the HERMES and ISIS spectra, is the Mg II line at 4,481 Å. We measured the radial velocities from that line by fitting a Gaussian profile to it. We also measured the radial velocities from the Balmer lines at 4,102, 4,340 and 4,861 Å simultaneously, by first normalising the spectra using low order splines (as described in Pápics et al. 2012), and then fitting a Gaussian to the core of the mean profile obtained by Least Squares Deconvolution (Donati et al. 1997). The measured radial velocity amplitudes and systemic velocities, assuming a circular orbit, are given in Table 5.1. The uncertainties on individual data points have been scaled to deliver a unit  $\chi^2$  per degree of freedom. The initial  $\chi^2$ , before rescaling the uncertainties, is given in the table.

The radial velocities measured from the Balmer lines are shown in Fig. 5.2, folded on the orbital period using the *Kepler* ephemeris as given in Rowe et al. (2010). Some

5.2 Spectroscopy 67

1313@WHI allo	I LEKMES@M	ercator spectra		
Instrument	Line(s)	$K_1  ({\rm km  s^{-1}})$	$\gamma  (\mathrm{km  s^{-1}})$	$\chi^2_{\text{init,reduced}}$
ISIS	Balmer	$15.8 \pm 0.4$	$-50.9 \pm 0.3$	1.2
	Mg II	$15.4 \pm 0.7$	$-49.3 \pm 0.5$	1.6
HERMES	Balmer	$14.9 \pm 0.4$	$-47.1 \pm 0.3$	0.5
	Mg II	$16.5 \pm 1.3$	$-51.0 \pm 1.0$	2.3
Weighted mean (adopted)		$15.4 \pm 0.3$	$-49.1 \pm 0.2$	

**Table 5.1** Radial velocity amplitudes ( $K_1$ ) and systemic velocities ( $\gamma$ ) of KOI-74, measured from ISIS@WHT and HERMES@Mercator spectra

The uncertainties that are given are scaled to get a unit  $\chi^2$  per degree of freedom. The initial reduced  $\chi^2$  is given in the last column. Two techniques have been used: a Gaussian fit to the Mg II line at 4,481 Å and a Gaussian fit to the mean profile of the Balmer lines at 4,102, 4,340 and 4,861 Å (see text for details)

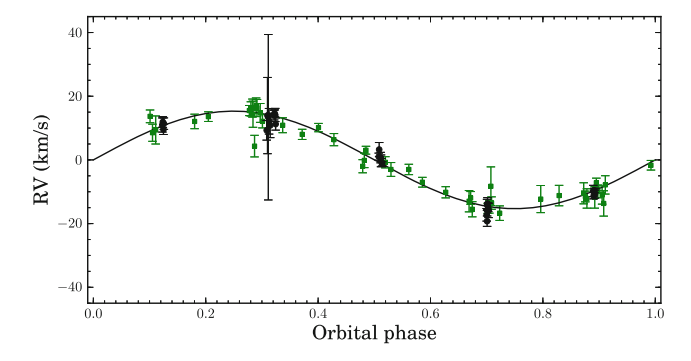


Fig. 5.2 Radial velocity curve of the primary of KOI-74, measured by fitting a Gaussian profile to the mean profile of three Balmer lines (see text for details). The radial velocity measurements from ISIS@WHT spectra are represented by *black circles*, the measurements from HERMES@Mercator spectra by *green squares*, folded on the orbital period. The systemic velocity derived from both datasets has been subtracted. The error bars are scaled to deliver a unit  $\chi^2$  per degree of freedom

spectra were taken in bad seeing conditions, which is reflected by the large error bars on a few of the data points. We have adopted the weighted mean velocity amplitude of our measurements,  $K_1 = 15.4 \pm 0.3 \, \mathrm{km \, s^{-1}}$ , for the further analysis presented in this chapter. The weighted mean systemic velocity, is  $\gamma = 49.1 \pm 0.2 \, \mathrm{km \, s^{-1}}$ . Our radial velocity amplitudes are in agreement with (but slightly lower than) Ehrenreich et al. (2011)'s result of  $18.2 \pm 1.7 \, \mathrm{km \, s^{-1}}$ .

#### **5.3** *Kepler* Photometry

The *Kepler* data from Q0 (quarter 0), Q1, Q2 and Q3 were retrieved from the public archive.<sup>2</sup> The data span 229 d, resulting in a dataset of 212 d of observations excluding the gaps. The data of Q0, Q1 and the first two months of Q2 are long cadence data

<sup>&</sup>lt;sup>2</sup> Publicly released *Kepler* data can be downloaded from http://archive.stsci.edu/kepler/.

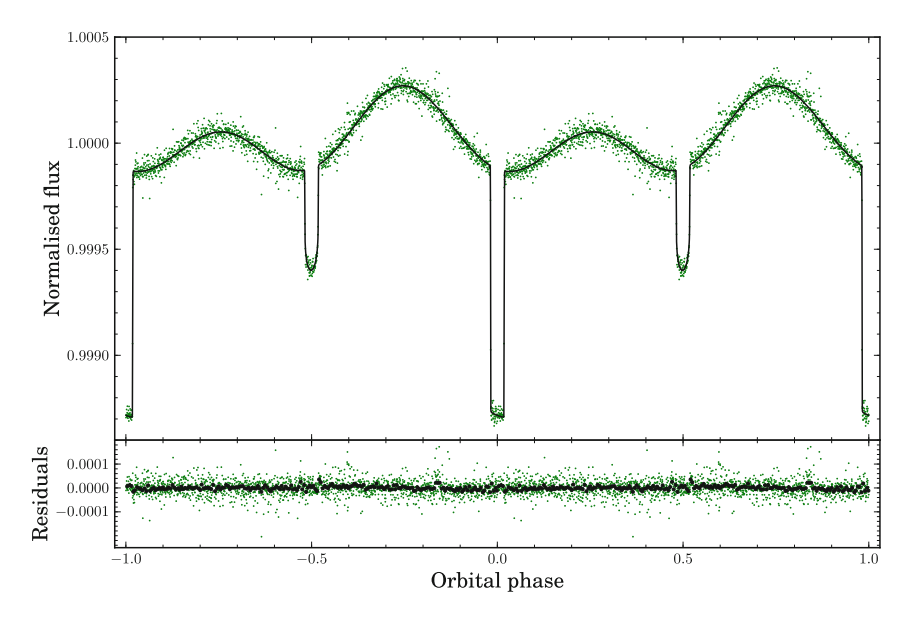


**Fig. 5.3** The *Kepler* Q0, Q1, Q2 and Q3 data of KOI-74, folded on the orbital period and binned into 2,000 phase bins. The *black curve* shows a typical model fit to the data. The residuals of the data points after subtracting the model are shown in the *bottom panel*, binned into 2,000 phase bins (*green*) and 200 phase bins (*black*)

(30 m integrations), the last 27 d of Q2 and the entire Q3 dataset (86 d) are taken in short cadence mode (1 m integrations). The light curve (see Fig. 5.3 for a phase folded version) shows clear eclipses, transits, ellipsoidal modulation and Doppler beaming. Rowe et al. (2010) and Van Kerkwijk et al. (2010) already presented models for the light curve. We remodelled the light curve using more data, and find a lower orbital inclination than Rowe et al. (2010) ( $i = 88.8 \pm 0.5^{\circ}$ ). This finding also has consequences for some of the system parameters derived by Van Kerkwijk et al. (2010), as they adopted the inclination of Rowe et al. (2010) for their analysis.

Below we discuss the various steps of our binary light curve modelling, referring to Bloemen et al. (2012) for details on the extraction and detrending of the *Kepler* data. We rebinned the light curve into 1,800 s bins out of eclipse and 30 s bins in eclipse, to be left with 1,717 data points. In the following, we assumed that there is no background contamination in the *Kepler* data.

#### 5.3.1 What We Can Learn from the Kepler Light Curve

As already discussed in Chap. 4, fitting a light curve of a binary that shows a variety of effects (such as eclipses, ellipsoidal modulation and Doppler beaming) allows one to gain a lot of information on the binary's parameters. We first recall the potential in the case of KOI-74 before we discuss the actual light curve fits in Sect. 5.3.3.

A first useful constraint comes from the measured fractional transit depth, which reveals the ratio of the radii of the two stars:

$$\Delta F_{transit}/F = (R_2/R_1)^2. \tag{5.1}$$

Given  $R_2/R_1$  from the transit depth and  $T_1$  from the spectral fit (Sect. 5.2), the eclipse depth provides information about  $T_2$ . Using blackbody approximations and neglecting the contribution of the companion out of eclipse, one finds:

$$\frac{\Delta F_{eclipse}}{F} \approx \frac{F_2}{F_1} = \frac{\exp(h\nu/kT_1) - 1}{\exp(h\nu/kT_2) - 1} \left(\frac{R_2}{R_1}\right)^2. \tag{5.2}$$

The eclipse duration  $t_e$  gives  $R_1/a$  as a function of the inclination i (assuming spherical stars):

$$(R_1/a)^2 = \sin^2(\pi t_e/P) \sin^2 i + \cos^2 i$$
 (5.3)

(Russell 1912) with P the orbital period and a the separation between the two binary components.

In case of *corotation* of the star with the binary orbit, the semi-amplitude of the ellipsoidal modulation can be approximated as<sup>3</sup>

$$\frac{\Delta F_{ellipsoidal}}{F} = 0.15 \frac{(15 + u_1)(1 + \tau_1)}{3 - u_1} \left(\frac{R_1}{a}\right)^3 q \sin^2 i$$
 (5.4)

(Morris and Naftilan 1993; Zucker et al. 2007) in which  $q = M_2/M_1$  is the mass ratio of the two binary components,  $u_1$  the primary's linear limb darkening coefficient and  $\tau_1$  its gravity darkening coefficient.

With  $R_1/a$  determined from the eclipse duration (Eq. 5.3), q is then known as a function of i. In the case of KOI-74, the primary is not in corotation but is a rapid rotator, as already suggested by Van Kerkwijk et al. (2010) and confirmed by all measurements of the rotational velocity (see Sect. 5.2). Van Kerkwijk et al. (2010) argue that rapid rotation has a very significant impact on the ellipsoidal modulation amplitude. Kruszewski (1963) presented an expression for the Roche lobe potentials that accounts for the effects of asynchronous rotation. Although we will use this treatment in our light curve models, we will be careful when interpreting the mass ratio derived from our light curve modelling effort presented in Sect. 5.3.3. Our modelling setup is such that the mass ratio is the only parameter that is only constrained by the ellipsoidal modulation amplitude. Therefore, if the expression for the ellipsoidal modulation is invalid (e.g. because it assumes instantaneous adjustment of the star's surface to the ever-changing potential in the asynchronous case), this will manifest itself in the mass ratio being off.

<sup>&</sup>lt;sup>3</sup> Van Kerkwijk et al. (2010) use a similar equation but with a  $\sin^3 i$  term, which should be  $\sin^2 i$ .

The detection of Doppler beaming in the extremely accurate *Kepler* light curve (see Van Kerkwijk et al. 2010) gives access to a second, independent, way to determine q as a function of i. For velocities much lower than the speed of light, the Doppler beaming amplitude is proportional to the radial velocity amplitude of the A-star as given by Eq. (4.2).

With  $M_1$  given by the spectral type derived from spectroscopy (Sect. 5.2), and  $K_1$  derived from the Doppler beaming amplitude (Eq. 4.2) or spectroscopy (Sect. 5.2), we get the following relation where q and i are the only unknowns:

$$K_1^3 = \frac{q^3}{(1+q)^2} \frac{2\pi G M_1}{P} \sin^3 i.$$
 (5.5)

This equation allows one to derive the mass ratio without relying on the amplitude of the ellipsoidal modulation (as long as the deformation of the primary is small enough not to affect the spectroscopic parameter determinations). The mass ratio q derived from the radial velocity amplitude using Eq. (5.5) is not influenced by the rapid rotation, contrary to the mass ratio that can be derived from the ellipsoidal modulation amplitude via Eq. (5.4).

Recently, Kaplan (2010) showed that one can use an effect similar to the Rømer delay to derive the radial velocity amplitude of the secondary, in double white dwarf binaries with circular orbits and mass ratios significantly different from 1. in such systems, a light travel time difference causes the time between the primary and secondary eclipses to be different from P/2 by

$$\delta t = (K_2 - K_1) \frac{P}{\pi c} \tag{5.6}$$

in which c denotes the speed of light (see Kaplan 2010). After substitution of  $q = \frac{K_1}{K_2}$ , we find the following expression:

$$q = \left(1 - \frac{\pi c \,\Delta t}{PK_1}\right)^{-1}.\tag{5.7}$$

If we can measure this Rømer delay, it would allow us to derive the mass ratio in yet another way, this time independently from the mass of the primary which was estimated from spectral analysis. As far as we are aware, this technique has not yet been applied to any system in practice. KOI-74 is a good candidate to put the theory to the test, since the expected time difference is of the order of a minute.

### 5.3.2 Gravity Darkening, Limb Darkening and Doppler Beaming Coefficients

The gravity darkening coefficient (see e.g. Claret 2003) of the primary was calculated by integrating ATLAS model spectra (Castelli and Kurucz 2004) over the *Kepler* 

bandpass. We took into account the estimated reddening of E(B-V) = 0.15 (Kepler Input Catalog) by reddening the model spectra following Cardelli et al. (1989). Reddening marginally influences the gravity darkening coefficient because it is bandpass dependent. Assuming solar metallicity,  $v_{\text{turb}} = 2 \, \text{km s}^{-1}$ ,  $T_{\text{eff}} = 9,500 \pm 250 \, \text{K}$  and  $\log g = 4.3 \pm 0.1$ , and using Eq. (4.1), we found the gravity darkening coefficient to be  $\beta_K = 0.55 \pm 0.05$ . We have used a physical gravity darkening coefficient of d log  $T/d \log g = 0.25$ .

Using the same assumptions, we computed limb darkening coefficients for the A-star. We adopted the 4-parameter limb darkening relation Eq. (5) of Claret (2004) with  $a_1 = 0.576$ ,  $a_2 = 0.118$ ,  $a_3 = -0.039$  and  $a_4 = -0.016$ . For the white dwarf companion, we used a model atmosphere for a DA white dwarf with  $T_{\rm eff} = 13,000$  K and  $\log g = 6.5$  (Koester 2010) and found  $a_1 = 0.372$ ,  $a_2 = 0.518$ ,  $a_3 = -0.540$  and  $a_4 = 0.178$ .

As explained in Sect. 4.3.2, a bandpass-integrated photon weighted beaming factor has to be computed for the A-star to model the Doppler beaming signal. Taking reddening into account, the beaming factor  $\langle B \rangle$  defined in Eq. (4.4) is found to be  $\langle B \rangle = 2.19 \pm 0.04$ , which compares well with Van Kerkwijk et al. (2010)'s value of 2.21. For an unreddened spectrum, the beaming factor would be  $\langle B \rangle = 2.22 \pm 0.04$ .

#### 5.3.3 Modelling Code and MCMC Setup

Our light curve modelling code, LCURVE (for a description of the code, see Copperwheat et al. 2010 Appendix A), uses grids of points on the two binary components to calculate the total flux that is visible from the system at different orbital phases. It accounts for Doppler beaming, eclipses and transits, ellipsoidal modulation and reflection effects. The code can also account for lensing effects (implemented following Marsh 2001), which occur when the white dwarf transits the primary. In the models of KOI-74 presented here, however, we did not include these lensing effects. The white dwarf radius we would find by including lensing would be slightly larger but we estimate the difference at about one percent only, which is far lower than the uncertainty on the parameter. In addition, estimation of the lensing requires knowledge of the mass of the white dwarf, which owing to the difficulty in deducing the mass ratio from the ellipsoidal variations, was not easily calculated during the MCMC runs.

A typical light curve fit is shown in Fig. 5.3, together with the phase folded light curve and the residuals. Because of the large difference in the radii of the stars, it turned out to be difficult to get the numerical noise at a lower level than the scatter on the observational datapoints of the superb *Kepler* light curve. The grid on the A-star would have to consist of millions of points to get to the required accuracy level, which is particularly difficult during the transits. We therefore replaced the grid of uniformly distributed points, at the transit phases, by a grid with a denser strip on the A-star at the region of the star that gets occulted during the white dwarf transits. A graphical representation of the grid is shown in Fig. 5.4. We used 92,716 points



**Fig. 5.4** Illustration of the grids of points we used on the two binary components to model the light curve of KOI-74 (only about one point in 4 is shown on the A-star, and about one in 10 on the white dwarf). To achieve a high enough numerical precision, at the transit phases, a denser strip is used on the primary at the location where it gets occulted by the white dwarf. The system is shown with an inclination of 86.4°, at orbital phase 0.02

(on 270 latitude strips) on the A-star outside the transits and 178,468 points during the transits (adding 7 latitude and 4 longitude points per coarse grid point in the strip). The flux from the white dwarf was modelled with a 12,724-points grid (100 latitude strips) at all orbital phases.

To account for a possible detection of the Rømer delay, we introduced a  $\delta t$  parameter and computed the light curve at phase  $\phi'$  instead of the requested phase  $\phi$ , with

$$\phi' = \phi + \frac{\delta t}{P} \left( \frac{\cos(2\pi\phi)}{2} - 0.5 \right). \tag{5.8}$$

This essentially results in a maximum Rømer delay of  $-\delta t$  at the phase of the eclipse, while the phase of the transit is untouched.

In an attempt to correctly model the ellipsoidal modulation taking into account the effects of rapid rotation, we implemented the adapted Roche lobe potentials as given by Kruszewski (1963). The modelling procedure, using Markov Chain Monte Carlo simulations, is identical to the one used in Sects. 4.3.3 and 4.3.4 for the modelling of the light curve of KPD 1946+4340. In the initial runs using the full dataset, the orbital period ( $P_{\rm orb}$ ), the time zero point ( $T_0$ ), the inclination (i), the temperature

of the white dwarf  $(T_2)$ , the mass ratio (q), the beaming factor  $(\langle B \rangle)$  and the Rømer delay  $(\delta t)$  were kept as free parameters. The computation of one synthetic light curve at the 28,086 time points of the dataset, for which we computed the light curve at about 127,000 phases to be able to account for the finite integration time of the observations, took about 5 min of CPU time. Due to the strong degeneracy between the inclination and the mass ratio, the MCMC chains took too much time to sample the whole parameter space. We therefore fixed the orbital period  $(P_{\rm orb})$  and the time zero point  $(T_0)$  at the optimal values of the initial runs, and used the phasefolded light curve (see Sect. 5.3 for details) for the final runs.

To account for the finite integration times of the observations, we oversampled our light curves in time space. The 30 s phasebins during eclipses and transits were oversampled by a factor 5, and the 1,800 s phasebins out of eclipse by a factor 3. For the oversampling, we approximated the effective integration time for each bin by  $\sqrt{I^2 + x^2}$ , in which I is the integration time of the binned short cadence data points (about 58 s) and x is the width of the bin (30 or 1,800 s). To explore the effects of rapid rotation, we ran MCMC chains assuming corotation (as in the case of KPD 1946+4340), as well as chains treating the spin rate as a free parameter with  $v \sin i = 150 \pm 10 \,\mathrm{km \, s^{-1}}$  as a prior. This prior was implemented as a constraint on  $(2\pi R/P) \sin i$ . In total, we computed over 450,000 light curves in the corotation chain, plus about 400,000 light curves in the fast rotation chain with spectroscopic prior on the spin rate. Every tenth model that was computed was stored and used to determine the system parameters.

We set the limb darkening coefficients to the values found in Sect. 5.3.2 and used priors on the flux weighted temperature of the primary ( $T_1 = 9,500 \pm 250$  K, taken from spectroscopy, see Sect. 5.2), the gravity darkening coefficient of the primary ( $\beta_K = 0.55 \pm 0.05$ , see Sect. 5.3.2) and the radial velocity amplitude of the primary ( $K_1 = 15.4 \pm 0.3$  km s<sup>-1</sup>, taken from spectroscopy, see Sect. 5.2). If the amplitude of the Doppler beaming effect is consistent with the radial velocity amplitude, as was the case for KPD 1946+4340 (see Chap. 4), the results of the analysis will be identical when the prior on  $K_1$  would be replaced by a prior on  $\langle B \rangle$ . In our approach, putting a prior on  $K_1$  and treating  $\langle B \rangle$  as a free parameter, we can judge whether the Doppler beaming effect has the expected amplitude by comparing the  $\langle B \rangle$  that results from our MCMC analysis with the one found from atmosphere models in Sect. 5.3.2.

#### 5.3.4 MCMC Results and Discussion

As can be seen in Fig. 5.3, the light curve model fits the observed data very well. There is some structure in the residuals around the transit ingress and egress (around orbital phase 0.5), but it is barely significant. This structure can for example result from a small difference between the assumed limb darkening coefficients (which were derived for a spherical star) and the true limb darkening of the A-star. The parameters derived from our MCMC runs that account for the rapid rotation of the

	Primary (A-star)	Secondary (WD)	
P <sub>orb</sub> (d)	5.188675(4)		
i (deg)	$87.0 \pm 0.4$		
T <sub>eff</sub> (K)	$9,500 \pm 250$	$14500 \pm 500$	
qell,corot	$0.052 \pm 0.004$		
qell, vsini	$0.047 \pm 0.004$		
$q_{ m RV}$	$0.104 \pm 0.004$		
$R(R_{\odot})$	$2.14 \pm 0.08$	$0.044 \pm 0.002$	
<i>M</i> (M <sub>☉</sub> )	$2.2 \pm 0.2$	$0.228 \pm 0.014$	
$v \sin i  (\mathrm{km  s}^{-1})$	$150 \pm 10$	_	
$\delta t$ Rømer (s)	$-56 \pm 17$		
$\langle B \rangle$	$2.24 \pm 0.05$	_	

**Table 5.2** Properties of KOI-74. The mass of the primary, the effective temperature and the rotational velocity are derived from spectroscopy

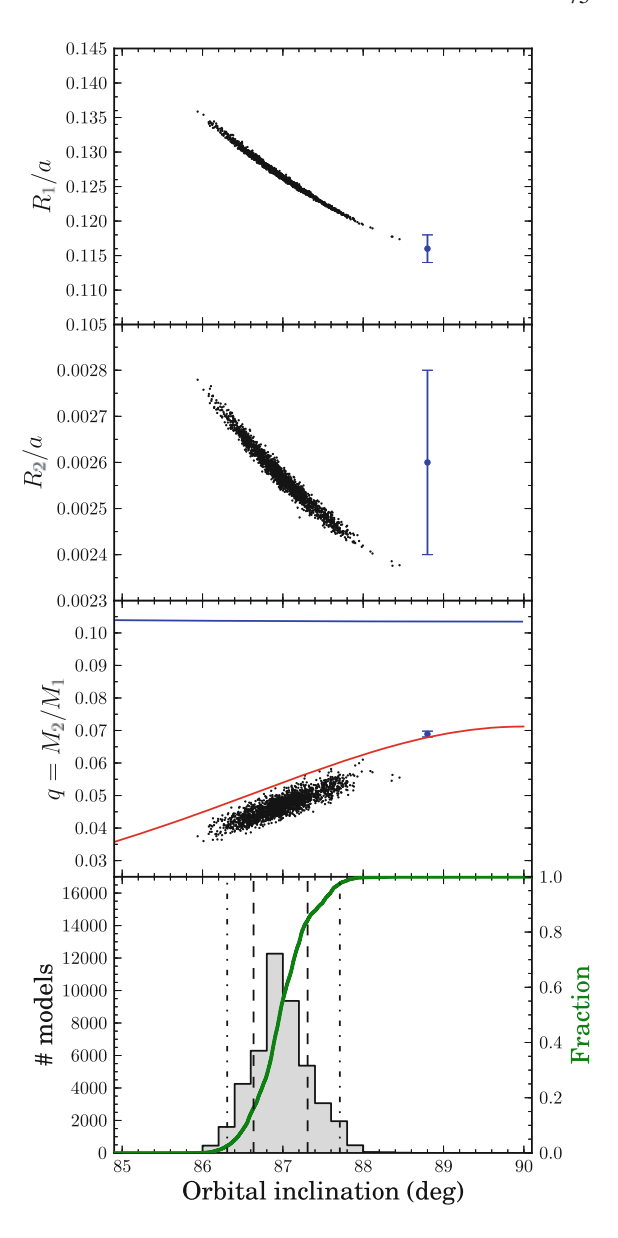
The other parameters are the result of our MCMC analysis of the *Kepler* data. The two different mass ratios are derived from the information contained in the ellipsoidal modulation amplitude  $(q_{\text{ell}})$  and the radial velocity  $(q_{\text{RV}})$ . The mass of the secondary is derived using  $q_{\text{RV}}$ 

primary, using the prior on  $v \sin i$ , are summarized in Table 5.2. Rowe et al. (2010) determined  $M_1 = 2.2 \pm 0.2 \,\mathrm{M}_\odot$  based on the spectral type. Using the evolutionary model grids of Briquet et al. (2011) and our spectroscopic determinations of  $T_{\rm eff}$  and log g, we find the same result, which we adopted for our analysis.

The results of the MCMC chains for the corotating case are nearly identical except for the derived mass ratios. The mass ratio from the models assuming corotation is also listed in Table 5.2, to allow for comparison with previously published values. The most important difference between our results and those previously published, is that our inclination  $i=87.0\pm0.4^{\circ}$  differs by  $\sim 3\sigma$  from the value derived by Rowe et al. (2010),  $i=88.8\pm0.5^{\circ}$ . In that paper, the inclination was determined by fitting the eclipses and transits using the analytical formulae of Mandel and Agol (2002), which include limb darkening but not gravity darkening. Furthermore, it is possible that the authors did not account for the finite exposure times, which significantly smear out the eclipse ingresses and egresses in the long cadence data they had available. Fitting only the 43 d of long cadence data that Rowe et al. (2010) used, we find an uncertainty on the inclination of 0.9°, compared to their more optimistic value of 0.5°. The 4 months of short cadence observations allowed us to determine the inclination more reliably.

The distribution of the inclination values in our MCMC runs using the prior on  $v \sin i$  is shown in the bottom panel of Fig. 5.5. The two top panels of the figure show our radius estimates (relative to the separation of the two stars, a) as a function of the inclination. The blue points with error bars indicate the values found by Van Kerkwijk et al. (2010), who did not derive the inclination independently but instead adopted the value of Rowe et al. (2010). Due to our lower preferred inclination,

Fig. 5.5 Illustration of the correlation between the inclination of the system and the mass ratio and radii of the stars. The bottom panel shows the distribution of the models that were accepted in our MCMC runs that account for the rapid rotation of the primary. The dashed (dot-dashed) line indicates the 68 (95)% confidence interval. The black dots represent a random selection of the models. The blue dots with error bars show the results from Van Kerkwijk et al. (2010). The red line on the mass ratio plot is the theoretical relation based on Eqs. (5.3) and (5.4), assuming corotation. The blue line shows the mass ratio derived from  $K_1$  (Eq. 5.5)



the radii inferred in our analysis are slightly larger than the ones obtained by Van Kerkwijk et al. (2010).

The third panel of Fig. 5.5 shows the mass ratio as a function of the inclination. The red line is the theoretical relation, assuming corotation, based on the constraints offered by the transit duration (Eq. 5.3) and the ellipsoidal modulation amplitude (Eq. 5.4). The distribution of points from our corotation runs, falls nicely around this

line (not shown). The blue line shows the mass ratio derived from the spectroscopic  $K_1$ , or equivalently, as we will see further in this Section, the Doppler beaming amplitude. The discrepancy between the mass ratios derived from the ellipsoidal modulation amplitude on one hand, and from the radial velocity information on the other hand, was already noted by Van Kerkwijk et al. (2010). The results of the models that account for rapid rotation of the primary are plotted with black dots. It is striking that these models result in lower rather than higher mass ratios, thus only increasing the discrepancy compared to the models assuming corotation. The lower preferred inclination value also contributes to the increase in the discrepancy between the two mass ratios, compared to the discrepancy shown by Van Kerkwijk et al. (2010). This can easily be understood: as i gets lower,  $K_1/a$  has to increase to make the model fit the observed transit duration (Eq. 5.3); but a higher  $K_1/a$  would lead to a higher ellipsoidal modulation amplitude, which is then compensated in the simulations by lowering  $g_{\rm ell}$  (Eq. 5.4).

The beaming factor derived from the MCMC chains,  $\langle B \rangle = 2.24 \pm 0.05$ , agrees with the beaming factor derived from spectroscopy in Sect. 5.3.2 ( $\langle B \rangle = 2.19 \pm 0.04$ , taking reddening into account). We could thus have modelled the binary equally well without spectroscopic radial velocity information, just relying on the Doppler beaming amplitude in the *Kepler* light curve, verifying Van Kerkwijk et al. (2010)'s approach.

One can argue that the mass ratios determined from the ellipsoidal modulation amplitude and radial velocity information can be brought into agreement by assuming a high contamination of the *Kepler* light curve by background stars, since this would increase the observed ellipsoidal modulation amplitude. The consistency between the observed Doppler beaming amplitude (which would also increase if one assumes a higher contamination) and the spectroscopic radial velocity amplitude, however, implies that our assumption of no background contamination in the *Kepler* light curve has to be correct up to a few per cent.

We were also able to measure the Rømer delay at  $\delta t = -56 \pm 17$  s, as can be seen on the distribution plot from our MCMC chains on Fig. 5.6. The expected Rømer

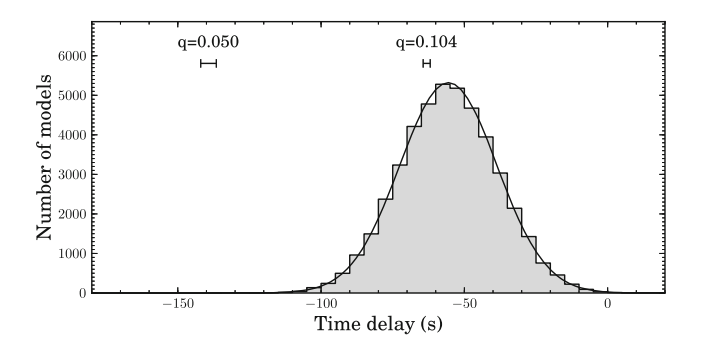


Fig. 5.6 Distribution of the Rømer delay as fitted by our MCMC runs. The delays expected for mass ratios of q = 0.050 and q = 0.104 are indicated for comparison

delay for a mass ratio of q = 0.104 is  $\delta t = -63.2 \pm 1.2$  s, while for q = 0.050 we would expect  $\delta t = -139 \pm 3$  s (the error bars account for the uncertainty on  $K_1$  measured from spectroscopy). The Rømer delay estimates only depend on  $P_{\rm orb}$ ,  $K_1$  and the mass ratio. With  $P_{\rm orb}$  and  $K_1$  firmly established from both spectroscopy and photometry, the measurement of the delay proves that the true mass ratio of the system is the one derived from the radial velocity amplitude, under the condition that the orbit is circular. Note that, while  $K_1$  can be derived from the Doppler beaming amplitude, a measurement of the Rømer delay allows one to also derive  $K_2$  directly from the light curve if  $M_1$  is known.

#### 5.3.5 Variability in Residuals

We performed a time-frequency analysis on the residuals of the short cadence data after subtracting our best model. The time-frequency diagram is shown in Fig. 5.7. We detected significant variability (following the criteria given in Degroote et al. 2009), but all at low amplitudes ( $\sim$ 10 parts per million). We found variability with periods of  $\sim$ 3 d, which is a known instrumental artefact (see Christiansen et al. 2011). We also found variability with a period of 0.5918  $\pm$  0.0015 d, with an amplitude that changes in time (see Fig. 5.7). Van Kerkwijk et al. (2010) suggested that this signal could be associated with the spin period of the A-star. Given our spectroscopic value for  $\nu \sin i$  and the radius determination from our light curve analysis, we expect the spin period of the A-star to be 0.72  $\pm$  0.06 d, which differs by  $2\sigma$  from the detected periodicity.

We detected additional variability of similar amplitude in the long cadence Q2 data at frequencies between 15 and 20 d<sup>-1</sup>. We could find a similar signal in the observations of KIC 6889190, which is observed on the same CCD close to KOI-74, and it can be removed successfully using the cotrending basis vectors technique

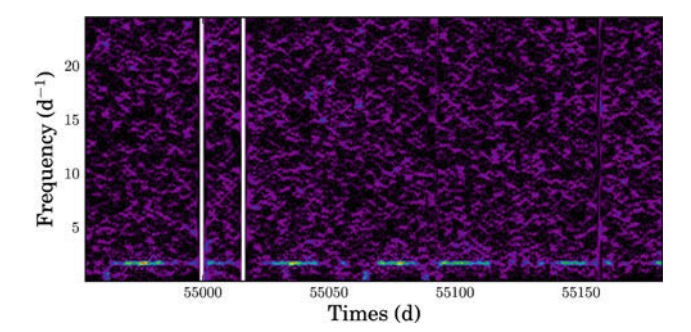


Fig. 5.7 Time-frequency analysis of the residuals of the short cadence data after subtracting our best fitting binary light curve model. The observed variability at  $\sim$ 1.3 d<sup>-1</sup> might be related to the spin period of the primary star

described in Christiansen et al. (2011) (Tom Barclay, priv. comm.). This confirms that it is instrumental in nature.

We did not find significant residual power at the orbital period which proves that the LCURVE model fits the data very well.

#### **5.4 Summary**

We have analysed 212 d of *Kepler* data (Q0, Q1, Q2 and Q3) of the eclipsing binary KOI-74, as well as supporting spectroscopic observations. We modelled the light curve using the LCURVE code, accounting for ellipsoidal modulation, reflection effects, Doppler beaming, Rømer delay, eclipses and transits. Using Markov Chain Monte Carlo simulations, we determined various system parameters of KOI-74, which are summarised in Table 5.2. We find a lower orbital inclination of  $i=87.0\pm0.4^{\circ}$  compared to the discovery paper and first analysis presented by Rowe et al. (2010) and adopted by Van Kerkwijk et al. (2010),  $i=88.8\pm0.5^{\circ}$ . The difference propagates to our values of other parameters such as the radii. It lowers the mass ratio derived from the ellipsoidal modulation amplitude to  $q=0.052\pm0.004$  assuming corotation or  $q=0.047\pm0.004$  accounting for a rapidly rotating primary (using  $v \sin i = 150\pm10\,\mathrm{km\,s^{-1}}$  as a prior).

The amplitude of the observed Doppler beaming, which makes the primary become brighter when the star moves in the direction of the *Kepler* satellite in its orbit, is in perfect agreement with what is expected from the spectral type and radial velocity amplitude of the star, which we determined to be  $K_1 = 15.4 \pm 0.3 \, \mathrm{km \, s^{-1}}$  from spectroscopy. From the primary's mass of  $2.2 \pm 0.2 \, \mathrm{M}_{\odot}$  the mass ratio derived from the radial velocity is  $q = 0.104 \pm 0.004$ .

We also report the first detection of Rømer delay in a light curve of a compact binary. This delay, which amounts to  $56\pm17\,\mathrm{s}$ , is exactly as long as one would expect for a mass ratio of  $q\sim0.1$ , and is in contradiction with the lower mass ratio derived from the ellipsoidal modulation amplitude. Van Kerkwijk et al. (2010) preferred the mass ratio derived from the Doppler beaming amplitude over the mass ratio derived from the ellipsoidal modulation amplitude. We find that the spectroscopic radial velocity amplitude as well as the Rømer delay leave no doubt that this was indeed the correct assumption, and that the secondary of KOI-74 is a low mass white dwarf.

As a result of our lower preferred orbital inclination value, the discrepancy between the mass ratio determined from the ellipsoidal modulation amplitude and the higher mass ratio determined from radial velocity information or Rømer delay has increased compared to Van Kerkwijk et al. (2010), and now amounts to a factor 2. Our attempt to account for the effect of the rapid rotation of the primary, increased the discrepancy even further. Our results imply that one has to be very cautious when adopting mass ratio estimates derived from the ellipsoidal modulation amplitude, in particular if there is no firm proof of corotation. We are not aware of any theoretical explanation of the reduction in ellipsoidal modulation as a result of rapid asynchronous rotation.

References 79

#### References

Bloemen, S., Marsh, T. R., Degroote, P., et al. (2012). MNRAS, 422, 2600.

Breton, R. P., Rappaport, S. A., van Kerkwijk, M. H., & Carter, J. A. (2012). ApJ, 748, 115.

Briquet, M., Aerts, C., Baglin, A., et al. (2011). A&A, 527, A112.

Cardelli, J. A., Clayton, G. C., & Mathis, J. S. (1989). ApJ, 345, 245.

Carter, J. A., Rappaport, S., & Fabrycky, D. (2011). ApJ, 728, 139.

Castelli, F., & Kurucz, R. L. (2004). arXiv:astro-ph/0405087.

Christiansen, J. L., Van Cleve, J. E., Jenkins, J. M., et al. (2011). Kepler Data Release 11 Notes, KSCI-19051-001.

Claret, A. (2003). A&A, 406, 623.

Claret, A. (2004). A&A, 428, 1001.

Copperwheat, C. M., Marsh, T. R., Dhillon, V. S., Littlefair, S. P., Hickman, R., Gänsicke, B. T., et al. (2010). MNRAS, 402, 1824.

Debosscher, J., Blomme, J., Aerts, C., & De Ridder, J. (2011). A&A, 529, A89.

Degroote, P., Aerts, C., Ollivier, M., et al. (2009). A&A, 506, 471.

Donati, J.-F., Semel, M., Carter, B. D., Rees, D. E., & Collier Cameron, A. (1997). MNRAS, 291, 658.

Ehrenreich, D., Lagrange, A., Bouchy, F., et al. (2011). A&A, 525, A85.

Faigler, S., Mazeh, T., Quinn, S. N., Latham, D. W., & Tal-Or, L. (2012). ApJ, 746, 185.

Gray, D. F. (1992). The observation and analysis of stellar photospheres. Cambridge: Cambridge University Press.

Kaplan, D. L. (2010). ApJ, 717, L108.

Koester, D. (2010). Memorie della Societa Astronomica Italiana, 81, 921.

Kruszewski, A. (1963). Acta Astronomica, 13, 106.

Loeb, A., & Gaudi, B. S. (2003). ApJ, 588, L117.

Mandel, K., & Agol, E. (2002). ApJ, 580, L171.

Marsh, T. R. (2001). MNRAS, 324, 547.

Maxted, P. F. L., Anderson, D. R., Burleigh, M. R., et al. (2011). MNRAS, 418, 1156.

Mazeh, T., & Faigler, S. (2010). A&A, 521, L59+.

Morris, S. L., & Naftilan, S. A. (1993). ApJ, 419, 344.

Munari, U., Sordo, R., Castelli, F., & Zwitter, T. (2005). A&A, 442, 1127.

Pápics, P. I., Briquet, M., Baglin, A., et al. (2012). A&A, 276, 393.

Raskin, G., Van Winckel, H., Hensberge, H., et al. (2011). A&A, 526, A69.

Rowe, J. F., Borucki, W. J., Koch, D., et al. (2010). ApJ, 713, L150.

Royer, F., Gerbaldi, M., Faraggiana, R., & Gómez, A. E. (2002). A&A, 381, 105.

Russell, H. N. (1912). ApJ, 35, 315.

Shporer, A., Jenkins, J. M., Rowe, J. F., et al. (2011). AJ, 142, 195.

Simón-Díaz, S., & Herrero, A. (2007). A&A, 468, 1063.

Slawson, R. W., Prša, A., Welsh, W. F., et al. (2011). AJ, 142, 160.

Van Kerkwijk, M. H., Rappaport, S. A., Breton, R. P., Justham, S., Podsiadlowski, P., & Han, Z. (2010). *ApJ*, 715, 51.

Zucker, S., Mazeh, T., & Alexander, T. (2007). ApJ, 670, 1326.

## Chapter 6 A New Grid of Evolutionary Subdwarf B Star Models and Their Pulsational Properties

Abstract We present a new grid of evolutionary subdwarf B-star models that was computed taking into account diffusion processes such as radiative levitation and gravitational settling. We also compute the non-adiabatic pulsation properties of the stars along the evolutionary track. We find that the build-up of Fe and Ni in the pulsation driving region is larger than expected. The gravity mode instability strip extends further to the blue, solving the so-called 'blue-edge problem' compared with the observed V1093 Her pulsators. Finally, we compute expected amplitude ratios of modes observed in different colour bands. We conclude that our results are in agreement with previous studies for pressure mode pulsators. For gravity mode pulsations, we see significant changes in the amplitude ratios along an evolutionary track.

#### 6.1 Introduction

Subdwarf B stars (sdBs) are extreme horizontal branch stars burning helium in their cores (for a good review on sdBs, see Heber 2009). They typically have masses around  $0.5\,M_\odot$  and have only a thin hydrogen layer left at their surfaces, which is too thin to sustain hydrogen shell burning. Due to their thin envelopes, sdBs are unusually bright in the near-UV. They are identified as the source of the unexpected UV-upturn observed in elliptical galaxies (Podsiadlowski et al. 2008). The formation of sdBs is not well understood. It is unclear how the sdB progenitors lost most of their hydrogen envelopes.

More than 50% of the sdBs have been found to be part of short period binaries (Maxted et al. 2001). This suggests that binary evolution may play a key role in their formation. Several evolutionary channels have been proposed: (1) common-envelope ejection channels, leading to sdBs in binaries with orbital periods below  $\sim 10\,\mathrm{d}$  and a white dwarf or low-mass main sequence companion; (2) a stable Roche lobe overflow channel resulting in binary systems with orbital periods between  $\sim 10\,\mathrm{and} \sim 100\,\mathrm{d}$  and much thicker hydrogen envelopes; and (3) a double helium white dwarf merger channel that gives rise to single sdB stars with very thin hydrogen envelopes and a wider mass range (Han et al. 2002, 2003). Recently, sdBs with planetary companions

were found (Beuermann et al. 2012; Charpinet et al. 2011; Silvotti et al. 2007), rejuvenating the idea that interactions of a star with a planetary companion might also lead to the formation of sdBs (Soker and Harpaz 2000). The evolutionary scenarios remain largely untested. Since they result in different predicted populations of sdBs, accurate determinations of their masses and envelopes, as well as periods of sdB binaries, can be used to discriminate between the different channels.

Many sdBs show stellar oscillations. Pulsation modes for which the pressure force is the dominant restoring force, p-modes, were predicted in sdB stars by Charpinet et al. (1996) and discovered around the same time by Kilkenny et al. (1997). The first detection of gravity (g-) mode pulsations, for which buoyancy is the dominant restoring force, in sdBs was accomplished by Green et al. (2003). Asteroseismic techniques can therefore be used to probe the internal structure of sdBs and to measure the masses of their cores and envelopes. Asteroseismology of sdBs is not only useful to constrain the evolutionary scenarios, but also allows us to test our knowledge of physical processes such as atomic diffusion and stellar winds, as well as to test tidal theory through spin-orbit synchronisations of sdBs in short period binaries (Pablo et al. 2011, 2012). Recent reviews of sdB asteroseismology can be found in Fontaine et al. (2006), Østensen (2009, 2010) and Kawaler (2010).

Pulsations in sdBs are driven by the opacity ( $\kappa$ ) mechanism (shown by Charpinet et al. 1997 for p-modes and Fontaine et al. 2003 for g-modes) which operates in stellar layers where chemical elements are partially ionized. In these regions, a heat engine converts radiation into kinetic energy. During the contraction phase of a pulsation cycle, the opacity increases and energy that is radiated outwards gets trapped. It heats up the material and causes it to expand, after which the cycle repeats.

An accurate modelling of the abundance profiles of the ionized elements in different layers of the star is required to understand the opacity-related mode driving. These abundance profiles are influenced by diffusion processes and stellar winds, which therefore have to be taken into account in stellar models. In particular, proper treatments of radiative levitation and gravitational settling are needed.

Although Fontaine et al. (2003) showed that an Fe opacity bump in the envelope of sdB stars (in the layers with  $T \sim 200,000 \,\mathrm{K}$ ) can excite g-modes, the stars that were theoretically predicted to show g-mode pulsations were several thousand Kelvin too cool compared to the observed pulsators. Using OP (Badnell et al. 2005) instead of OPAL (Iglesias and Rogers 1996) opacity tables, and by enhancing not only the Fe but also the Ni abundance in the envelope, Jeffery and Saio (2006) obtained a predicted instability strip that reduced the so-called 'blue-edge problem'. Using artificial enhancements of Fe and Ni in the pulsation driving region, Hu et al. (2009) showed that gravitational settling, thermal diffusion and concentration diffusion acting on H and He shifts the theoretical blue-edge of the instability strip further to about 1,000 K from the observed value (Hu et al. 2009). Recently, Hu et al. (2011) added diffusion due to radiative levitation to their evolution code, next to the already implemented gravitational settling, thermal diffusion and concentration diffusion, and solved the diffusion equations for H, He, C, N, O, Ne, Mg, Fe and Ni. Due to the inclusion of radiative levitation, Fe and Ni enhancements are built up in the pulsation driving region, therefore eliminating the need to include artificial abundance 6.1 Model Grid 83

enhancements. The authors showed that the resulting evolutionary models can excite low-degree *g*-modes at relatively high effective temperatures, suggesting that the blue-edge problem could be resolved. In this Chapter, we present a grid of models computed using the codes of Hu et al. (2011) to readdress the instability strip issue. We also present computations of amplitude ratios of pulsation modes observed in different colour bands, which are required for mode identification.

#### 6.2 Model Grid

We have set up tools to compute grids of evolutionary tracks of sdB stars using a modified version of the stellar evolution code STARS (Eggleton 1971). The most important changes are the implementation of gravitational settling, thermal diffusion and concentration diffusion by Hu et al. (2010), the implementation of radiative levitation by Hu et al. (2011) and the coupling of the STARS code to the non-adiabatic pulsation code MAD (Dupret 2001) as described in Hu et al. (2008). The evolutionary tracks are computed starting from red giant branch models from which most of the envelope was stripped off. The free parameters of the starting models are the total mass of the star and the mass of the remaining hydrogen envelope. For the grid presented here, we assumed solar metallicity with the metal mixture of Grevesse and Noels (1993) and no mass loss due to winds during the sdB evolution. The total masses ( $M_*$ ) range from 0.35 to 0.55  $M_{\odot}$  and the envelope masses from  $10^{-5}$  to  $10^{-1.8}$   $M_*$ . The computation of one evolutionary track takes about 6 days of CPU time on a single core of a 2.8 GHz quad-core Intel Xeon X5560 Nehalem CPU.

#### 6.3 Instability Strips

Hu et al. (2011) showed that the build up of the Fe abundance in the driving region proceeds relatively quickly and reaches an equilibrium situation in about 10<sup>5</sup> years, as was also shown by Fontaine et al. (2006). Hu et al. (2011) found that it takes longer before the equilibrium situation is reached for Ni, but this also happens in less than 10<sup>7</sup> yr. For the test track presented in that paper, it was clear that the Ni abundance increase compared to the initial abundance was much higher than was previously assumed. From our grid spanning a range of envelope masses and total masses, we have measured the height of the Fe and Ni abundance peaks in the driving region 10<sup>7</sup> years after the start of the sdB evolution on the zero-age horizontal branch. The resulting abundance enhancement factors compared to the initial abundance are shown in Fig. 6.1 for Fe and in Fig. 6.2 for Ni.

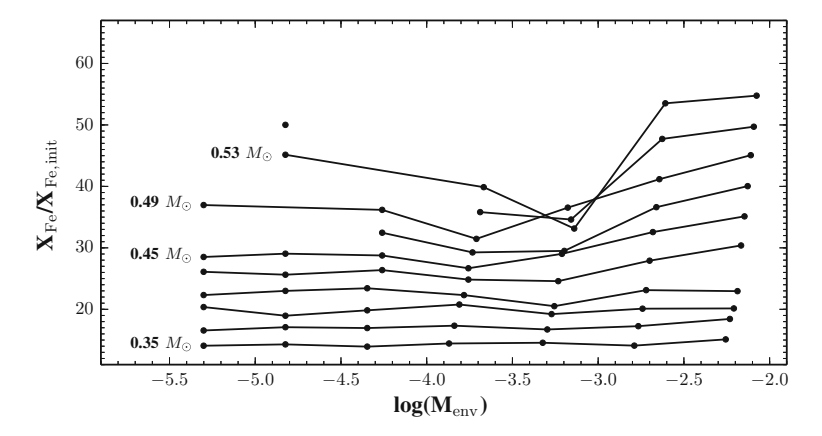


**Fig. 6.1** Abundance enhancement of Fe in the driving region at  $T = 200,000 \,\mathrm{K}, \, 10^7$  years after the start of central He burning. The *lines* connect the enhancement factors of models with the same total mass but different envelope masses

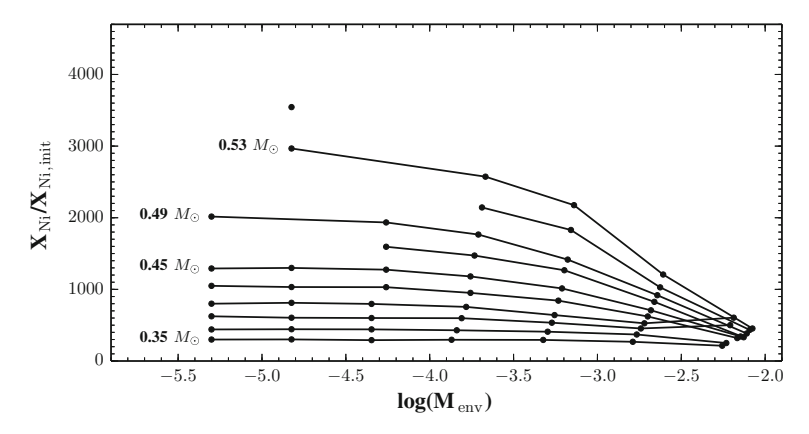


**Fig. 6.2** Same as Fig. 6.1 but for Ni instead of Fe. In earlier work, enhancement factors of 10 or 20 were assumed, which is clearly an underestimation

While previous studies of the instability strips of sdBs used parametrized enhancement factors of up to 20 for the abundances of Fe and Ni in the driving regions (Hu et al. 2008; Jeffery and Saio 2006), our simulations predict that especially the Ni abundance increase is orders of magnitude higher. For low mass models  $(M_* = 0.35\,\mathrm{M}_\odot)$ , we find an increase by a factor  $\sim\!300$  for Ni. For higher mass models, we find enhancement factors up to 4,000. This large difference in enhancement factors is explained by the difference in initial abundances: Fe is 16.1 times more abundant at the start, since we use the Grevesse and Noels (1993) mixture. In Fig. 6.3 we show the ratio of the Ni and Fe abundance in the driving region, which is close to unity, in agreement with the results presented by Michaud et al. (2011). For the models with thin envelopes, there is a clear upwards trend of the Ni to Fe ratio with rising total mass.

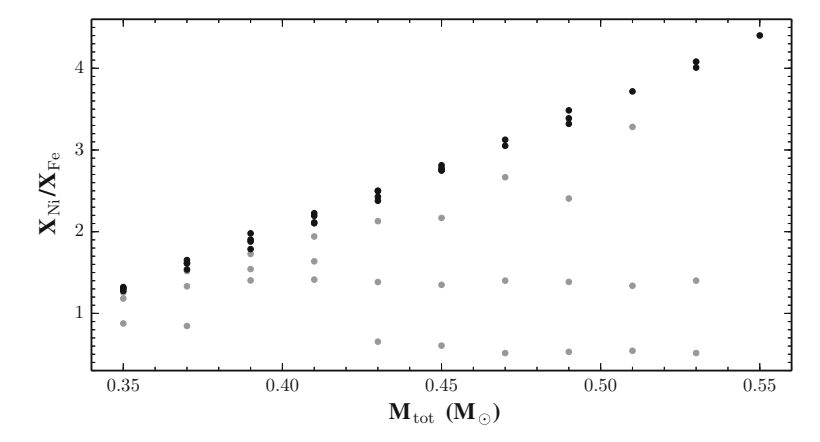


**Fig. 6.3** The abundance ratio of Ni and Fe in the driving region after  $10^7$  years versus the total mass of the star. Models with *thin* envelopes  $(\log(M_{\rm env}/{\rm M_{\odot}}) < 3.5)$  are shown in *black*, and follow a clear upwards trend with increasing total mass. The *grey dots* represent models with *thicker* envelopes

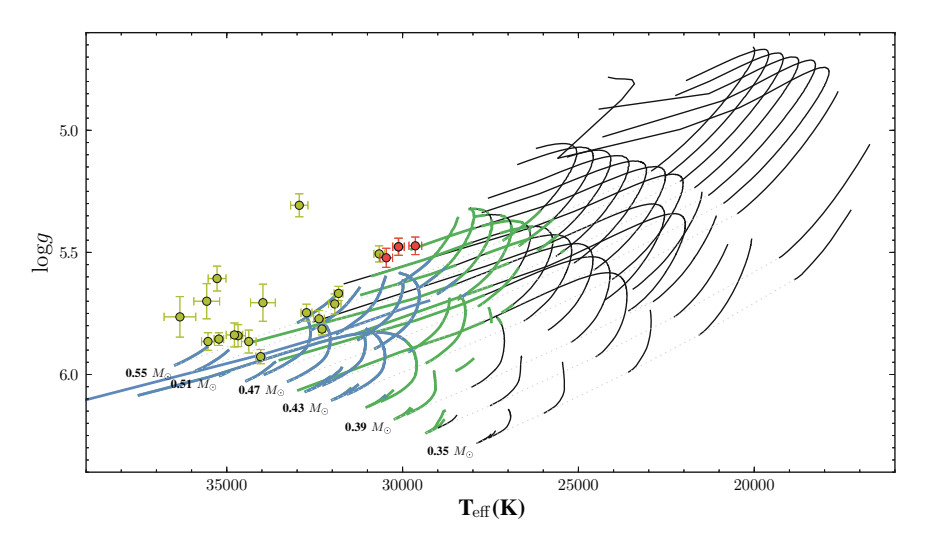
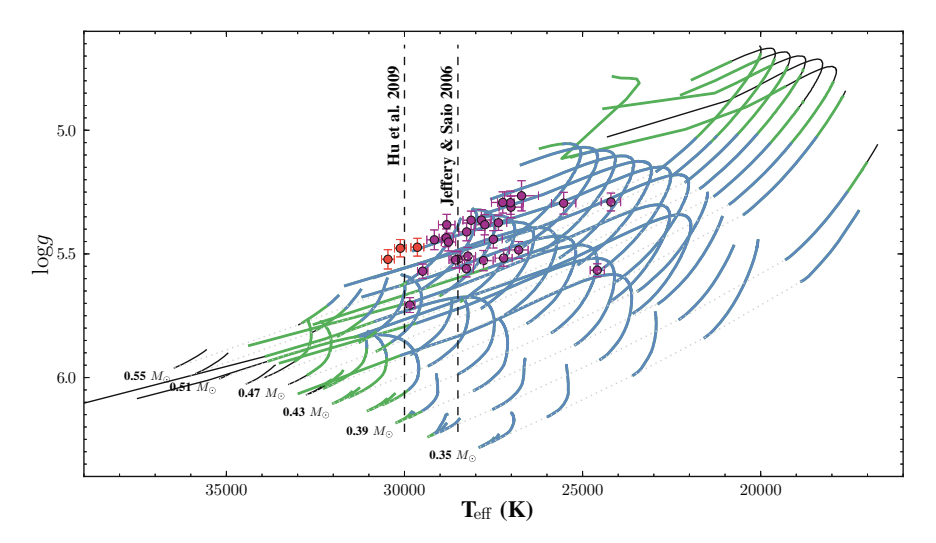


Fig. 6.4 Instability strip for p-mode pulsations in sdB stars. The initial points of evolutionary tracks of stars with identical core masses are connected with a *grey dotted line* and the masses are indicated on the plot. Envelope masses rise from *left* to *right* and range from  $10^{-5} M_*$  to  $10^{-1.8} M_*$ . Sections of the tracks where more than 10% and more than 25% of the p-modes with *spherical* degree  $l \le 2$  are predicted to be excited, are coloured in *green* and *blue*, respectively. The rest of the tracks is shown in *black*. A sample of known p-mode pulsators are indicated with *yellow* points and *red* points indicate known hybrid pulsators

The higher Fe and Ni opacity bumps in the driving region influence the instability strips. An example of the modes that are excited is shown for one evolutionary track ( $M_{\text{tot}} = 0.47 \, \text{M}_{\odot}$ ,  $M_{\text{env}} = 9.0 \times 10^{-5} \, \text{M}_{\odot}$ ) in Fig. 6.6. In Fig. 6.4 we show



**Fig. 6.5** Same as Fig. 6.4 but for *g*-mode pulsations in sdB stars. *Red* points still indicate known hybrid pulsators that show *p*- and *g*-modes. *Magenta* points indicate known *g*-mode pulsators. The *vertical dashed lines* indicate the *blue* edges of the instability strips predicted by Jeffery and Saio (2006) and Hu et al. (2009)

the predicted instability strip for p-mode pulsations. The evolutionary tracks are coloured green (blue) when more than 10~(25)~% of the p-modes of spherical degree  $l \leq 2$  have a positive work integral in our non-adiabatic pulsation computations. Figure 6.5 shows the same for g-modes. The dots indicate a sample of pulsators taken from Green et al. (2008) that was already shown in Østensen (2010): p-mode pulsators are shown in yellow, g-mode pulsators in magenta and hybrid pulsators that show both p- and g-mode pulsations in red. All pulsators fall within the instability strips, which in our simulations extend to slightly cooler temperatures than the known pulsators in the case of p-modes and to hotter temperatures in the case of g-modes. The predicted instability strips for g-mode pulsations, including l=3 modes, showed a blue edge around  $28,500~\mathrm{K}$  in the study by Jeffery and Saio (2006), and around  $30,000~\mathrm{K}$  in the study by Hu et al. (2009). In our case, by only considering modes with  $l \leq 2$ , we find the blue edge around  $33,000~\mathrm{K}$ .

The larger overlap between the p- and g-mode instability strips compared to previous studies is comforting, since recent work on *Kepler* data has made clear that sdB pulsators that predominantly show g-modes often also have one or a few excited p-modes (see e.g. Baran et al. 2011) and that p-mode pulsator KIC 10139564 also shows g-mode pulsations while it has an effective temperature that is close to 32,000 K (Baran et al. 2012). The apparent offset between the spectroscopically determined surface gravities and the evolutionary tracks for typical  $\sim 0.47 M_{\odot}$  sdBs is a known, yet unsolved, problem (see e.g. Fig. 1 in Østensen 2009). In Hu et al. (2011) it was shown that a weak stellar wind or a mixing process in the envelope, effects which are not accounted for in our grid computations, both tend to reduce the

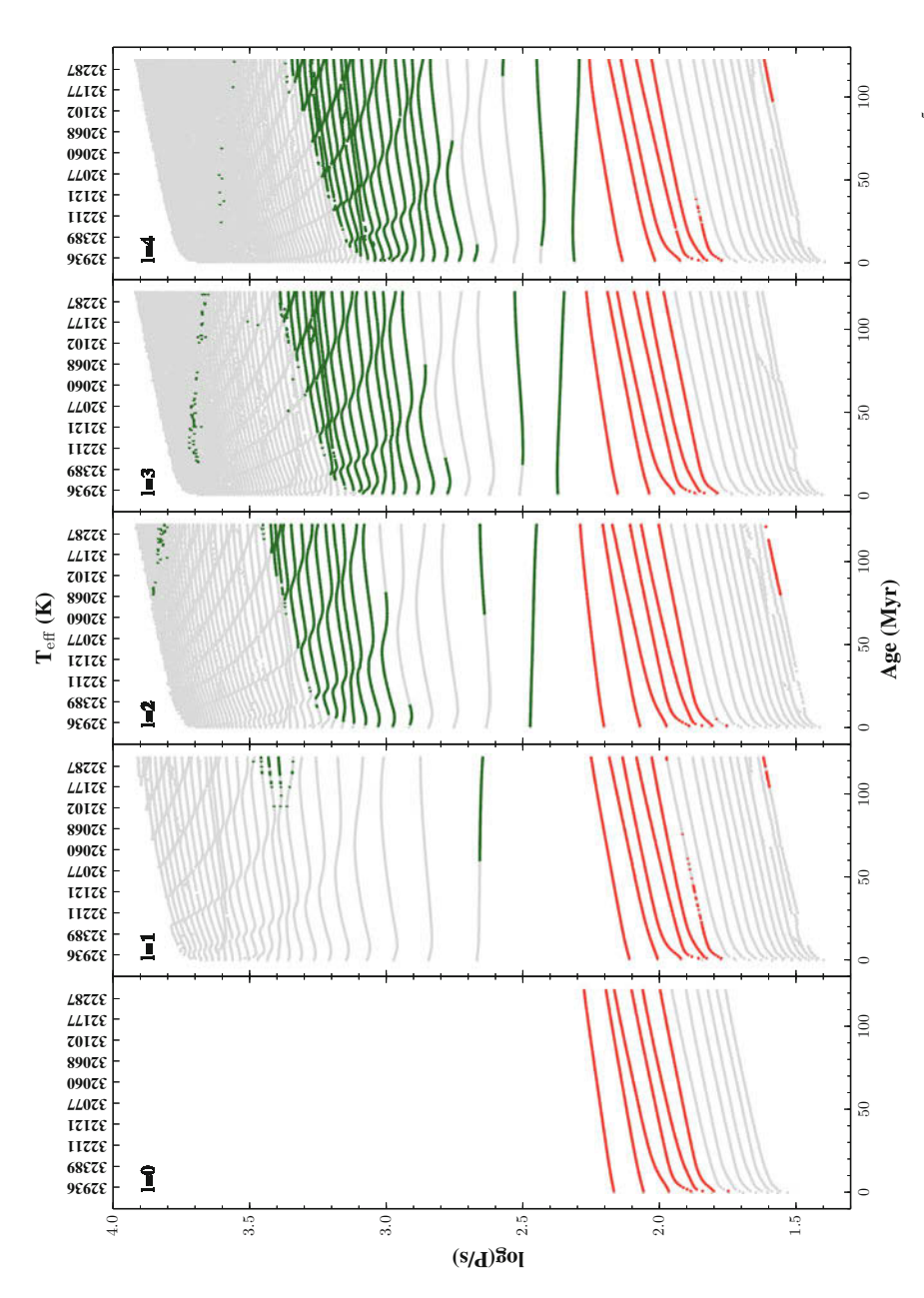


Fig. 6.6 Pulsation spectra per spherical degree for an evolutionary track with a total mass of  $0.47\,\mathrm{M}_\odot$  and an envelope mass of  $9.0\times10^{-5}\,\mathrm{M}_\odot$ . The unstable p-modes are shown in red, the unstable g-modes in green

build up of Fe and Ni in the envelope. If such a stellar wind or extra mixing process are indeed present, the instability regions we find here might shrink a bit.

#### **6.4 Amplitude Ratios**

Asteroseismology of subdwarf B stars is usually performed based on the so-called forward modelling approach, which consists of matching a set of observed pulsation frequencies to theoretically predicted pulsation frequencies as those computed for our model grid. Promising modelling results have been obtained for both *p*-mode pulsators (see e.g. Fontaine et al. 2006 for a review) and, more recently and based on *Kepler* data, for *g*-mode pulsators (e.g. Charpinet et al. 2011; Van Grootel et al. 2010). Often, however, several models match an observed set of frequencies equally well. To break that degeneracy, extra input is needed. Usually, spectroscopic parameters such as the effective temperature and surface gravity of a star are used to limit the parameter space. Another way to lift degeneracies is to try to observationally determine the spherical degree *l* of the observed pulsation modes.

Pulsation modes cause perturbations in the local radius, surface gravity and effective temperature on the surface of the star. Because limb darkening is temperature, gravity and wavelength dependent, the amplitude of flux variations caused by a pulsation mode depends on the colour band in which the variations are observed. Since the wavelength dependence is sensitive to the geometrical nature of the pulsation mode, comparing pulsation amplitudes in different colour bands allows one to put constraints on its spherical degree l. Methods to do so have been developed since long (see e.g., Chap. 6 of Aerts et al. 2010 for an overview), and are continuously being improved.

The new MAIA (Mercator Advanced Imager for Asteroseismology, see Chap. 7) instrument that was installed at the 1.2 m Mercator Telescope (La Palma, Spain) in 2012 is ideally suited to make such precise measurements of the amplitude of pulsation modes in different colour bands, as is the ULTRACAM instrument (Dhillon et al. 2007) which has been used for this in the past. In anticipation of the datasets that will be collected with this camera, we have set up methods to compute synthetic amplitude ratios for the non-adiabatic frequencies we have computed for our evolutionary grids of sdB models. Our amplitude ratio calculations are implemented following Townsend (2003), which builds on earlier work such as Dziembowski (1977) and Watson (1987, 1988). The output of the MAD pulsation code of Dupret (2001) which was adapted to produce the non-adiabatic amplitudes and phases in the outer stellar atmosphere (Dupret et al. 2002, 2003), serves as the input for our amplitude ratio computations. However, our software is constructed in such a way that it can easily accommodate non-adiabatic pulsation results from other codes as well should they become available. For the case of non-rotating sdB pulsators, the computations are equivalent to the ones outlined in Hu (2009 Chap. 6).

To compute amplitude ratios for a set of bandpasses, one also needs a grid of limb darkening coefficients which describe how the intensity of a star varies from

its center to its limb. A grid of synthetic sdB spectra with specific intensities at different angles on the stellar surface was kindly provided to us by E. Ringat and T. Rauch (University of Tübingen). The grid is computed using TMAP (Tübingen NLTE Model-Atmosphere Package, Werner et al. 2003). It spans effective temperatures ranging from 20,000 to 100,000 K and surface gravities (log *g*) ranging from 4.5 to 6.5. From these synthetic spectra, we computed limb darkening coefficients for a variety of widely used photometric filters. We integrated the specific intensities over the different bandpasses and fitted the 4-parameter limb darkening relation of Clatet (2004, Eq. 5) weighted in radius to give a more realistic fit, as proposed by Heyrovský (2007) and Hu 2009 Sect. 6.2.3).

#### 6.4.1 Changes in the Amplitude Ratios During the Evolution

Our computations reveal that the amplitude ratios for modes with similar frequencies depend on the evolutionary stage of the star. Figure 6.7 illustrates this for p-mode pulsations and Fig. 6.8 for g-mode pulsations.

In the case of the *p*-mode pulsations, modes with periods between 100 and 125 s are shown as a function of age since the zero-age extreme horizontal branch for an sdB with a total mass of  $0.47~\rm M_{\odot}$  and an envelope mass of  $9\times10^{-5}~\rm M_{\odot}$ . We show all modes in the given range, and did not require them to be excited in our simulations. For different *l*-values, the amplitude ratios are shown for the Johnson UBVRI filters, normalised to the amplitude in the U filter. In the case of the *g*-mode pulsations, modes with periods between 2,750 and 3,250 s are shown for an sdB with a total mass of  $0.49~\rm M_{\odot}$  and an envelope mass of  $7\times10^{-4}~\rm M_{\odot}$ .

The results show that amplitude ratios change significantly during the evolution of the star. In the case of p-modes, changes are only seen at the very beginning of the evolution (during the first  $\sim 5 \times 10^6 \, \rm yr$ ). This is the typical timescale needed for the diffusion processes in the envelope to reach equilibrium situations (Hu et al. 2011) and thus the stage in which these processes have the largest influence on the structure of the stars. In the case of g-mode pulsations, the amplitude ratios change significantly during the full life of the sdB. This is explained by the fact that g-modes are sensitive to the CO-core of the star, which steadily grows during the evolution.

#### 6.4.2 Comparison with Previous Work

As a benchmark, we compared the results of our simulations with those of Randall et al. (2005), which is currently the only study with concrete applications of amplitude ratios of subdwarf B star pulsations in which non-adiabatic pulsation properties are used. The models used in Randall et al. (2005) are static models, which do not include a CO-core. We have selected sdB structure models in our grid that have

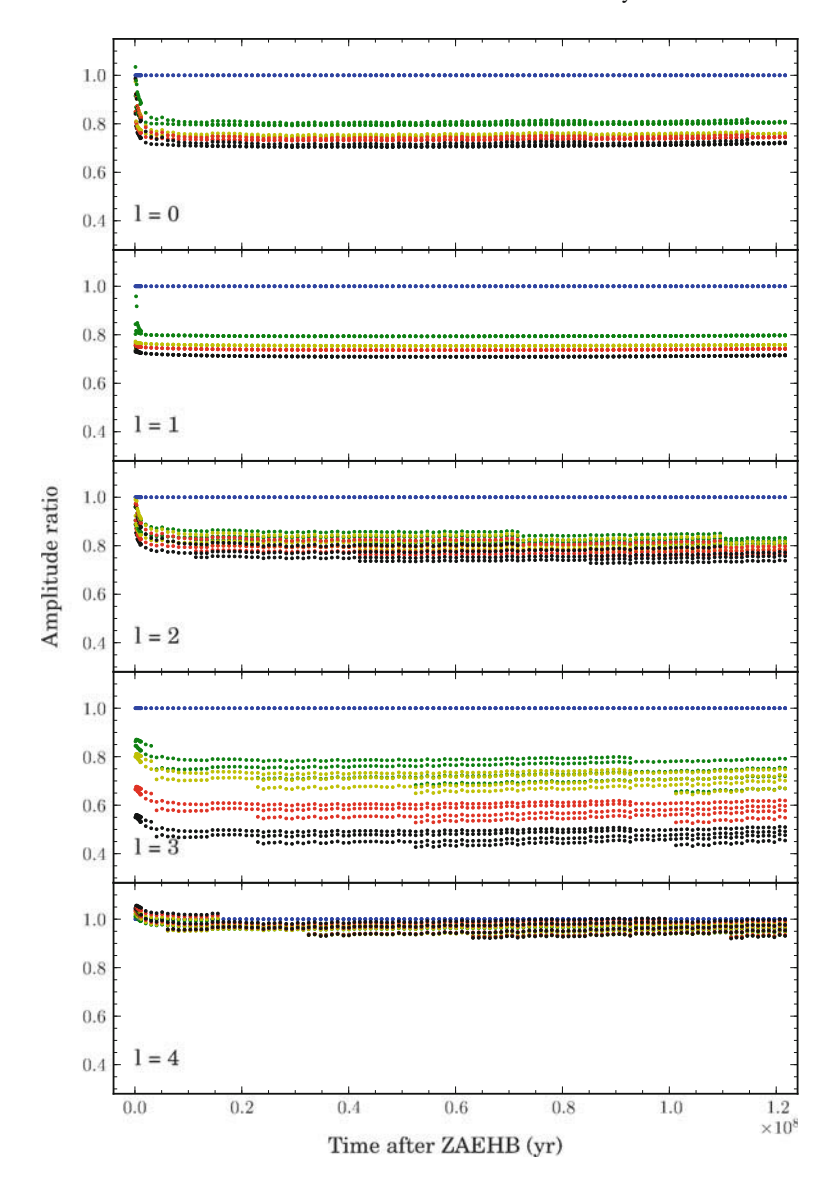


**Fig. 6.7** Evolution of synthetic amplitude ratios for p-modes during the evolution of an sdB with a total mass of  $0.47 \, \mathrm{M_\odot}$  and an envelope mass of  $9 \times 10^{-5} \, \mathrm{M_\odot}$ . The amplitude ratios for modes of different l value are shown in separate panels. Modes with periods between 100 and 125 s are shown. In each panel, from top to bottom we see the results for the Johnson U (blue, used as the reference filter), B (green), V (yellow), R (red), and I (black) filters

surface gravities and effective temperatures comparable to the two example cases presented in their paper.

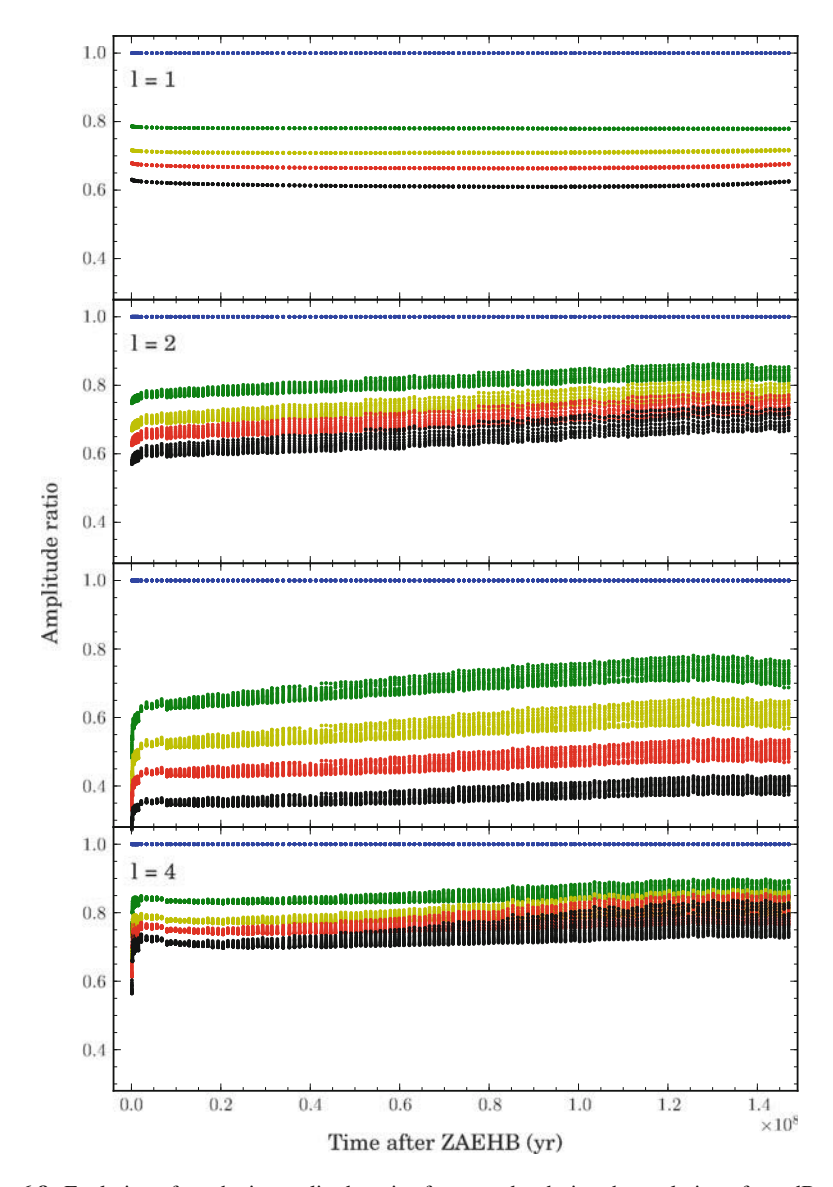


**Fig. 6.8** Evolution of synthetic amplitude ratios for g-modes during the evolution of an sdB with a total mass of  $0.49\,\mathrm{M}_\odot$  and an envelope mass of  $7\times10^{-4}\,\mathrm{M}_\odot$ . The amplitude ratios for modes of different l value are shown in separate panels. Modes with periods between 2,750 and 3,250 s are shown. In each panel, from top to bottom we see the results for the Johnson U (blue, used as the reference filter), B (green), V (yellow), R (red), and I (black) filters

To compute amplitude ratios that are representative for a p-mode pulsator, we selected models with 31,000 K <  $T_{\rm eff}$  < 35,000 K and 5.65 <  $\log g$  < 5.85.

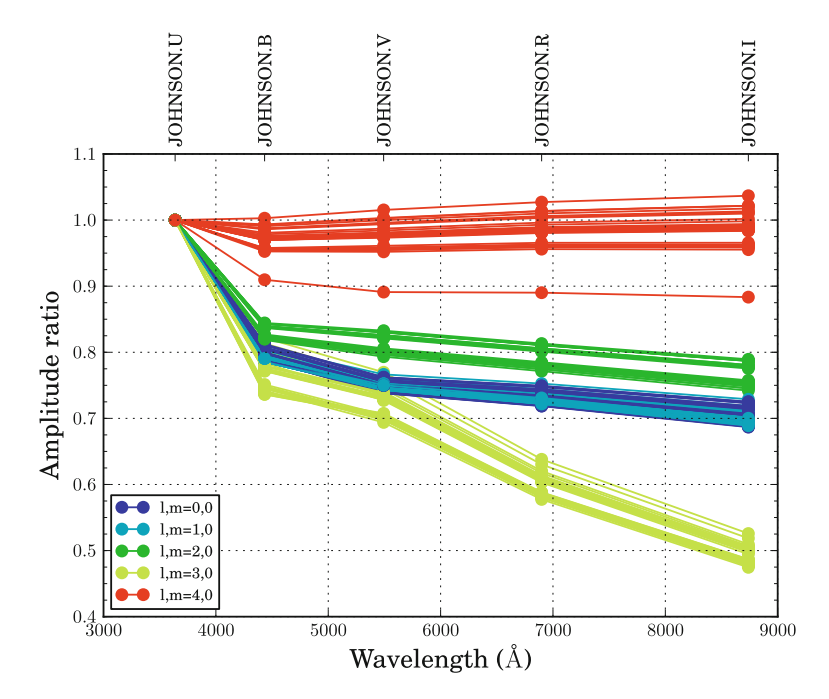


**Fig. 6.9** Amplitude ratios relative to the Johson U filter for representative models for a p-mode pulsator. All modes with periods between 140 and 160 s are shown, regardless of whether they are expected to be excited. No rotation was taken into account, hence m = 0 for all models

Figure 6.9 shows the resulting amplitude ratios in the Johnson filter system for all pulsation modes with periods in the range of  $140-160\,\mathrm{s}$ , again regardless of whether they are predicted to be excited. This makes the figure directly comparable to the second panel of Fig. 14 in Randall et al. (2005). While the figure in Randall et al. (2005) shows the amplitude ratios of one mode per l-value, we have shown all modes in the selected period range and for all selected models. This gives a feeling for the spread one can expect on the synthetic amplitude ratios when modelling a star for which properties such as the core and envelope masses are not known. All amplitude ratios shown in Randall et al. (2005) fall within 5% of our predictions, a quite comforting situation given the independent setup of our codes. We confirm that modes with spherical degrees l=0,1,2 are hard to distinguish from one another, while l=3 and l=4 modes have rather distinct amplitude ratios.

To show the results for typical g-mode pulsators, we selected models with  $26,000\,\mathrm{K} < T_\mathrm{eff} < 28,000\,\mathrm{K}$  and  $5.35 < \log g < 5.45$  and computed the amplitude ratios for the Johnson filters for modes with periods of  $3,000\pm100\,\mathrm{s}$ . The results, shown in Fig. 6.10, are directly comparable to the amplitude ratios shown in the third panel of Fig. 19 in Randall et al. (2005). In this case, the differences are more pronounced and would lead to contradicting identifications of modes with spherical degrees different from l=1. In Randall et al. (2005), the ratio of the

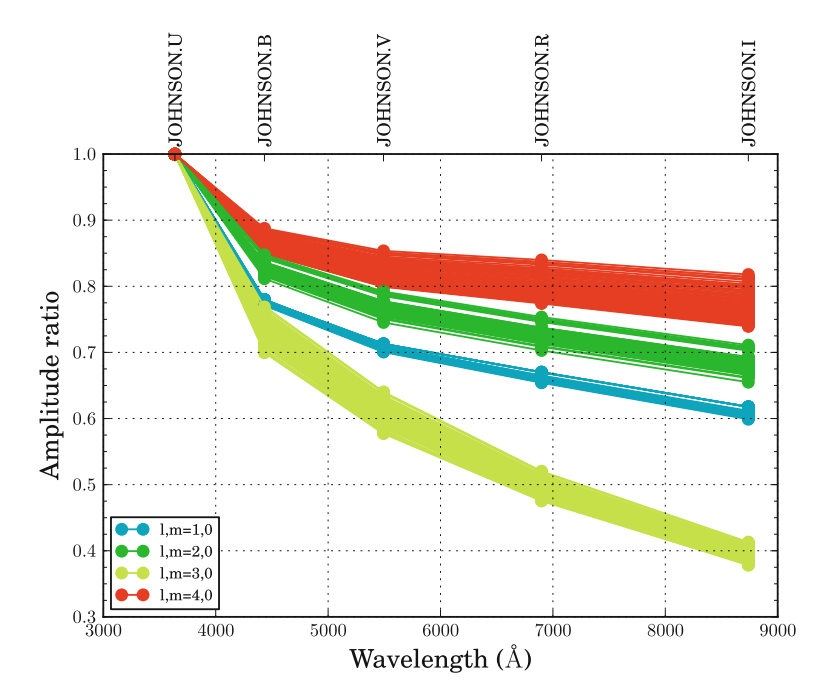


**Fig. 6.10** Same as Fig. 6.9 but for models representative for a *g*-mode pulsator. All modes with periods between 2,900 and 3,100 s are shown, regardless of whether they are expected to be excited

pulsation amplitudes in Johnson I compared to Johnson U are around 0.3, 0.5, 0.55 and 0.6 for l=3, 2, 4 and 1 modes, respectively. These values appear to be up to 25% different (for l=4 modes) in our simulations. The reason for this discrepancy is that none of the selected models is a zero-age horizontal branch model. Therefore, and contrary to the models of Randall et al. (2005), they all have at least a small CO-core, which, as we have shown above, clearly influences the amplitude ratios. The amplitude ratios of the youngest models agree to within 5% of the values found by Randall et al. (2005), but once the sdB starts evolving, the discrepancy gets larger for all modes with spherical degree l>1.

#### 6.5 Conclusions

We have computed a grid of evolutionary subdwarf B star models based on the theoretical work of Hu et al. (2011) and using their implementation of the atomic diffusion processes, which include radiative levitation, gravitational settling, thermal diffusion and concentration diffusion. The diffusion equations are solved for H, He, C, N, O, Ne, Mg, Fe and Ni. We have measured the build up of Fe and Ni in the pulsation driving region. We find that depending on the total mass of the star and

the mass of the hydrogen envelope, Fe gets enhanced by a factor of 10-60 and Ni by a factor of 300–4,000 due to the inclusion of these diffusion processes compared to the initial abundances. Previous recent studies assumed parametrized Fe and Ni enhancements of up to a factor 20 after it was realised that enhancements were needed to explain the mode excitation. These assumptions were clearly an underestimation. We have studied the effect of the Fe and Ni enhancements on the instability strip for p- and g-mode pulsators by computing the non-adiabatic pulsation properties of the models. While the g-mode instability strip in previous studies did not extend to high enough temperatures to include all known pulsators, we obtained a g-mode instability strip that predicts modes to be excited in stars with effective temperatures up to  $\sim 33,000 \,\mathrm{K}$ , which is *hotter* than what is observed and solves the problem of the too narrow instability strip. Even though Hu et al. (2011) showed that a small stellar wind or an extra source of mixing in the envelope reduces mode excitation, which can reduce the instability strip we obtained here, there is no longer any need to invoke these phenomena in the comparison of observed modes with theoretical predictions.

We have also studied amplitude ratios for typical p-mode pulsator and g-mode pulsator models. We find that amplitude ratios of modes are influenced by the structure of the star and therefore change during the evolution of the sdB. For p-mode pulsators, the amplitude ratios only change during the first  $\sim 5 \times 10^6$  yr, but g-modes are sensitive to the core of the sdB and therefore change over the full lifetime. We conclude that, certainly for g-modes, evolutionary models are needed to achieve secure mode identifications in sdBs based on amplitude ratios. Because of the dependence of the amplitudes ratios on the age of the star, amplitude ratios of g-modes will even offer an extra diagnostic to determine the evolutionary stage of pulsating sdBs.

Comparing our results to the only study available in the literature that uses non-adiabatic pulsation properties of sdBs (Randall et al. 2005) we found a satisfactory agreement for typical p-mode pulsator models. For the g-mode pulsators, we found that our results agree with those of Randall et al. (2005) for young sdBs, which is explained by the fact that the models used in Randall et al. (2005) do not have a CO-core.

With our new grid of evolutionary models and their non-adiabatic pulsational properties, we are ready for concrete applications of mode identification of sdB pulsators when observations of the new MAIA camera (see Chap. 7) become available.

#### References

Aerts, C., Christensen-Dalsgaard, J., & Kurtz, D. W. (2010). Asteroseismology. Heidelberg, Germany: Springer.

Badnell, N. R., Bautista, M. A., Butler, K., Delahaye, F., Mendoza, C., Palmeri, P., et al. (2005). *MNRAS*, 360, 458.

Baran, A. S., Kawaler, S. D., Reed, M. D., et al. (2011). MNRAS, 414, 2871.

Baran, A. S., Reed, M. D., Stello, D., et al. (2012). MNRAS, 424, 2686.

Beuermann, K., Dreizler, S., Hessman, F. V., & Deller, J. (2012). A&A, 543, A138.

References 95

Charpinet, S., Fontaine, G., Brassard, P., & Dorman, B. (1996). ApJ, 471, L103.

Charpinet, S., Fontaine, G., Brassard, P., Chayer, P., Rogers, F. J., Iglesias, C. A., et al. (1997). *ApJ*, 483, L123.

Charpinet, S., Van Grootel, V., Fontaine, G., Green, E. M., Brassard, P., Randall, S. K., et al. (2011). *A&A*, *530*, A3.

Charpinet, S., Fontaine, G., Brassard, P., Green, E. M., Van Grootel, V., Randall, S. K., et al. (2011). *Nature*, 480, 496.

Claret, A. (2004). A&A, 428, 1001.

Dhillon, V. S., Marsh, T. R., Stevenson, M. J., Atkinson, D. C., Kerry, P., Peacocke, P. T., et al. (2007). *MNRAS*, 378, 825.

Dupret, M. A. (2001). A&A, 366, 166.

Dupret, M. -A., De Ridder, J., Neuforge, C., Aerts, C., & Scuflaire, R. (2002). A&A, 385, 563.

Dupret, M. -A., De Ridder, J., De Cat, P., Aerts, C., Scuffaire, R., Noels, A., et al. (2003). *A&A*, 398, 677.

Dziembowski, W. (1977). Acta Astronautica, 27, 203.

Eggleton, P. P. (1971). MNRAS, 151, 351.

Fontaine G., Brassard P., Charpinet S., Green E. M., Chayer P., Randall S., et al. (2006). In *Proceedings of SOHO 18/GONG 2006/HELAS I, Beyond the spherical Sun (Vol. 624) of ESA Special Publication, Asteroseismology of hot B subdwarf stars: a brief overview.* 

Fontaine, G., Brassard, P., Charpinet, S., Green, E. M., Chayer, P., Billères, M., et al. (2003). *ApJ*, 597, 518.

Fontaine, G., Brassard, P., Charpinet, S., & Chayer, P. (2006). *Mem. Societa Astronomica Italiana*, 77, 49.

Green, E. M., Fontaine, G., Reed, M. D., Callerame, K., Seitenzahl, I. R., White, B. A., et al. (2003). *ApJ*, 583, L31.

Green, E. M., Fontaine, G., Hyde, E. A., For, B., & Chayer, P. (2008). ASPC, 392, 75.

Grevesse N., Noels A. (1993). In N. Prantzos, E. Vangioni-Flam & M. Casse (Eds.), *Origin and Evolution of the Elements Cosmic abundances of the elements* (pp. 15–25).

Van Grootel, V., Charpinet, S., Fontaine, G., Brassard, P., Green, E. M., Randall, S. K., et al. (2010). *ApJ*, 718, L97.

Han, Z., Podsiadlowski, P., Maxted, P. F. L., Marsh, T. R., & Ivanova, N. (2002). MNRAS, 336, 449.

Han, Z., Podsiadlowski, P., Maxted, P. F. L., & Marsh, T. R. (2003). MNRAS, 341, 669.

Heber, U. (2009). ARA&A, 47, 211.

Heyrovský, D. (2007). ApJ, 656, 483.

Hu H. (2009). PhD thesis, University of Leuven and University of Nijmegen.

Hu, H., Glebbeek, E., Thoul, A. A., Dupret, M., Stancliffe, R. J., Nelemans, G., et al. (2010). A&A, 511, A87.

Hu, H., Dupret, M., Aerts, C., Nelemans, G., Kawaler, S. D., Miglio, A., et al. (2008). *A&A*, 490, 243.

Hu, H., Nelemans, G., Aerts, C., & Dupret, M. (2009). A&A, 508, 869.

Hu, H., Tout, C. A., Glebbeek, E., & Dupret, M. -A. (2011). MNRAS, 418, 195.

Iglesias, C. A., & Rogers, F. J. (1996). ApJ, 464, 943.

Jeffery, C. S., & Saio, H. (2006). MNRAS, 372, L48.

Kawaler, S. D. (2010). Astronomische Nachrichten, 331, 1020.

Kilkenny, D., Koen, C., O'Donoghue, D., & Stobie, R. S. (1997). MNRAS, 285, 640.

Maxted, P. F. L., Heber, U., Marsh, T. R., North, R. C. (2001). MNRAS, 326, 1391.

Michaud, G., Richer, J., & Richard, O. (2011). A&A, 529, A60.

Østensen, R. H. (2009). Communications in Asteroseismology, 159, 75.

Østensen, R. H. (2010). Astronomische Nachrichten, 331, 1026.

Pablo, H., Kawaler, S. D., & Green, E. M. (2011). ApJ, 740, L47.

Pablo, H., Kawaler, S. D., Reed, M. D., et al. (2012). MNRAS, 422, 1343.

Podsiadlowski P., Han Z., Lynas-Gray A. E., Brown D. (2008). In C. S. Heber, Jeffery, & R. Napiwotzki (Ed.), Hot subdwarf stars and related objects (Vol. 392, p. 15). Astronomical Society of the Pacific Conference Series, Hot Subdwarfs in Binaries as the Source of the Far-UV Excess in Elliptical Galaxies.

Randall, S. K., Fontaine, G., Brassard, P., & Bergeron, P. (2005). ApJS, 161, 456.

Silvotti, R., Schuh, S., Janulis, R., et al. (2007). Nature, 449, 189.

Soker, N., & Harpaz, A. (2000). MNRAS, 317, 861.

Townsend, R. H. D. (2003). MNRAS, 343, 125.

Watson, R. D. (1987). Proceedings of the Astronomical Society of Australia, 7, 38.

Watson, R. D. (1988). Ap&SS, 140, 255.

Werner K., Deetjen J. L., Dreizler S., Nagel T., Rauch T., Schuh S. L. (2003). In I. Hubeny, D. Mihalas, K. Werner (Eds.), Stellar Atmosphere Modeling, (Vol. 288, p. 31) of Astronomical Society of the Pacific Conference Series, Model Photospheres with Accelerated Lambda Iteration.

## Chapter 7 MAIA: The Mercator Advanced Imager for Asteroseismology

**Abstract** MAIA, the Mercator Advanced Imager for Asteroseismology, was developed by the Institute of Astronomy of the KU Leuven and was installed at the 1.2-m Mercator telescope in 2012. MAIA is an imager that can observe at high cadence in three passbands simultaneously. It was built around three large frametransfer CCDs that were originally made in the framework of the later cancelled ESA space mission Eddington. In this Chapter we describe the science goals of the instrument, we give a brief overview of the design and the operational aspects. We also present the results of efficiency measurements for the system, as well as the first science data taken with the instrument.

#### 7.1 Introduction

#### 7.1.1 The Starting Point for the MAIA Camera Project

The Institute of Astronomy (IvS) of the KU Leuven has finished the development of a new camera: the Mercator Advanced Imager for Asteroseismology (MAIA). MAIA is a multi-colour camera that can observe in 3 colour bands simultaneously, at high cadence, and with a relatively large field of view. It was installed at one of the Nasmyth foci of the 1.2-m Mercator telescope in the Spring of 2012, where it will be permanently available to the observers. A simple change of the position of the motorized tertiary mirror allows one to switch between MAIA and the HERMES spectrograph (Raskin et al. 2011) in a few minutes. The optical and mechanical design of MAIA are described in detail in Chap. 2 of Vandersteen (2012) and Raskin et al. (2013).

The history of the instrument started after the European Space Agency (ESA) cancelled its Eddington Space Mission in 2003. The IvS received 5 of the satellite's prototype e2v frame-transfer CCDs on permanent loan from ESA, on the condition that they would be used for the asteroseismology project defined by C. Aerts and submitted to ESA. In 2010, Mercator's single-channel Merope imager was replaced by the Merope II imager. Merope II was equipped with an Eddington CCD for the instrument team to become familiar with the CCDs that were designed to be operated in space for high-precision photometry.

In the meantime, Merope II has been decommissioned and its CCD is, together with two other Eddington CCDs, installed in MAIA. The remaining two Eddington CCDs have been used as engineering CCDs. Neither CCD ever gave a useful full-frame image, with one device showing half the image the other no image. Probably they underwent too much damage during the tests that were performed by E2V to determine if they would be suitable to be flown on the Eddington spacecraft.

#### 7.1.2 Scientific Motivation

Although MAIA can be used for a variety of astrophysical studies, it was mainly built to do asteroseismology of subdwarf B stars (sdBs). Asteroseismology has proven to be an unrivalled tool to study the interiors of stars, and can also be used to determine important global stellar parameter such as mass, radius and age.

The main observational input to asteroseismic studies is a set of observed pulsation frequencies of a star. These periodic signals can be detected in both photometric data, where the light intensity is modulated, and in spectroscopy, where variations are seen in spectral line shapes, depths and offsets from the rest wavelength. In principle, one can determine the stellar structure of pulsating stars by comparing observed pulsation frequencies with theoretical frequency spectra of stellar models. In practice, degeneracies often lead to multiple solutions, certainly when only a few pulsation modes are observed.

One way to break the degeneracy is to identify the spherical degree l of the modes from observations. This can be achieved from high-resolution spectroscopic data by a detailed study of the line shape variations. This has been achieved for modes in pulsators of several different classes (see e.g. Aerts 1996, for a  $\beta$  Cep star example but requires spectra with a very high signal to noise ratio (S/N  $\sim$  200). Unfortunately, sdBs are usually relatively faint and show p-mode pulsations with periods of the order of minutes. Obtaining high-resolution spectroscopy at sufficiently high cadence to resolve the pulsation frequencies often proves to be impossible, with the notable exception of the study of large-amplitude radial-mode sdB pulsator Balloon 090100001 by Telting et al. (2008). Other in-depth studies based on high-quality data only achieved partial mode identifications, as for example in the study of the UVES spectra obtained with an 8.2-m VLT telescope by Vučković et al. (2009). Photometric mode identification through amplitude ratios of pulsation signals in different colour bands, as we introduced in Sect. 6.4, is often more appropriate for compact pulsators.

#### 7.1.3 Requirements and Design

As explained in Chap. 6, we have set up methods to compute synthetic amplitude ratios for the non-adiabatic pulsation modes computed for a grid of sdB models.

7.1 Introduction 99

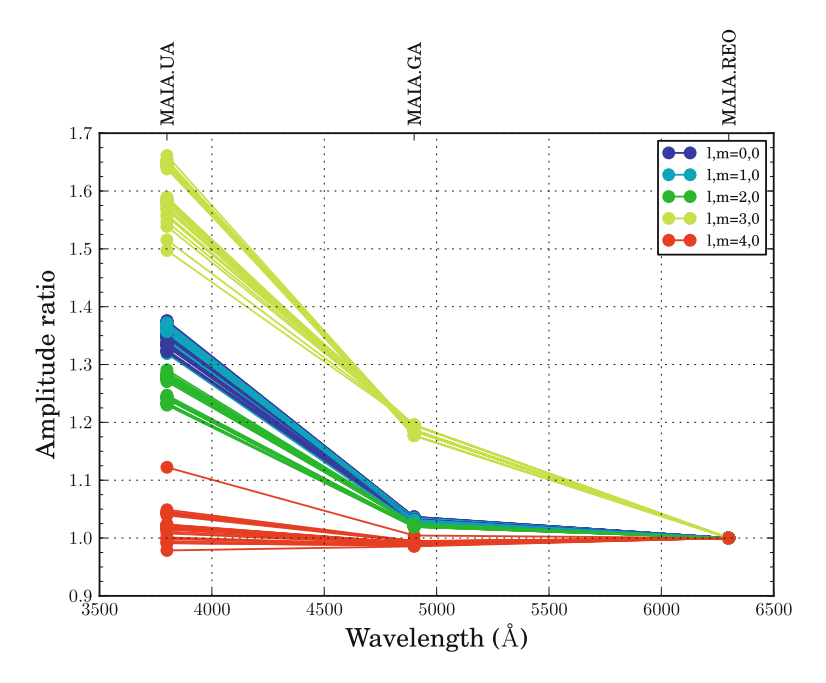


**Fig. 7.1** Illustration of expected *p*-mode amplitude ratios for MAIA. The modes and models are the same as those shown in Fig. 6.9 but in this case the MAIA filters have been used to compute the amplitude ratios

As an illustration, we have computed the amplitude ratios that can be expected for the same models as those shown in Sect. 6.4 but for MAIA's response curves instead of the Johnson filters. The results are shown for the typical p-mode pulsator in Fig. 7.1 and for the g-mode pulsator in Fig. 7.2. These Figures illustrate the importance of a very blue (u) filter for the study of sdB pulsations: it offers the highest contrast between modes of different spherical degrees. Unfortunately, while sdBs are fairly bright in u, most (cooler) field stars are not, and the quantum efficiency of the CCDs is relatively poor in u. In order to have a good chance to have a comparison star available that is bright enough in u, one of the key requirements of MAIA is a large field of view while still keeping the pixel scale fine enough for an average seeing of  $\sim$ 1 arcsec. Since typical p-mode pulsators have pulsation periods on the order of minutes, the camera also has to be able to observe at a cadence of on the order of 10 s.

In summary, the main scientific requirements for MAIA were the following:

- be able to observe in at least 3 different colours simultaneously, including a u channel
- reach a cadence of a few seconds with reasonable dead-time, and
- provide a relatively large field of view at a pixel scale suitable for an average seeing.

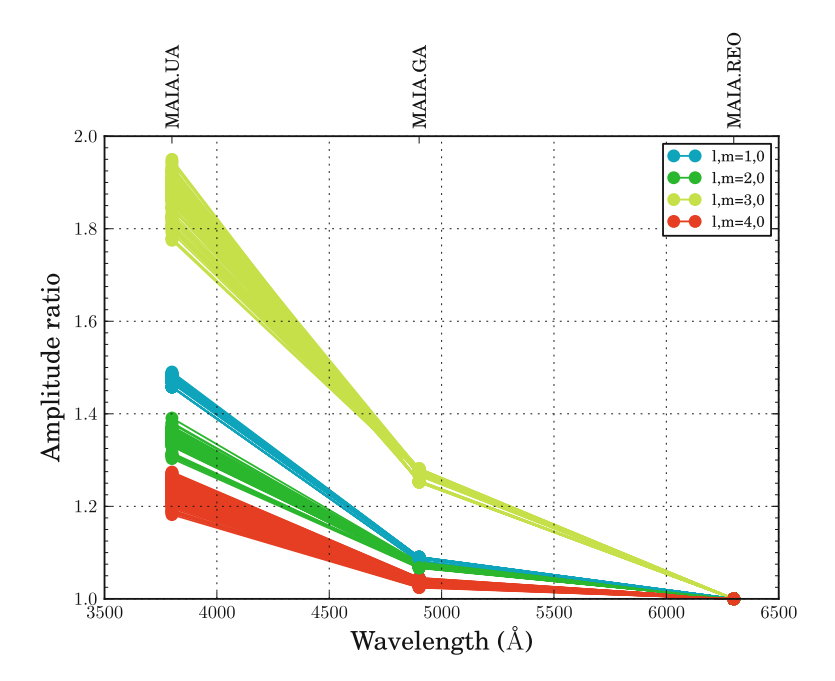
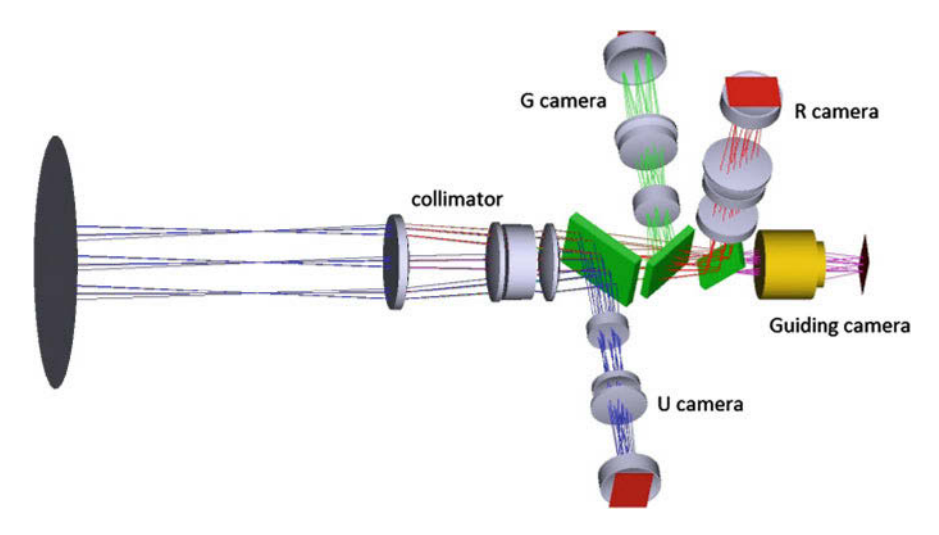


Fig. 7.2 Illustration of expected g-mode amplitude ratios for MAIA. The modes and models are the same as those shown in Fig. 6.10

From a technical point of view, the design had to be compliant with the Eddington CCDs we had at our disposal. These CCDs are 2k by 6k pixels large. Half of the silicon is used as a frame transfer buffer which allows MAIA to start taking a new image while the previous one is still being read out. A full unbinned frame takes 295 ms to shift from the image area to the frame transfer butter, and about 40 s to read out. By windowing and binning, this can be reduced to only a few seconds, which is short enough to resolve sdB pulsation modes. Multiple windows can be defined around stars of interest, so that data of comparison stars that are imaged at different parts of the CCD can be obtained without the need to read out a large part of the image. The three cameras have iris shutters that allow one to operate the camera in standard (not frame transfer) mode. In frame transfer mode, the shutters never close. The optical design was developed such that the 2k by 3k images offer a large field of view of 9.4 by 14.1 arcmin at a pixel scale of 0.28 arsec/pixel. This will allow users of the instrument in most cases to obtain data of a comparison star that is bright enough in the *u* filter.

Figure 7.3 shows MAIA's optical design. The light from the telescope that enters MAIA is split into three colour components by a series of dichroics, and images in each of the colours are recorded using a different CCD. This way, simultaneous observations can be obtained in MAIA's r, g and u colour channels. A picture of MAIA mounted on the Mercator telescope is shown in Fig. 7.4. For a more detailed

7.1 Introduction 101



**Fig. 7.3** The MAIA optics. Light enters the instrument from the *left* and after passing through the collimator, it passes a series of dichroics that send the light of different colours to the three science detectors and the remaining light to the guiding camera. Figure taken from Vandersteen (2012)

description of the optical and mechanical design, see Chap. 2 of Vandersteen (2012) and Raskin et al. (2013).

The response curves of the different channels, which include the optical elements and the filters, are shown in Fig. 7.5. The throughput in the u channel is affected by the coating of the CCDs, which is not optimised for near-UV light since the Eddington mission was designed to observe in white light.

## 7.1.4 Comparison with Similar Instruments

Multi-channel CCD images are not common. The idea to build MAIA was inspired by ULTRACAM, which is a 3-channel camera operated by the universities of Warwick and Sheffield (Dhillon et al. 2007). Compared to MAIA, it uses smaller 1k by 2k frame transfer CCDs and has a smaller field of view of 5 by 5 arcmin when mounted on the William Herschel Telescope or 2.5 by 2.5 arcmin when mounted on the Melipal Very Large Telescope (VLT). ULTRACAM can, however, achieve frame rates of several hundred frames per second, which is not possible with MAIA. ULTRACAM has been used for research on a variety of high-speed astrophysics topics, including sdB asteroseismology (e.g. Jeffery et al. 2005; Aerts et al. 2006; Silvotti et al. 2010).

Another multi-channel camera that is currently in operation is the Bonn University Simultaneous CAmera (BUSCA), installed at the 2.2-m telescope at Calar Alto. BUSCA is a four-channel camera with a 12 by 12 arcmin field of view (Reif et al. 1999). Its 4k by 4k CCDs have, however, no frame transfer capabilities. A full

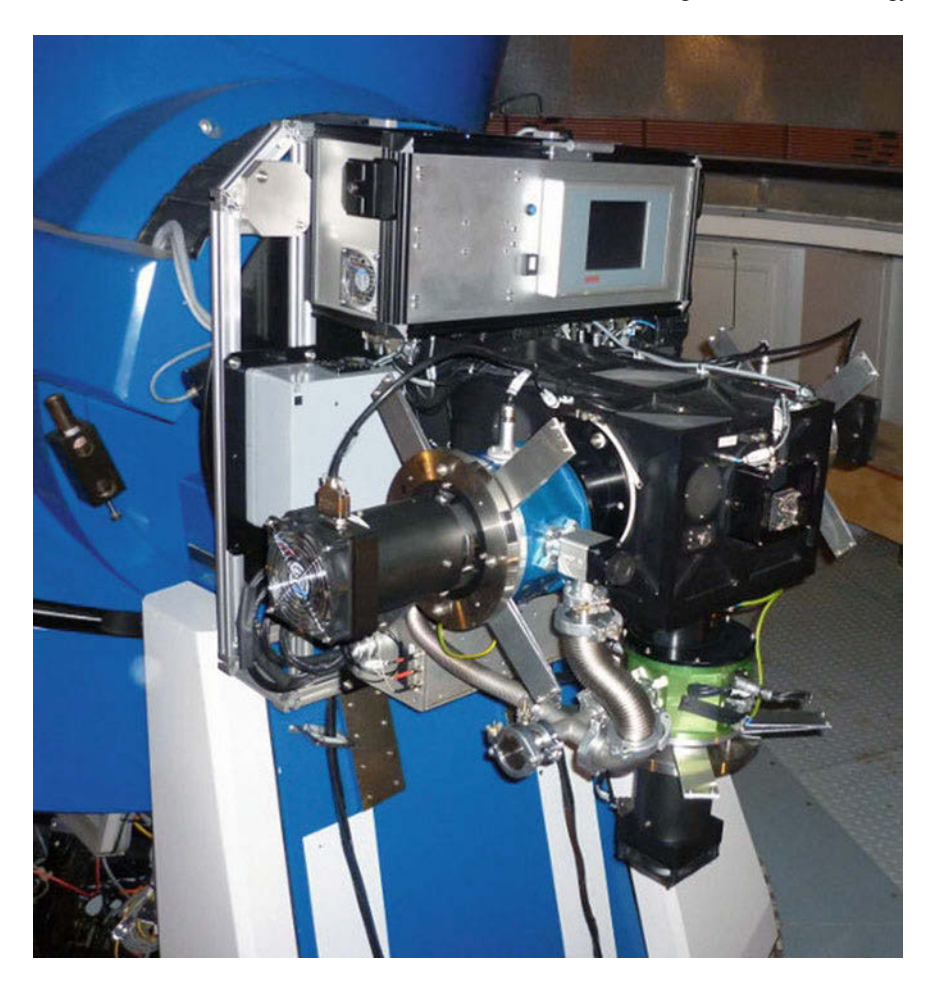


**Fig. 7.4** MAIA installed at a Nasmyth focus of the Mercator telescope. The instrument consists of a *black* optics box, three cryostats (the *blue* and *green* coloured ones are visible on this picture, the *red* one sits in the back). The stirling coolers (*black* with visible fan) are mounted on springs to prevent the instrument and telescope from picking up their vibrations

readout of the CCDs takes 2 min when using a  $2 \times 2$  binning. By carefully defining windows around the stars of interest, this readout time can be reduced, but typical dead-times between two exposures are on the order of  $10-20 \, \mathrm{s}$ . Although the camera has a large field of view and a u channel, these long dead-times make it much less suitable to observe fast pulsators than MAIA. It has, e.g., been used to study RR Lyra variables (de Boer and Maintz 2010), to search for ZZ Ceti pulsators using color indices (Silvotti et al. 2005) and as part of a multi-site campaign to observe the g-mode pulsations in PG 1716 + 426 (Reed et al. 2004).

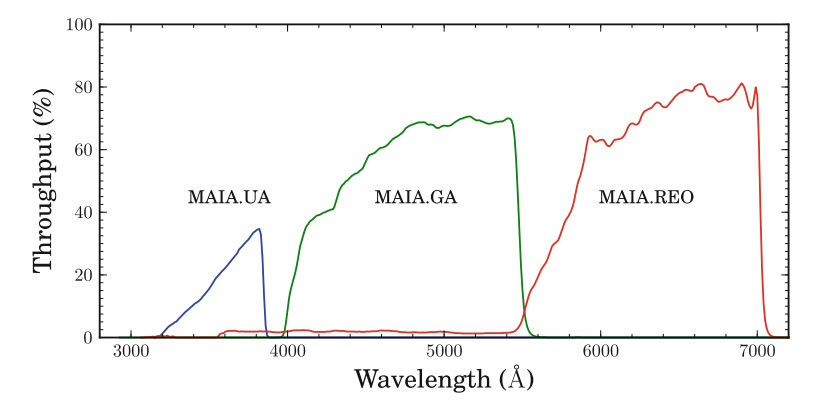


Fig. 7.5 Response curves of MAIA in the three different channels and with the currently installed filters: an Astrodon u (MAIA.UA), an Astrodon g (MAIA.GA) and an Edmund r (MAIA.REO) filter. The atmospheric transmission and the reflectivity of the telescope mirrors are not taken into account in these curves

## 7.2 Data Reduction Pipeline

As part of this thesis, a dedicated data reduction software package for MAIA data has been written in Python. This pipeline can be run both in real time as observations come in, or on a full night of data. Parameters that are used by the pipeline can be changed in a settings file and can be overruled by command line options.

A typical pipeline run starts by indexing the available data of a given night. The pipeline recognizes images that suffer from read-out issues, which occurred several times per night during the first commissioning runs but are now mostly resolved. Such images, as well as images that are on a blacklist that the user can adapt, are omitted.

After indexing the frames that are available at the start of the pipeline run, the pipeline automatically selects flatfields to create a masterflat. The user can set, for each camera independently, whether sky—or domeflats should be used. Limits can also be set for the signal that a flatfield should have in order to be acceptable. Flatfields that have a too low signal, or that have count levels that are too close to saturation, will be rejected. The flats are selected for each camera independently, which is necessary since the typical count levels in u are much lower than in g or r. Therefore, images taken simultaneously in the three channels will seldomly all be useful. Masterflats are produced by taking the median image of all suitable images, and dividing by the mean count level in a region set in the settings file. Masterflats are created for the three channels and for all binning settings for which flatfields are available.

The next step involves the processing of the science frames. The bias level is subtracted from each frame using a constant which is determined from the overscan region of each frame. The image is then divided by the masterflat, and is saved together with a flag image. This boolean image indicates which of the pixels are to

be used to extract the stars and which are not. Known bad pixels (bad spots and bad columns on the CCD) are flagged in this image, as well as the overscan regions and regions that are not read out when the detectors are operated in a windowed mode.

Finally, SExtractor (Bertin and Arnouts 1996) is used to extract the fluxes of all the stars in the observed field. SExtractor is the only hard software dependency of the data reduction software besides Python and a set of Python libraries that are very often used for astronomical applications (pyfits, pylab, numpy and scipy). SExtractor uses the mask image to avoid regions were no data is available, or where data cannot be used. It automatically interpolates over bad pixels and columns. All SExtractor settings are available and can be changed in a separate settings file. The output of SExtractor is a .fits file which contains the positions of the identified sources, their fluxes determined using different extraction methods including aperture photometry, the full-width half-maximum of the sources, their ellipticity, the background measured at the centroid positions, et cetera. The pipeline propagates important header information such as the time of the observation, the exposure time and the coordinates of the target to these output files.

Light curves can then be produced using the SExtractor output files. The user of the pipeline has to identify the target and reference stars on one frame, which the pipeline then matches to the other frames to follow the evolution of the flux in time. The selection of target and reference stars can already be performed at the telescope during the target acquisition phase to allow for a fully automated reduction afterwards.

### 7.3 Instrument Calibration

## 7.3.1 Flatfields

Flatfield images (i.e. evenly illuminated images) are used in the data reduction process to calibrate out differences in the response of the pixels in a CCD. Such differences can, e.g., be caused by dust on the CCD, by imperfections in the thinning of the CCD or the coating applied to its surface. At Mercator, a LED-illuminated screen is available in the dome to take dome flatfields. Another option is to take flats on sky during evening or morning twilight. Dome flatfields can be taken with the dome closed, in the afternoon or at night at times of bad weather. They are thus easier to obtain, but a careful comparison with sky flats is needed to ensure that dome flats are equally suitable for the data reduction. While skyflats are taken with a well behaved continuum light source (the sunlight on the sky), dome flats can suffer from an uneven illumination due to the LED arrangement and from differences in the measured pixel responses due to the distinct wavelengths at which the LEDs emit light.

To check for possible uneven illumination effects, we have rotated the instrument using the derotator and compared dome flats taken at various angles. No significant differences could be found, which indicates that the illumination is uniform. This is

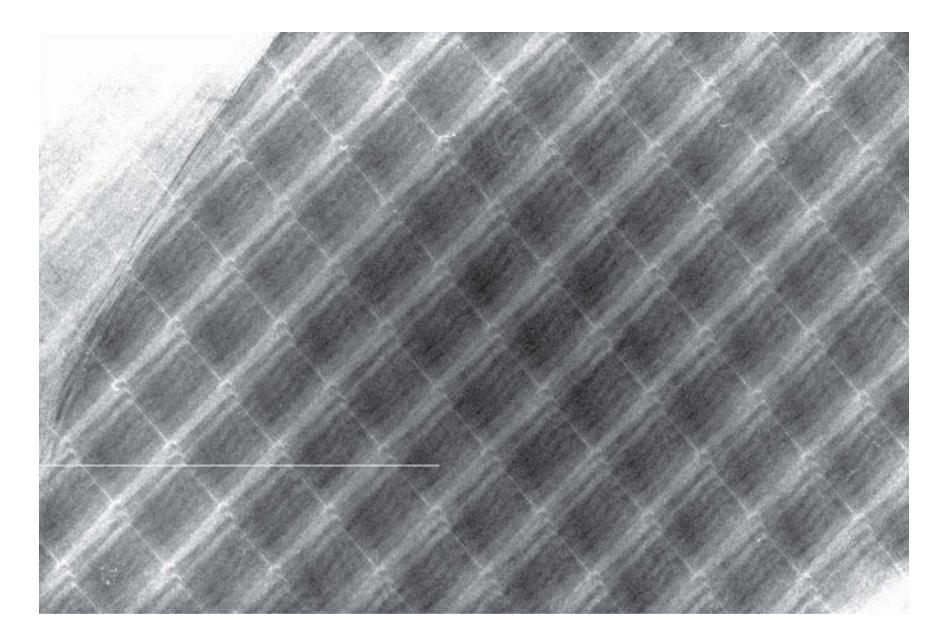


Fig. 7.6 A u channel dome flat divided by a u channel skyflat. The response of the pixels is different depending on the colour of the light source. The colour scale is linear, with a black to white difference of 20% of the mean light level

explained by the fact that the LEDs are placed around the top ring of the telescope and because an image taken of the screen that is only a few meters away from the primary mirror is highly defocused. Any structure in the screen or the illumination is therefore blurred to a large extent.

The colour difference between the skylight and the dome LEDs unfortunately has a notable effect on the flats. While dome flats and sky flats are nearly indistinguishable in the r and g channels, the flats taken in u are different. This is illustrated in Fig. 7.6, where a u dome flat divided by a u sky flat is shown. If the response to both light sources would be identical, the image would be constant, apart from noise. In this case, however, pixel response differences of more than 20% are seen. Skylight is closer to what is observed from sun-like stars than the LED light, but of course also not like the spectrum of a hot subdwarf, which typically has an effective temperature between 20,000 and 30,000 K. Nevertheless, skyflats are to be used whenever they are available to calibrate the u channel. For the g and r channels, both skyflats and domeflats are viable options.

In the original design, the shutters of the three cameras operate simultaneously. Since the images in the r and g channels are saturated when a flat is taken with  $\sim$ 15,000 counts in u, differential shutters were installed in March 2013 so that the shutters of the r and g cameras can stay closed when u flats are obtained.

### 7.3.2 System Throughput

To measure the efficiency of the system and to be able to estimate exposure times for observations, we determined the zeropoints of the instrument in the three channels. The zeropoint is defined as the magnitude of an object that would result in a signal of 1 count per second, outside the atmosphere. Zeropoints depend not only on the instrument efficiency and the filterset that is being used, but also on the telescope. For example, when dust accumulates on the mirrors of the telescope, the efficiency of the system will drop and the zeropoints, since they are expressed in magnitudes, will rise.

In order to determine the zeropoint of a given system, one has to observe a series of standard stars (spanning a range of altitudes on the sky) with known magnitudes in the given filter. Such a series of observations is also known as a skydip and should be performed in photometric sky conditions. The zeropoint can then be determined by least-squares optimization of the following equation:

$$m_{\text{cat},\lambda} - m_{\text{obs},\lambda} = Z_{\lambda} - k_{\lambda} F_{z},$$
 (7.1)

in which  $Z_{\lambda}$  is the zeropoint for the given filter,  $k_{\lambda}$  the first-order extinction coefficient,  $F_z$  the airmass of the targets at the time of the observations,  $m_{\text{cat},\lambda}$  the catalogued magnitudes of the stars for the given filter, and  $m_{\text{obs},\lambda}$  the observed instrumental magnitudes computed as  $-2.5 \log$  (counts/s). The airmass reflects the optical path length of the observed light through the Earth's atmosphere. The value is defined as 1 at zenith and increases to about  $\sim$ 40 at the horizon. We have computed the airmass using the approximate formula by Pickering (2002)

$$F_z = \frac{1}{\sin(h + 244/(165 + 47h^{1.1}))},$$
(7.2)

in which h is the altitude (in degrees) of the target at the time of the observation.

The stars we observed on 2013/02/02 to determine the zeropoints are spectrophotometric standard stars selected by the Isaac Newton Group of Telescopes (ING). For all of them, spectral energy distributions are available, expressed in AB magnitudes. We have integrated these magnitudes over the response curves of the three MAIA channels, shown in Fig. 7.5, to determine the value  $m_{\rm cat}$  used in Eq. (7.1). The stars we have used and the sources of their spectral energy distributions are listed in Table 7.1.

In Fig. 7.7, the fit of Eq. (7.1) to the values of  $m_{\text{cat},\lambda} - m_{\text{obs},\lambda}$  as a function of airmass ( $F_z$ ) is shown. The derived zeropoints and extinction coefficients are listed in Table 7.2. Since the aluminum coating of the telescope's mirrors was five years old at the time of the measurement, we expect that the zeropoints with a fresh coating will be  $\sim$ 0.25 mag higher.

The zeropoints in the r and g channels are comparable to the values that were measured for the Geneva R and Geneva G filters with the MEROPE instrument.

ING identifier	Alternative identifier	Reference
SP0105+625	Hiltner 102	Stone (1977)
SP0437+085	HZ 15	Stone (1977)
SP0642+021	Hiltner 600	Massey et al. (1988)
SP0644+375	He 3	Oke (1974)
SP0934+554	PG0934+554	Massey et al. (1988)
SP0958-073	GD 108	Oke (1990)
SP1204+119	Feige 56	Stone (1977)

Table 7.1 Standard stars observed on 2013/02/02 to determine the zeropoint of the different channels

The first and second columns give the ING identifier and an alternative name, respectively. The third column gives the source of the spectral energy distributions we have used

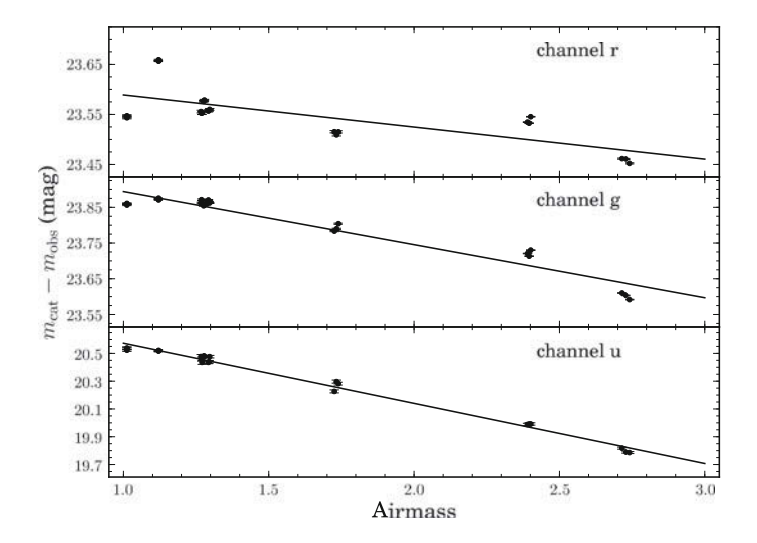
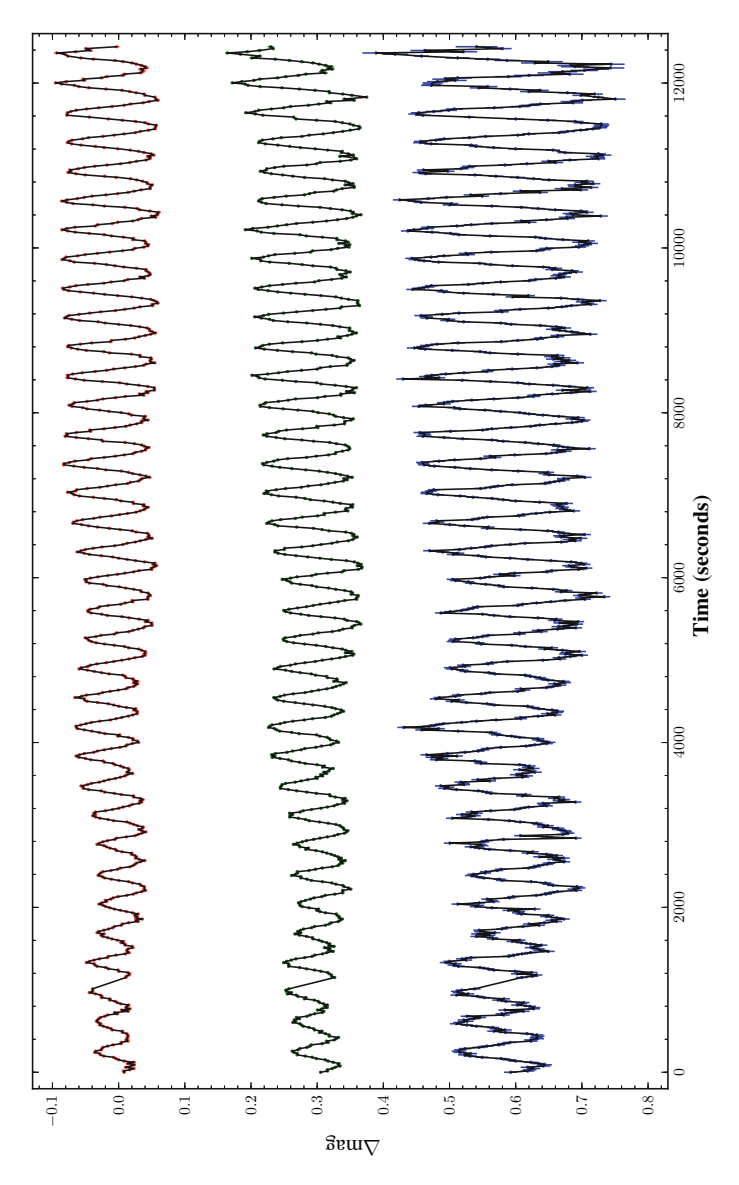


Fig. 7.7  $m_{\rm cat}-m_{\rm obs}$  in the three MAIA channels for standard stars observed at different elevations. The error bars only reflect the uncertainty on the extracted fluxes, but do not take into account fluctuations due to the sky conditions or uncertainties on the catalogue magnitudes, which are likely to be dominated by uncertainties in the characterization of the instrument's response curves. The *line* represents the fit of the linear relation shown in Eq. (7.1)

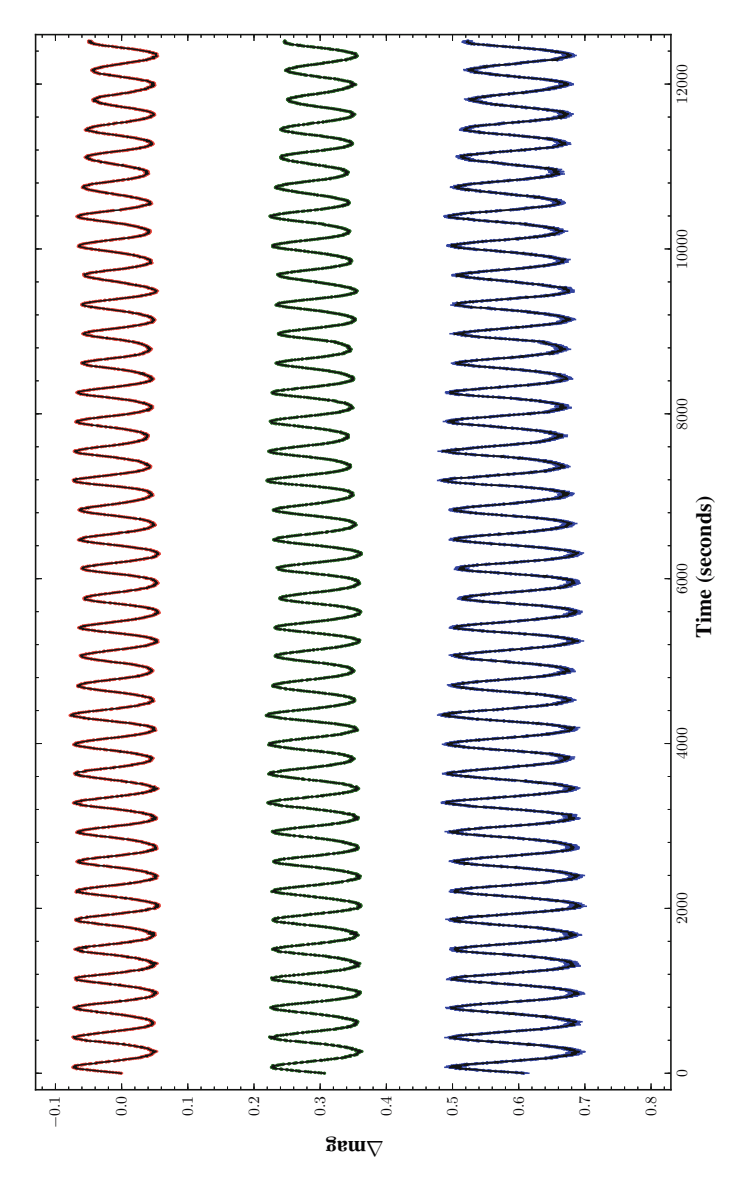
**Table 7.2** Zeropoints  $(Z_{\lambda})$  and extinction coefficients  $(k_{\lambda})$  for the different MAIA channels, determined from observations of standard stars taken on the night of 2013/02/02

Channel	$Z_{\lambda}$ (mag)	$k_{\lambda}$ (mag/airmass)
и	21.0	0.43
g	24.0	0.15
r	23.7	0.06



**Fig. 7.8** MAIA light curve of Balloon taken with 15 s integration times. The different colour bands (from *top* to *bottom*, r in red, g in green and u in blue) are offset by 0.2 mag for clarity. The amplitude of the variations in u is clearly higher than the variation in g and g

The efficiency in u is one magnitude lower than for the Geneva U band. We expect that this is mainly caused by poor performance of the anti-reflection coating on the CCD, which is not optimised for this wavelength regime. One option to increase the sensitivity in u would be to use a filter that extends further towards the red end. While extra red photons are not helpful for the determination of amplitude ratios since it



 $\textbf{Fig. 7.9} \quad \text{Similar to Fig. 7.8 but showing an ULTRACAM @ WHT light curve of Balloon taken with 3.4s integration times } \\$ 

reduces their contrast for modes with different spherical degrees, it will be useful for other projects for which a higher signal-to-noise ratio of the observations is preferred over a larger colour contrast between the u and g channels.

Band	MAIA (mmag)	ULTRACAM (mmag)
r	$65.1 \pm 1.1$	$58.0 \pm 0.4$
g	$74.4 \pm 1.3$	$63.2 \pm 0.4$
и	$129.4 \pm 2.6$	$90.1 \pm 0.6$
u/r	$1.99 \pm 0.05$	$1.553 \pm 0.015$
g/r	$1.14 \pm 0.03$	$1.090 \pm 0.010$

 Table 7.3 Pulsation amplitudes and amplitude ratios for Balloon

The pulsation amplitudes are determined by fitting a sine curve at the main pulsation frequency  $(2,807.5\,\mu\,Hz)$  to light curve sections of  $2,000\,s$  observed with MAIA and ULTRACAM. These values are only given for illustrative purposes since a longer dataset, in which the different pulsations modes are resolved, is needed to determine reliable pulsation amplitudes

Since the zeropoints are variable in time, as explained above, observers will be requested to perform a skydip at least once during every MAIA run. A fixed list of standard stars to be used is currently being defined, which will allow the data reduction pipeline in the future to automatically pick up the skydip observations in order to monitor the zeropoints.

### 7.4 First Results

## 7.4.1 Light Curve of Balloon 090100001

During the commissioning run in October 2012, we obtained a 3.5h light curve of the high-amplitude hybrid sdB pulsator Balloon 090100001 (hereafter referred to as Balloon Oreiro et al. 2004). This target is interesting because we have comparison data available taken with ULTRACAM mounted on the 4.2-m William Herschel Telescope (WHT).

The MAIA data of Balloon were taken with 15 s integration times and are shown in Fig. 7.8. Since the mirror surface of the WHT is about 12 times larger than that of Mercator, shorter integration times of 3.4 s were used for the ULTRACAM observations. A part of the ULTRACAM data, with the same timespan as the MAIA dataset, is shown in Fig. 7.9. The ULTRACAM observations have been reduced with the dedicated data reduction pipeline (Dhillon et al. 2007).

It is clear from the figures that the pulsation amplitude in the u band is larger than in the other two bands. The target's main pulsation mode at 2,807.5  $\mu$ Hz (356 s) is known to be the fundamental radial mode (Baran et al. 2005). Unfortunately, the target has strong pulsation modes at 2,823.2, 2,824.8 and 2,823.3  $\mu$ Hz (Baran et al. 2008), which are close to the fundamental. Beating between these modes and the fundamental mode probably explains the reduced variability amplitude at the start of the MAIA observations.

For illustrative purposes, Table 7.3 lists the amplitudes of the pulsation signal in the different colour bands for both instruments. These amplitudes were determined by fitting a sine curve at the main pulsation frequency to light curve sections of

7.4 First Results

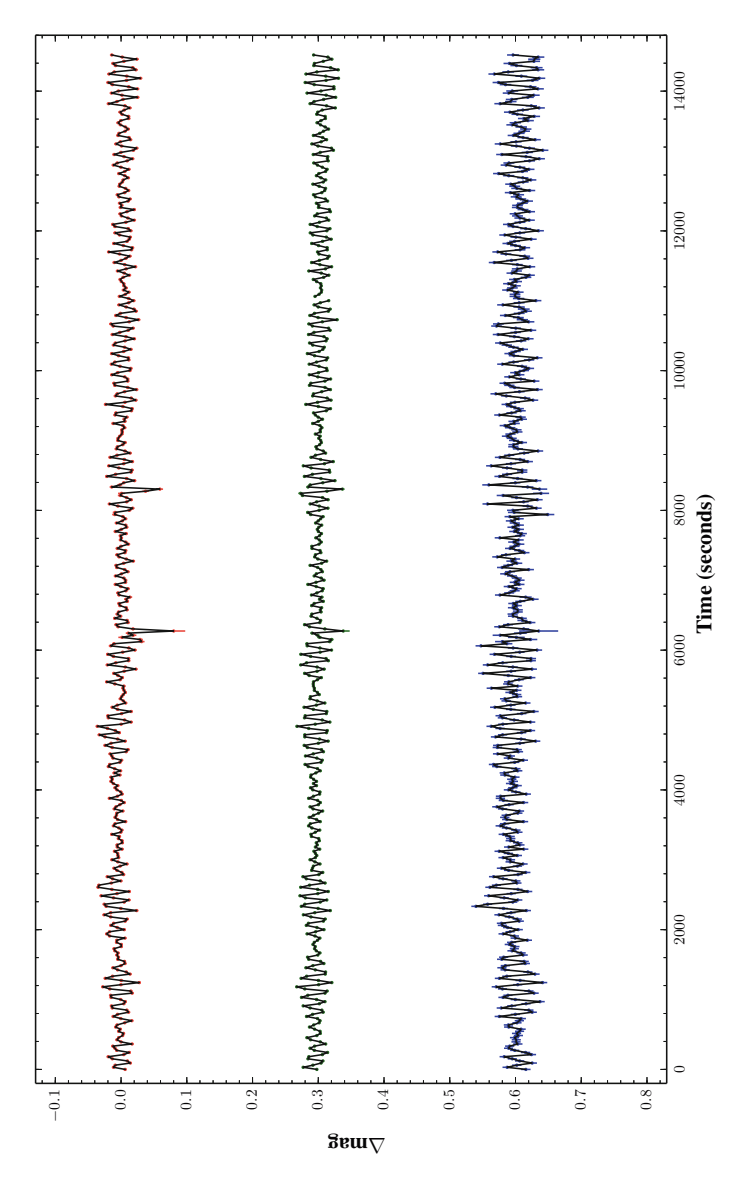


Fig. 7.10 MAIA light curve of KY UMa obtained in the night of 24 April 2013, which had the best weather conditions of all nights during which we observed this target. The different colour bands (from *top* to *bottom*, r in red, q in green and u in blue) are offset by 0.2 mag for clarity

 $2,000 \, \mathrm{s}$ . For MAIA, we took the part of the light curve were the amplitude is highest, between  $10,000 \, \mathrm{and} \, 12,000 \, \mathrm{s}$  on Fig. 7.8, and for ULTRACAM we used the section between  $2,000 \, \mathrm{and} \, 4,000 \, \mathrm{s}$  on Fig. 7.9. The results show that, in the light curves observed with both instruments, the amplitudes is smallest in the r band, larger in g and largest in u, exactly as expected for an  $l=0 \, p$ -mode. Obviously, in order

Frequency		Amplitude (ppt)		Amplitude ratio			
	$d^{-1}$	μHz	r	g	и	g/r	u/r
$f_1$	601.426(4)	6960.95(4)	$8.9 \pm 0.6$	$9.9 \pm 0.6$	$12.3 \pm 0.8$	$1.11 \pm 0.10$	$1.38 \pm 0.13$
$f_2$	674.555(5)	7807.35(6)	$6.8 \pm 0.6$	$6.9 \pm 0.6$	$8.6 \pm 0.8$	$1.01 \pm 0.12$	$1.26 \pm 0.16$
$f_3$	647.089(8)	7489.46(9)	$3.8 \pm 0.6$	$5.0 \pm 0.6$	$4.7 \pm 0.8$	$1.32 \pm 0.26$	$1.21 \pm 0.28$
$f_4$	580.706(11)	6721.13(13)	$3.5 \pm 0.6$	$3.5 \pm 0.6$	$4.6 \pm 0.6$	$1.00 \pm 0.24$	$1.37 \pm 0.33$

**Table 7.4** Pulsation amplitudes (in parts per thousand) and amplitude ratios for the 4 dominant pulsation frequencies observed in KY UMa

The frequency value that is given is determined from the g-band observations and lies within  $1\sigma$  from the one found in the other two bands

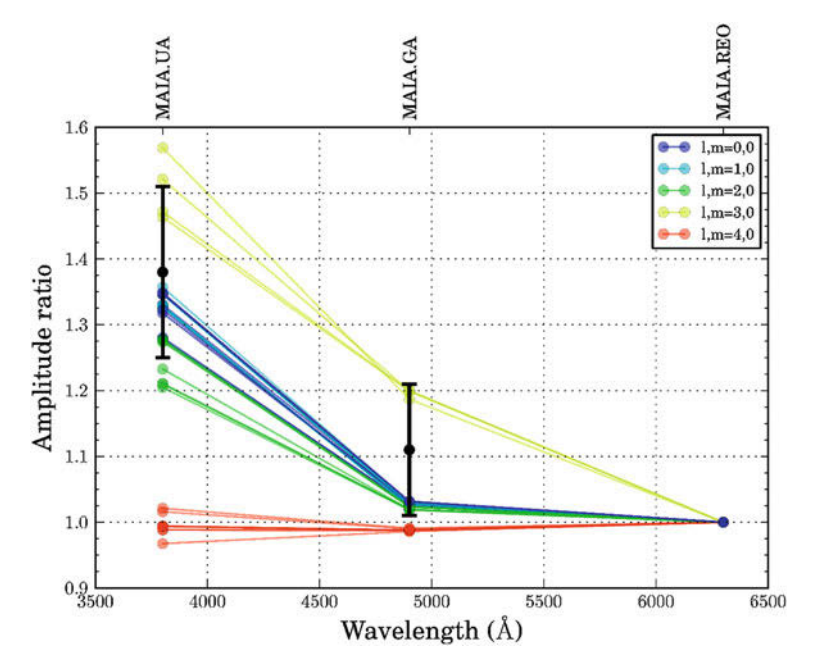


**Fig. 7.11** Measured amplitude ratios with R as the reference band for  $f_1 = 6,960.95(4) \,\mu\text{Hz}$  (black) and model predictions, similar to Fig. 7.1 but for models with properties similar to KY UMa

to determine reliable amplitudes and amplitude ratios, a longer dataset in which the different pulsation modes are resolved, is needed.

## 7.4.2 Amplitude Ratios for KY UMa

During another commissioning run in April 2013, we have obtained 17h of MAIA observations of KY UMa, also known as PG 1219+534. KY UMa was discovered to be a pulsator by Koen et al. (1999) and was the subject of several further in-depth studies. Charpinet et al. (2005) presented an asteroseismic model for this star, and

7.4 First Results 113

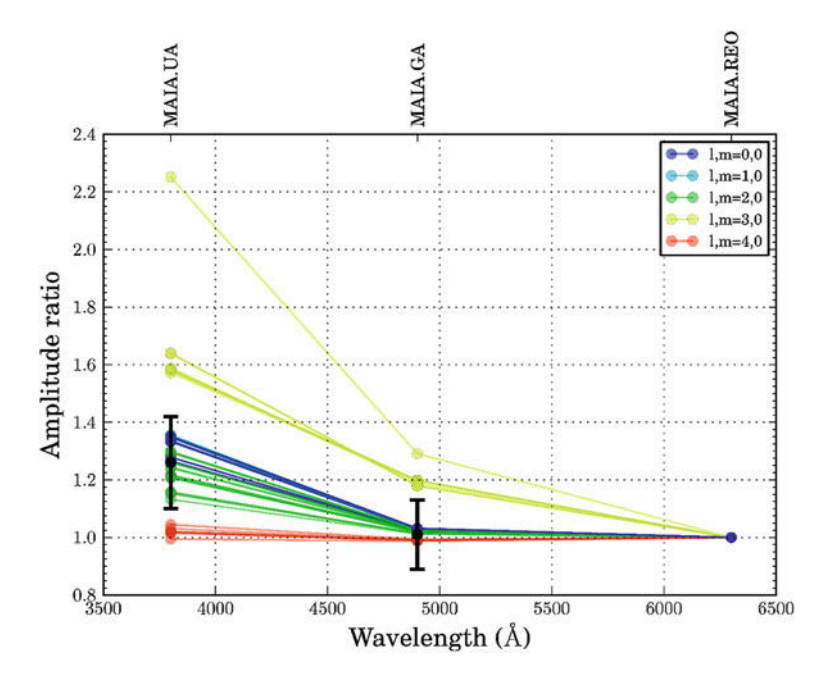


**Fig. 7.12** Same as Fig. 7.11 but for  $f_2 = 7,807.35(6) \mu Hz$ 

Harms et al. (2006) and Reed et al. (2009) performed time resolved spectroscopic and photometric observations. The star was shown to have well-spaced pulsation frequencies, which can more easily be resolved than the frequencies seen in Balloon.

Our observations were performed on the nights of 23, 24, 26, 27 and 30 April, and 01 May, using integration times from 20 to 40 s. Although we were in full commissioning phase, and also suffered from clouds during part of the observations, the dataset is much richer than the one presented in the previous section. Due to its longer duration, it also allows us to separate the main pulsation modes of the star, and to determine the amplitudes of the pulsations in the three wavelength bands. The light curve of the night of 24 April 2013 is shown in Fig. 7.10.

We performed a preliminary data analysis using the data reduction routines described above, and performed a standard interative prewhitening procedure to determine the pulsation frequencies and their amplitudes in the different filters. We find that the 4 frequencies presented in Koen et al. (1999) are also the dominant modes in our observations, across all three channels. Our derived frequencies and their associated pulsation amplitudes in the three passbands are listed in Table 7.4. The amplitude ratios are also given, with r as the reference channel.

In the best-fitting asteroseismic model of Charpinet et al. (2005), the pulsation frequencies  $f_1$  and  $f_2$  were associated with modes of spherical degree l=1. In Figs. 7.11 and 7.12, our amplitude ratios are shown together with model predictions for modes within 5 d<sup>-1</sup> in models (see Chap. 6) of approximately the same effective

temperature and surface gravity as KY UMa. The amplitude ratios for both modes are consistent with l=1 modes, but other solutions cannot be ruled out.

A complete and thorough analysis of the data is currently ongoing.

## 7.5 Summary

After detailed optical and mechanical design work at the University of Leuven, the 3-channel imager MAIA has successfully been installed at the Mercator telescope at La Palma, Canary Islands. A dedicated data reduction pipeline was written in Python. We have also performed an initial zeropoint calibration for the three cameras. The efficiency of the r and g channels is as expected, while that in the g channels is lower than expected. This is most likely due to the coating on the CCD, which is not optimised for blue and near-UV light. A test light curve of Balloon was obtained. The amplitude of the observed pulsation signal is highest in g and lowest in g, as expected, but the time span of the dataset is too short to resolve closely spaced pulsation modes and hence to determine their pulsation amplitudes. A second test light curve was obtained of the sdB pulsator KY UMa. A preliminary analysis shows that amplitude ratios can successfully be derived.

The results presented here show that MAIA was successfully developed and commissioned, and indicate that it will be able to do what it was primarily designed for: shed light on the spherical degrees of pulsation modes in sdB stars. The camera is now regularly used to acquire high speed multi-colour photometry for a variety of science goals, one early example of which can be seen in the study of close sdB binaries by Geier et al. (2014).

### References

Aerts, C. (1996). A&A, 314, 115.

Aerts, C., Jeffery, C. S., Fontaine, G., Dhillon, V. S., Marsh, T. R., & Groot, P. (2006). MNRAS, 367, 1317.

Baran, A., Pigulski, A., Kozieł, D., Ogłoza, W., Silvotti, R., & Zoła, S. (2005). MNRAS, 360, 737. Baran, A., Pigulski, A., & O'Toole, S. J. (2008). MNRAS, 385, 255.

Bertin, E., & Arnouts, S. (1996). A&As, 117, 393.

Charpinet, S., Fontaine, G., Brassard, P., Green, E. M., & Chayer, P. (2005). A&A, 437, 575.

de Boer, K. S., & Maintz, G. (2010). A&A, 520, A46.

Dhillon, V. S., Marsh, T. R., Stevenson, M. J., Atkinson, D. C., Kerry, P., Peacocke, P. T., et al. (2007). MNRAS, 378, 825.

Geier, S., Østensen, R. H., Heber, U., Kupfer, T., Maxted, P. F. L., Barlow, B. N., et al. (2014). A&A, 562, A95

Harms, S. L., Reed, M. D., & O'Toole, S. J. (2006). Baltic Astronomy, 15, 251.

Jeffery, C. S., Aerts, C., Dhillon, V. S., Marsh, T. R., & Gänsicke, B. T. (2005). MNRAS, 362, 66.

Koen, C., O'Donoghue, D., Pollacco, D. L., & Charpinet, S. (1999). MNRAS, 305, 28.

Massey, P., Strobel, K., Barnes, J. V., & Anderson, E. (1988). ApJ, 328, 315.

Oke, J. B. (1974). ApJs, 27, 21.

Oke, J. B. (1990). AJ, 99, 1621.

References 115

Oreiro, R., Ulla, A., Pérez Hernández, F., Østensen, R., Rodríguez López, C., & MacDonald, J. (2004). A&A, 418, 243.

- Pickering, K. A. (2002). DIO The International Journal of Scientific History, 12, 2.
- Raskin, G., Bloemen, S., Morren, J., Perez Padilla, J., Prins, S., Pessemier, W., et al. (2013). A&A, 559, A26.
- Raskin, G., Van Winckel, H., Hensberge, H., et al. (2011). A&A, 526, A69.
- Reed, M. D., Green, E. M., Callerame, K., Seitenzahl, I. R., White, B. A., Hyde, E. A., et al. (2004). *ApJ*, 607, 445.
- Reed, M. D., Eggen, J. R., Harms, S. L., Telting, J. H., Østensen, R. H., O'Toole, S. J., et al. (2009). *A&A*, 493, 175.
- Reif, K., Bagschik, K., de Boer, K. S., Schmoll, J., Mueller, P., Poschmann, H., et al. (1999). In: M. M. Blouke & G. M. Williams (Eds.), Society of Photo-Optical Instrumentation Engineers (SPIE) Conference Series, Vol. 3649 of Society of Photo-Optical Instrumentation Engineers (SPIE) Conference Series, BUSCA: A Telescope Instrumentation for Simultaneous Imaging in Four Optical Bands (pp. 109–120).
- Silvotti, R., Voss, B., Bruni, I., Koester, D., Reimers, D., Napiwotzki, R., et al. (2005). A&A, 443, 195.
- Silvotti, R., Randall, S. K., Dhillon, V. S., Marsh, T. R., Savoury, C. D., Schuh, S., et al. (2010). *Astronomische Nachrichten*, 331, 1034.
- Stone, R. P. S. (1977). ApJ, 218, 767.
- Telting, J. H., Geier, S., Østensen, R. H., Heber, U., Glowienka, L., Nielsen, T., et al. (2008). A&A, 492, 815.
- Vandersteen, J. (2012). PhD Thesis, University of Leuven.
- Vučković, M., Østensen, R. H., Aerts, C., Telting, J. H., Heber, U., & Oreiro, R. (2009). A&A, 505, 239.

# **Chapter 8 Conclusions and Future Prospects**

### 8.1 Conclusions

In this thesis, we presented several detailed studies of compact variables, as well as new theoretical and instrumental tools to aid such studies.

In Chap. 2 we have presented an analysis of fast spectroscopic observations of DQ Her, the prototype of the intermediate polars (IPs), obtained with the ISIS spectrograph at the William Herschel Telescope. We have discovered that DQ Her shows a spiral structure in its accretion disc at the time of our observations. The spiral arms can clearly be seen on Doppler tomography maps of three spectral lines. They arise from tidal effects from the secondary component of the binary on the accretion disc of the primary. Spiral shocks are believed to be an alternative mechanism for the transport of angular momentum in accretion discs besides viscosity. As such, they form a crucial clue in the understanding of accretion disc physics, which is relevant to many parts of astrophysics, including planet and star formation. There is still a debate on whether the spin period of the white dwarf in DQ Her is 71s or twice this value. Our data do not provide conclusive evidence for either of the proposed spin periods. We confirm with greater significance the observation by Martell et al. (1995) that variability can be seen at the spin period in the redshifted part of the HeII λ4686 line, but not in the blueshifted part of the line. This lack of symmetry is unexpected. Since the source of this emission is likely to be the region where matter gets accreted from the disc onto at least one of the magnetic poles of the white dwarf, we would expect to find enhanced blueshifted emission at parts of the spin phase or orbital phase.

To check whether the line variations we observed at the spin period of the white dwarf in DQ Her are the rule in IPs, or rather an exception, a second IP with a fastly spinning white dwarf was targeted. In Chap. 3, we presented fast optical spectroscopy of V455 And, taken with the same instrument as was used for DQ Her, but with a new detector. The spectrograph is now equipped with an Electron Multiplier CCD (EMCCD), which is especially developed to observe faint objects at high cadence. It features a frame transfer buffer, which allows one to observe almost continuously,

with negligible dead-time between two exposures. It also has an electron multiplication stage in the readout register. This makes it possible to detect a single or a few photons in a pixel, which would be hidden in the read-out noise if a standard detector would have been used. We developed a new data reduction strategy that makes full use of a nearby brighter comparison star. No significant structure could be seen in the disc of V455 And. The line variations with the spin period of the white dwarf are, however, unlike any variation patterns observed in IPs before. We could not come up with a qualitative explanation for the observed emission and absorption phenomena, but suspect that we observe accretion via accretion curtains in action. Our observations provide valuable input to detailed modelling efforts of the accretion flow from the disc to the white dwarf and the light emission from the accreting spot on the surface of the white dwarf. Unfortunately, EMCCDs have not often been used yet for spectroscopy in astronomy, and the QUCAM CCDs are hardly ever being requested by ISIS observers. Our study is therefore not only relevant from a scientific point of view, but also as a showcase for the possibilities that EMCCDs offer to observe short-period repetitive effects in faint targets. Even though V455 And is about 2 magnitudes fainter than DQ Her, the use of the QUCAM2 detector allowed us to obtain significantly better data with the same instrument and telescope in a comparable time span.

In Chaps. 4 and 5 we have analysed *Kepler* observations of two close eclipsing binaries, KPD1946+4340 and KOI-74. These targets were the first ones to be found that show highly significant effects of Doppler beaming in their light curves. Accurate system parameters have been determined from light curve modelling, combined with temperature information from spectroscopy. The light curve models account for eclipses, ellipsoidal modulation, light travel time (Rømer) delay, gravitational lensing and Doppler beaming. Using Markov Chain Monte Carlo simulations, we have determined reliable uncertainty estimates for the derived parameters, taking into account degeneracies that commonly occur in light curve fitting. Precise system parameters are a key aspect to the study of stellar evolution. Reliable mass estimates of subdwarf B stars are especially scarce. Our estimate of the mass of the subdwarf in KPD1946+4340 has already been included in the study by Fontaine et al. (2012), where the observed mass distribution of subdwarf B stars has been compared to the distribution predicted for various formation scenarios. The authors made a clear distinction between the measurements based on binary motion and the results from asteroseismology, but found both to be in agreement. This is slightly surprising as stars with different masses spend a different amount of time in the instability strips, which must introduce an important bias in the seismic sample. More subdwarf mass estimates from binary stars will certainly benefit the study, which now still suffers from low number statistics.

In our work on KPD1946+4340 we presented the first comparison of a photometrical radial velocity amplitude, determined from the Doppler beaming amplitude, and a more standard spectroscopic radial velocity amplitude measurement. We found both to be in perfect agreement, for both targets we have studied. In the last two years, Doppler beaming has been detected in light curves of many binaries and even

8.1 Conclusions 119

planetary systems, and has on several occasions been used to derive radial velocity information (e.g. Shporer et al. 2010; Barclay et al. 2012; Silvotti et al. 2012).

In the case of KOI-74, we presented the first detection of Rømer delay in a close binary. With the velocity of the primary known from Doppler beaming, the Rømer delay measurement allowed us to derive the velocity, and thus mass, of the secondary. Since the secondary in KOI-74 is a white dwarf that is outshined by the primary, a main sequence A star, a velocity measurement of the white dwarf would not have been possible with spectroscopy. The complete photometric orbital solution is therefore an important achievement. Rømer delay has now been detected from eclipse timings in another close binary (Barlow et al. 2012), and Rømer delay measured from phase shifts in pulsation modes in stars in a binary has recently also led to photometric mass estimates (Shibahashi and Kurtz 2012; Telting et al. 2012). A systematic search for Rømer delays in the signals of *Kepler* pulsators could lead to the detection of hundreds of new binary stars.

Worryingly, the mass ratio of KOI-74 that could be derived from the amplitude of the ellipsoidal modulation is not in agreement with the mass ratio indicated by the Doppler beaming, Rømer delay and the spectral type of the primary. The same problem was noted in a study of a similar system, KIC 10657664 (Carter et al. 2011). The fact that the primary star in the binary is not in corotation with the orbit, but is on the contrary spinning more rapidly, might be the cause of the discrepancy. We tested a model with rapid rotation but did not find the currently available descriptions to match the observations.

In Chap.4 we have also provided a more accurate expression to compute the gravity darkening coefficient, and we have used it to provide grids of precomputed gravity darkening and limb darkening coefficients for main sequence stars to the community (Claret and Bloemen 2011).

In Chap. 6 we have presented a grid of evolutionary sdB models, which are computed while taking into account important atomic diffusion processes such as radiative levitation and gravitational settling for various chemical elements. We have shown that the build up of iron and nickel in the driving region for pulsations in sdB stars is larger than was previously assumed. The resulting instability strips we computed cover all observed p- and q-mode sdB pulsators and are even a bit more extended. Getting the instability strip predictions right is not only interesting to tune our knowledge of the governing processes such as diffusion and mixing, but is also important in the study of the evolutionary scenarios of sdBs. It is crucial to understand how long sdBs with different masses, envelope masses, etc., spend in the instability strip if one wants to compare the predicted mass and envelope mass distributions for the proposed evolutionary channels with the parameters derived using asteroseismology for a set of pulsating stars. Indeed, if a star is expected to spend less time pulsating, it will be harder to characterize using asteroseismology and hence statistical samples will have to be corrected for this bias. We have also shown predictions of amplitude ratios for pulsations in different passbands throughout the horizontal branch evolution for a representative p- and g-mode sdB pulsator. Comparing our results to the study of Randall et al. (2005), we found a good agreement for the p-mode pulsator. For the g-mode pulsator, we found our results to be in good

agreement for zero age horizontal branch models but not for evolved models, which is consistent with the fact that Randall et al. (2005) considered models without a CO core. Since g-modes are sensitive to the properties of the core, differences in the amplitude ratios of up to 25 per cent arise during the evolution.

In Chap. 7 we have presented the commissioning of the MAIA (Mercator Advanced Imager for Asteroseismology) instrument. MAIA is designed to do fast imaging of a relatively large field in three colour bands simultaneously. The camera is ideally suited for photometric mode identification of pulsation modes in subdwarf B stars. MAIA has successfully been installed at the Mercator telescope and is now being used for scientific observations.

## 8.2 Prospects

Our work on the two intermediate polars has resulted in the best spectroscopic view on the accretion process in systems with rapidly spinning white dwarfs. The observed emission line variations remain, however, largely unexplained. Accurate modelling of (the emission of) the accretion flow from the disc to the poles of the white dwarf has now to be performed to confirm that we are indeed observing emission from accretion curtains. Our use of the EMCCD to perform the V455 And observations has shown that the potential of such detectors is huge. With the existing instrumentation, other science cases involving repetitive signals, such as spectroscopic mode identification of pulsations in compact pulsators, should be attempted.

Our work on the *Kepler* binaries has shown that Doppler beaming can be used to measure radial velocities. Recently, a search for *Kepler* light curves that can be explained by the combination of ellipsoidal modulation, Doppler beaming and reflection signals led to the detection of 7 previously unknown binaries (Faigler et al. 2012). The same group is now conducting a promising search for binaries with low mass stellar companions in the *Kepler* database, which might help to improve the currently poorly calibrated low end of the stellar mass–radius relationship.

Doppler beaming can also be caused by the velocity of the surface of a spinning star. Averaging over the visible surface, the effects cancel out, except during eclipse where the photometric equivalent of the spectroscopic Rossiter-McLaughlin effect could be detected (Groot 2012). A measurement of this effect is very challenging but is expected to be possible with datasets of selected binaries spanning the full *Kepler* mission life-time. It can potentially shed light on the spin-orbit alignment of stars in binaries, which has so far only been achieved for a handful of stellar systems (Shporer et al. 2012).

Our observation that the ellipsoidal modulation amplitude in KOI-74 is not in agreement with the masses derived from Doppler beaming, Rømer delay and the spectral type of the primary, should elicit more research about the influence of rapid rotation on the deformation of a star that is also experiencing tidal forces from a companion. The ellipsoidal modulation amplitude has regularly been used to derive the mass ratio of binaries for which corotation of the deformed star(s) was assumed

8.2 Prospects 121

but not checked. All these mass ratios can be off if the discrepancy we noted is effectively due to the rapid rotation of the primary. The masses of massive planets that were derived from the same effect can be equally affected. As such, this is an extremely important problem to be solved.

Related to subdwarf B star asteroseismology, we found that amplitude ratios for *g*-modes significantly change with the age of the star since the zero-age extreme horizontal branch. In preparation for the analysis of upcoming multicolour data from sdB pulsators that will be obtained with the new MAIA camera, a more dense grid of models will be computed using the tools we have set up. This grid can then be used to perform forward stellar modelling, i.e. to find the models that match the observations best, both in terms of observed pulsation frequencies and their amplitude ratios in different filters.

Concerning the MAIA camera, the end of the commissioning and calibration effort mark the beginning of a new epoch for the Mercator telescope, whose operations are now funded until 2017. With MAIA as a second permanently mounted instrument besides the successful HERMES spectrograph, Mercator is equipped with a state-of-the-art multi-colour imager. Although designed with sdB asteroseismology in mind, many other projects, such as studies of flickering in CVs, fast imaging of compact binaries to study eclipse timing variations, oscillation detection in stellar flaring, etc. can be embarked upon.

### References

Barclay, T., Huber, D., Rowe, J. F., et al. (2012). ApJ, 761, 53.

Barlow, B. N., Wade, R. A., & Liss, S. E. (2012). ApJ, 753, 101.

Carter, J. A., Rappaport, S., & Fabrycky, D. (2011). ApJ, 728, 139.

Claret, A., & Bloemen, S. (2011). A&A, 529, A75.

Faigler, S., Mazeh, T., Quinn, S. N., Latham, D. W., & Tal-Or, L. (2012). ApJ, 746, 185.

Fontaine, G., Brassard, P., Charpinet, S., Green, E. M., Randall, S. K., & Van Grootel, V. (2012). *A&A*, 539, A12.

Groot, P. J. (2012). ApJ, 745, 55.

Martell, P. J., Horne, K., Price, C. M., & Gomer, R. H. (1995). ApJ, 448, 380.

Randall, S. K., Fontaine, G., Brassard, P., & Bergeron, P. (2005). ApJS, 161, 456.

Shibahashi, H., & Kurtz, D. W. (2012). MNRAS, 422, 738.

Shporer, A., Kaplan, D. L., Steinfadt, J. D. R., Bildsten, L., Howell, S. B., & Mazeh, T. (2010). *ApJ*, 725, L200.

Shporer, A., Brown, T., Mazeh, T., & Zucker, S. (2012). New A, 17, 309.

Silvotti, R., Østensen, R. H., Bloemen, S., et al. (2012). MNRAS, 424, 1752.

Telting, J. H., Østensen, R. H., Baran, A. S., et al. (2012). A&A, 544, A1.

## **Curriculum Vitae**

Steven Bloemen was born on the 6th of March 1986 in Geel (Belgium). He obtained a Bachelor in Physics (June 2007) and a Master of Science degree in Astronomy and Astrophysics (June 2009) from the University of Leuven (Belgium). He spent the second year of the Master programme as an Erasmus student at the University of Warwick (UK), where he made a master thesis under supervision of Prof. Tom Marsh and Dr. Danny Steeghs. Afterwards, he started a PhD at the University of Leuven under supervision of Prof. Conny Aerts and Dr. Roy Østensen.

In September 2013, Steven took up the job of the instrument scientist of the BlackGEM Array at the Radboud University of Nijmegen (The Netherlands). The BlackGEM Array is currently being developed and is designed to search for optical counterparts of gravitational wave radiation sources. It will consist of fifteen 60-cm telescopes and will be located at the ESO observatory at La Silla (Chile).

The list below gives an overview of the author's publications until March 2013. Articles in refereed journals and in conference proceedings are listed separately.

#### **Articles in Refereed International Journals**

Journal abbreviations and impact factors (ISI JCR 2011):

A&A: Astronomy and Astrophysics (4.6)

AJ: Astronomical Journal (4.0)

*ApJ*: Astrophysical Journal (6.0)

MNRAS: Monthly Notices of the Royal Astronomical Society (4.9)

Nature: Nature (36.3)

- (1) S. Bloemen, D. Steeghs, K. De Smedt, J. Vos, B. T. Gänsicke, T. R. Marsh, and P. Rodriguez-Gil. Remarkable spectral variability on the spin period of the accreting white dwarf in V455 And. *MNRAS*, 429:3433–3438, March 2013.
- (2) P. Lampens, A. Tkachenko, H. Lehmann, J. Debosscher, C. Aerts, P. G. Beck, **S. Bloemen**, N. Kochiashvili, A. Derekas, J. C. Smith, P. Tenenbaum, and J. D. Twicken. Low-frequency variations of unknown origin in the Kepler  $\delta$  Scuti star KIC 5988140 = HD 188774. A&A, 549:A104, January 2013.
- (3) T. Barclay, D. Huber, J. F. Rowe, J. J. Fortney, C. V. Morley, E. V. Quintana, D. C. Fabrycky, G. Barentsen, **S. Bloemen**, J. L. Christiansen, B.-O. Demory, B. J. Fulton, J. M. Jenkins, F. Mullally, D. Ragozzine, S. E. Seader, A. Shporer, P. Tenenbaum, and S. E. Thompson. Photometrically Derived Masses and Radii of the Planet and Star in the TrES-2 System. *APJ*, 761:53, December 2012.
- (4) P. Lampens, A. Tkachenko, H. Lehmann, J. Debosscher, C. Aerts, P. G. Beck, S. Bloemen, N. Kochiashvili, and A. Derekas. Do we see the simultaneous occurrence of stellar rotational effects and short-period pulsations in some Atype Kepler stars? *Astronomische Nachrichten*, 333:975–977, December 2012.
- (5) B. Mosser, M. J. Goupil, K. Belkacem, J. P. Marques, P. G. Beck, S. Bloemen, J. De Ridder, C. Barban, S. Deheuvels, Y. Elsworth, S. Hekker, T. Kallinger, R. M. Ouazzani, M. Pinsonneault, R. Samadi, D. Stello, R. A. García, T. C. Klaus, J. Li, S. Mathur, and R. L. Morris. Spin down of the core rotation in red giants. A&A, 548:A10, December 2012.

(6) J. Vos, R. H. Østensen, P. Degroote, K. De Smedt, E. M. Green, U. Heber, H. Van Winckel, B. Acke, S. Bloemen, P. De Cat, K. Exter, P. Lampens, R. Lombaert, T. Masseron, J. Menu, P. Neyskens, G. Raskin, E. Ringat, T. Rauch, K. Smolders, and A. Tkachenko. The orbits of subdwarf B+main-sequence binaries. I. The sdB+G0 system PG 1104+243. A&A, 548:A6, December 2012.

- (7) A. S. Baran, M. D. Reed, D. Stello, R. H. Østensen, J. H. Telting, E. Pakštienë, S. J. O'Toole, R. Silvotti, P. Degroote, S. Bloemen, H. Hu, V. Van Grootel, B. D. Clarke, J. Van Cleve, S. E. Thompson, and S. D. Kawaler. A pulsation zoo in the hot subdwarf B star KIC 10139564 observed by Kepler. MNRAS, 424:2686–2700, August 2012.
- (8) R. Silvotti, R. H. Østensen, S. Bloemen, J. H. Telting, U. Heber, R. Oreiro, M. D. Reed, L. E. Farris, S. J. O'Toole, L. Lanteri, P. Degroote, H. Hu, A. S. Baran, J. J. Hermes, L. G. Althaus, T. R. Marsh, S. Charpinet, J. Li, R. L. Morris, and D. T. Sanderfer. Orbital properties of an unusually low-mass sdB star in a close binary system with a white dwarf. MNRAS, 424:1752–1761, August 2012.
- (9) J. H. Telting, R. H. Østensen, A. S. Baran, S. Bloemen, M. D. Reed, R. Oreiro, L. Farris, T. A. Ottosen, C. Aerts, S. D. Kawaler, U. Heber, S. Prins, E. M. Green, B. Kalomeni, S. J. O'Toole, F. Mullally, D. T. Sanderfer, J. C. Smith, and H. Kjeldsen. Three ways to solve the orbit of KIC 11 558 725: a 10-day beaming sdB+WD binary with a pulsating subdwarf. A&A, 544:A1, August 2012.
- (10) A. Tkachenko, C. Aerts, K. Pavlovski, J. Southworth, P. Degroote, J. Debosscher, M. Still, S. Bryson, G. Molenberghs, S. Bloemen, B. L. de Vries, M. Hrudkova, R. Lombaert, P. Neyskens, P. I. Pápics, G. Raskin, H. Van Winckel, R. L. Morris, D. T. Sanderfer, and S. E. Seader. Detection of gravity modes in the massive binary V380 Cyg from Kepler space-based photometry and high-resolution spectroscopy. MNRAS, 424:L21–L25, July 2012.
- (11) S. Bloemen, T. R. Marsh, P. Degroote, R. H. Østensen, P. I. Pápics, C. Aerts, D. Koester, B. T. Gänsicke, E. Breedt, R. Lombaert, S. Pyrzas, C. M. Copperwheat, K. Exter, G. Raskin, H. Van Winckel, S. Prins, W. Pessemier, Y. Frémat, H. Hensberge, A. Jorissen, and S. Van Eck. Mass ratio from Doppler beaming and Rømer delay versus ellipsoidal modulation in the Kepler data of KOI-74. MNRAS, 422:2600–2608, May 2012.
- (12) H. Pablo, S. D. Kawaler, M. D. Reed, S. Bloemen, S. Charpinet, H. Hu, J. Telting, R. H. Østensen, A. S. Baran, E. M. Green, J. J. Hermes, T. Barclay, S. J. O'Toole, F. Mullally, D. W. Kurtz, J. Christensen-Dalsgaard, D. A. Caldwell, J. L. Christiansen, and K. Kinemuchi. Seismic evidence for non-synchronization in two close sdb+dM binaries from Kepler photometry. MNRAS, 422:1343–1351, May 2012.
- (13) G. Matijevič, A. Prša, J. A. Orosz, W. F. Welsh, **S. Bloemen**, and T. Barclay. Kepler Eclipsing Binary Stars. III. Classification of Kepler Eclipsing Binary Light Curves with Locally Linear Embedding. *Aj*, 143:123, May 2012.
- (14) K. Smolders, P. Neyskens, J. A. D. L. Blommaert, S. Hony, H. van Winckel, L. Decin, S. van Eck, G. C. Sloan, J. Cami, S. Uttenthaler, P. Degroote, D. Barry, M. Feast, M. A. T. Groenewegen, M. Matsuura, J. Menzies, R. Sahai, J. T. van

Loon, A. A. Zijlstra, B. Acke, **S. Bloemen**, N. Cox, P. De Cat, M. Desmet, K. Exter, D. Ladjal, R. Østensen, S. Saesen, F. van Wyk, T. Verhoelst, and W. Zima. The Spitzer spectroscopic survey of S-type stars. *A&A*, 540:A72, April 2012.

- (15) W. F. Welsh, J. A. Orosz, J. A. Carter, D. C. Fabrycky, E. B. Ford, J. J. Lissauer, A. Prša, S. N. Quinn, D. Ragozzine, D. R. Short, G. Torres, J. N. Winn, L. R. Doyle, T. Barclay, N. Batalha, S. Bloemen, E. Brugamyer, L. A. Buchhave, C. Caldwell, D. A. Caldwell, J. L. Christiansen, D. R. Ciardi, W. D. Cochran, M. Endl, J. J. Fortney, T. N. Gautier, III, R. L. Gilliland, M. R. Haas, J. R. Hall, M. J. Holman, A. W. Howard, S. B. Howell, H. Isaacson, J. M. Jenkins, T. C. Klaus, D. W. Latham, J. Li, G. W. Marcy, T. Mazeh, E. V. Quintana, P. Robertson, A. Shporer, J. H. Steffen, G. Windmiller, D. G. Koch, and W. J. Borucki. Transiting circumbinary planets Kepler-34 b and Kepler-35 b. *Nature*, 481:475–479, January 2012.
- (16) P. Degroote, B. Acke, R. Samadi, C. Aerts, D. W. Kurtz, A. Noels, A. Miglio, J. Montalbán, S. Bloemen, A. Baglin, F. Baudin, C. Catala, E. Michel, and M. Auvergne. CoRoT's view on variable B8/9 stars: spots versus pulsations. Evidence for differential rotation in HD 174648. A&A, 536:A82, December 2011.
- (17) J. J. Hermes, F. Mullally, R. H. Østensen, K. A. Williams, J. Telting, J. Southworth, **S. Bloemen**, S. B. Howell, M. Everett, and D. E. Winget. Discovery of a ZZ Ceti in the Kepler Mission Field. *APJ*, 741:L16, November 2011.
- (18) R. H. Østensen, S. Bloemen, M. Vučković, C. Aerts, R. Oreiro, K. Kinemuchi, M. Still, and D. Koester. At Last–A V777 Her Pulsator in the Kepler Field. APJ, 736:L39, August 2011.
- (19) R. H. Østensen, R. Silvotti, S. Charpinet, R. Oreiro, S. Bloemen, A. S. Baran, M. D. Reed, S. D. Kawaler, J. H. Telting, E. M. Green, S. J. O'Toole, C. Aerts, B. T. Gänsicke, T. R. Marsh, E. Breedt, U. Heber, D. Koester, A. C. Quint, D. W. Kurtz, C. Rodríguez-López, M. Vučković, T. A. Ottosen, S. Frimann, A. Somero, P. A. Wilson, A. O. Thygesen, J. E. Lindberg, H. Kjeldsen, J. Christensen-Dalsgaard, C. Allen, S. McCauliff, and C. K. Middour. First Kepler results on compact pulsators-VI. Targets in the final half of the survey phase. MNRAS, 414:2860–2870, July 2011.
- (20) A. Claret and **S. Bloemen**. Gravity and limb-darkening coefficients for the Kepler, CoRoT, Spitzer, uvby, UBVRIJHK, and Sloan photometric systems. *A&A*, 529:A75, May 2011.
- (21) S. Bloemen, T. R. Marsh, R. H. Østensen, S. Charpinet, G. Fontaine, P. Degroote, U. Heber, S. D. Kawaler, C. Aerts, E. M. Green, J. Telting, P. Brassard, B. T. Gänsicke, G. Handler, D. W. Kurtz, R. Silvotti, V. Van Grootel, J. E. Lindberg, T. Pursimo, P. A. Wilson, R. L. Gilliland, H. Kjeldsen, J. Christensen-Dalsgaard, W. J. Borucki, D. Koch, J. M. Jenkins, and T. C. Klaus. Kepler observations of the beaming binary KPD 1946+4340. MNRAS, 410: 1787–1796, January 2011.

(22) G. Fontaine, P. Brassard, E. M. Green, S. Charpinet, P. Dufour, I. Hubeny, D. Steeghs, C. Aerts, S. K. Randall, P. Bergeron, B. Guvenen, C. J. O'Malley, V. Van Grootel, R. H. Østensen, S. Bloemen, R. Silvotti, S. B. Howell, A. Baran, S. O. Kepler, T. R. Marsh, M. H. Montgomery, R. Oreiro, J. Provencal, J. Telting, D. E. Winget, W. Zima, J. Christensen-Dalsgaard, and H. Kjeldsen. Discovery of a New AM CVn System with the Kepler Satellite. APJ, 726:92, January 2011.

- (23) S. D. Kawaler, M. D. Reed, R. H. Østensen, S. Bloemen, D. W. Kurtz, A. C. Quint, R. Silvotti, A. S. Baran, E. M. Green, S. Charpinet, J. Telting, C. Aerts, G. Handler, H. Kjeldsen, J. Christensen-Dalsgaard, W. J. Borucki, and D. G. Koch. First Kepler results on compact pulsators-V. Slowly pulsating subdwarf B stars in short-period binaries. MNRAS, 409:1509–1517, December 2010.
- (24) M. D. Reed, S. D. Kawaler, R. H. Østensen, S. Bloemen, A. Baran, J. H. Telting, R. Silvotti, S. Charpinet, A. C. Quint, G. Handler, R. L. Gilliland, W. J. Borucki, D. G. Koch, H. Kjeldsen, and J. Christensen-Dalsgaard. First Kepler results on compact pulsators-III. Subdwarf B stars with V1093 Her and hybrid (DW Lyn) type pulsations. MNRAS, 409:1496–1508, December 2010.
- (25) S. D. Kawaler, M. D. Reed, A. C. Quint, R. H. Østensen, R. Silvotti, A. S. Baran, S. Charpinet, S. Bloemen, D. W. Kurtz, J. Telting, G. Handler, H. Kjeldsen, J. Christensen-Dalsgaard, W. J. Borucki, and D. G. Koch. First Kepler results on compact pulsators-II. KIC 010139564, a new pulsating subdwarf B (V361 Hya) star with an additional low-frequency mode. MNRAS, 409:1487–1495, December 2010.
- (26) R. H. Østensen, R. Silvotti, S. Charpinet, R. Oreiro, G. Handler, E. M. Green, S. Bloemen, U. Heber, B. T. Gänsicke, T. R. Marsh, D. W. Kurtz, J. H. Telting, M. D. Reed, S. D. Kawaler, C. Aerts, C. Rodríguez-López, M. Vučković, T. A. Ottosen, T. Liimets, A. C. Quint, V. Van Grootel, S. K. Randall, R. L. Gilliland, H. Kjeldsen, J. Christensen-Dalsgaard, W. J. Borucki, D. Koch, and E. V. Quintana. First Kepler results on compact pulsators-I. Survey target selection and the first pulsators. MNRAS, 409:1470–1486, December 2010.
- (27) R. H. Østensen, E. M. Green, S. Bloemen, T. R. Marsh, J. B. Laird, M. Morris, E. Moriyama, R. Oreiro, M. D. Reed, S. D. Kawaler, C. Aerts, M. Vučković, P. Degroote, J. H. Telting, H. Kjeldsen, R. L. Gilliland, J. Christensen-Dalsgaard, W. J. Borucki, and D. Koch. 2M1938+4603: a rich, multimode pulsating sdB star with an eclipsing dM companion observed with Kepler. MNRAS, 408:L51–L55, October 2010.
- (28) **S. Bloemen**, T. R. Marsh, D. Steeghs, and R. H. Østensen. Spin-resolved spectroscopy of the intermediate polar DQ Her. *MNRAS*, 407:1903–1912, September 2010.
- (29) P. Degroote, C. Aerts, A. Baglin, A. Miglio, M. Briquet, A. Noels, E. Niemczura, J. Montalban, **S. Bloemen**, R. Oreiro, M. Vučković, K. Smolders, M. Auvergne, F. Baudin, C. Catala, and E. Michel. Deviations from a uniform period spacing of gravity modes in a massive star. *Nature*, 464:259–261, March 2010.

### **Articles in Conference Proceedings**

(1) A. Prša, E. F. Guinan, E. J. Devinney, P. Degroote, **S. Bloemen**, and G. Matijevič. Advances in Modeling Eclipsing Binary Stars in the Era of Large All-Sky Surveys with EBAI and PHOEBE. In M. T. Richards and I. Hubeny, editors, *IAU Symposium*, volume 282 of *IAU Symposium*, pages 271–278, April 2012.

- (2) K. Hambleton, D. Kurtz, A. Prša, S. Bloemen, and J. Southworth. KIC 4544587: An Eccentric, Short Period Binary with δ Scuti Pulsations and Tidally Excited Modes. In M. T. Richards and I. Hubeny, editors, *IAU Symposium*, volume 282 of *IAU Symposium*, pages 77–78, April 2012.
- (3) V. Bakış, H. Hensberge, M. Zejda, P. de Cat, F. Yılmaz, **S. Bloemen**, P. Svoboda, and O. Demircan. Northern Binaries in the Evrena Project. In M. T. Richards and I. Hubeny, editors, *IAU Symposium*, volume 282 of *IAU Symposium*, pages 71–72, April 2012.
- (4) M. Vučković, R. H. Østensen, B. Acke, M. D. Reed, R. Oreiro, S. Bloemen, and A. S. Baran. We Like it Bright: GALEX J06398+5156. In D. Kilkenny, C. S. Jeffery, and C. Koen, editors, Fifth Meeting on Hot Subdwarf Stars and Related Objects, volume 452 of Astronomical Society of the Pacific Conference Series, page 257, March 2012.
- (5) P. F. L. Maxted, D. R. Anderson, M. R. Burleigh, A. Collier Cameron, U. Heber, B. T. Gänsicke, S. Geier, T. Kupfer, T. R. Marsh, G. Nelemans, S. J. O'Toole, R. H. Østensen, B. Smalley, R. G. West, and S. Bloemen. Discovery of a Stripped Red-giant Core in a Bright Eclipsing Binary Star. In D. Kilkenny, C. S. Jeffery, and C. Koen, editors, Fifth Meeting on Hot Subdwarf Stars and Related Objects, volume 452 of Astronomical Society of the Pacific Conference Series, page 137, March 2012.
- (6) V. A. Jacobs, R. H. Østensen, H. van Winckel, S. Bloemen, P. I. Pápics, G. Raskin, J. Debosscher, S. Uttenthaler, E. van Aarle, C. Waelkens, E. Bauwens, T. Verhoelst, C. Gielen, H. Lehmann, and R. Oreiro. HERMES High-Resolution Spectroscopy of HD 149382–Where Did the Planet Go? In S. Schuh, H. Drechsel, and U. Heber, editors, American Institute of Physics Conference Series, volume 1331 of American Institute of Physics Conference Series, pages 304–309, March 2011.
- (7) S. Bloemen, D. Steeghs, and T. Marsh. High speed spectroscopy of intermediate polars. In Proceedings of High Time Resolution Astrophysics The Era of Extremely Large Telescopes (HTRA-IV). May 5–7, 2010. Agios Nikolaos, Crete Greece. Published online at http://pos.sissa.it/cgi-bin/reader/conf.cgi?confid=108, id.11, 2010.
- (8) M. Vučković, R. Østensen, **S. Bloemen**, I. Decoster, and C. Aerts. Orbital Effects in VLT–UVES Spectra of AA Dor and NY Vir. In U. Heber, C. S. Jeffery, and R. Napiwotzki, editors, *Hot Subdwarf Stars and Related Objects*, volume 392 of *Astronomical Society of the Pacific Conference Series*, page 199, 2008.

## Index

A	Ellipsoidal modulation, 43, 47–49, 60, 69,	
Accretion curtain, 9, 25, 27, 30, 33, 34, 39,	76, 78, 121	
40, 120	EMCCD, 33, 118	
Accretion disc, 4, 7, 8, 13, 14, 16, 20, 22, 26,		
30, 33–35, 37, 38, 117		
Amplitude ratios, 88, 92, 94, 99, 113, 114,	F	
120, 121	Flatfield, 104	
Angular momentum, 22, 30, 44	Frame-transfer CCD, 6, 97, 118	
Asteroseismology, 5, 7, 10, 82, 98		
Atomic diffusion, 82, 120		
	G	
В	Gravitational lensing, 47, 71	
	Gravitational settling, 83	
Beat period, 13 Binary, 14, 33, 43, 44, 49, 52, 54, 59, 60, 64,	Gravity darkening, 48, 69, 71, 119	
68, 70, 71, 76, 81		
Binary star, 3, 4, 7, 120		
BUSCA, 102	H	
BUSCA, 102	Helium burning, 2, 45	
	HERMES spectrograph, 65, 66	
C	Hydrogen burning, 2	
Cataclysmic variable, 4, 7, 13, 15, 19, 33, 34,	Hydrogen envelope, 4, 44, 81	
59		
Common envelope, 4, 44, 81	I	
Compact binary, 50, 63	Instability strip, 84, 86, 94, 120	
Compact stars, 55, 78	Intermediate polar, 4, 7, 13, 22, 23, 26, 30,	
	33–35, 38–40, 117, 120	
<b>D</b>	ISIS spectrograph, 5, 33, 39, 65, 66	
D	1313 spectrograph, 3, 33, 39, 63, 66	
Doppler beaming, 9, 43, 45, 47, 48, 50, 57,		
60, 63–65, 68, 70, 71, 73, 76, 78,	K	
118–120 December 7, 12, 15, 18	Kepler space telescope, 6, 43, 45, 49, 55, 60,	
Doppler tomography, 7, 13–15, 18	63, 64, 67, 70, 71, 78, 118, 120	
	05, 01, 07, 70, 71, 70, 110, 120	
E		
Eclipsing binary, 7, 9, 14, 44, 47, 55, 63, 64,	L	
78	Limb darkening, 48, 69, 71, 89, 119	
	-	
© Springer International Publishing Switzerland 2015		
S. Bloemen, High-Precision Studies of Compact Variable Stars,		
Springer Theses, DOI 10.1007/978-3-319-10283-2		

132 Index

M	S
Magnetic field, 4, 13, 14, 22, 25, 26, 34	Spectroscopy, 7, 15, 23, 30, 33–35, 37–39,
MAIA, 10, 88, 97, 100, 101, 110, 114, 120,	43, 45, 49, 56, 60, 63–65, 70, 73,
121	76–78, 117
Mass transfer, 4, 9, 13, 20, 22, 120	Spin period, 13, 14, 23, 24, 27–30, 33–35,
Mercator Telescope, 88, 97	38, 40, 77, 117
Mode identification, 88, 98	Standard stars, 106
	Stellar evolution, 2
	Subdwarf B star, 4, 10, 43, 44, 47, 50, 52,
Optical conservation	55, 57, 60, 81, 110, 118, 120
Orbital energy, 44	
Orbital period, 4, 14, 36, 66, 69 Orbital phase, 13	
Orbital phase, 13	U
	ULTRACAM, 101, 110
P	ULIKACAM, 101, 110
Photometry, 24, 34, 37, 45, 49, 64, 67, 77,	
97, 104, 109, 113	
Pulsations, 13, 14, 24, 25, 27–30, 34–36, 43,	$\mathbf{W}$
45, 55, 59, 60, 82, 98, 110, 113	White dwarf, 3, 4, 8, 13, 14, 16, 20, 22, 23,
	25, 26, 30, 33–36, 39, 43, 44, 47,
	49, 52, 59, 60, 63, 64, 70–72, 78,
R	117, 118
Rømer delay, 10, 63, 65, 70, 72, 76, 78, 118, 119	William Herschel telescope, 5, 33
Radiative levitation, 83	
Red giant, 2, 4, 7, 64	
Roche lobe, 3, 20, 72	$\mathbf{Z}$
Roche lobe overflow, 4, 5, 64, 81	Zeropoint (photometric), 106, 109